Université de Montréal

Étude du champ magnétique dans les nuages moléculaires

par

Martin Houde

Département de physique

Faculté des arts et des sciences

Thèse présentée à la Faculté des études supérieures

en vue de l'obtention du grade de

Philosophiæ Doctor (Ph.D.)

en physique

Juin, 2000

Pierre Bastien
Département de Physique
Université de Montréal
Montréal, Québec
H3C 3J7

15 mars 2000

RE: Autorisation de microfilmage et microfichage

À qui de droit,

La présente a pour but de confirmer mon autorisation à tout éventuel microfilmage ou microfichage de la thèse de doctorat de Martin Houde. Cette thèse étant en partie composée d'articles dont je suis coauteur.

Bien à vous,

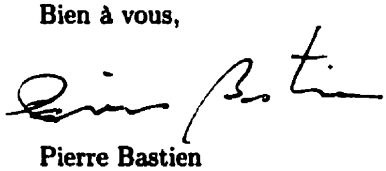

Pierre Bastien

Ruisheng Peng
Caltech Submillimeter Observatory
111 Nowelo Street,
Hilo, HI 96720
USA

15 mars 2000

RE: Autorisation de microfilmage et microfichage

À qui de droit,

La présente a pour but de confirmer mon autorisation à tout éventuel microfilmage ou microfichage de la thèse de doctorat de Martin Houde. Cette thèse étant en partie composée d'articles dont je suis coauteur.

Bien à vous,

Ruisheng Peng

Hiroshige Yoshida
Caltech Submillimeter Observatory
111 Nowelo Street,
Hilo, HI 96720
USA

15 mars 2000

RE: Autorisation de microfilmage et microfichage

À qui de droit,

La présente a pour but de confirmer mon autorisation à tout éventuel microfilmage ou microfichage de la thèse de doctorat de Martin Houde. Cette thèse étant en partie composée d'articles dont je suis coauteur.

Bien à vous,

Hiroshige Yoshida

Thomas G. Phillips
California Institute of Technology
Pasadena, CA 91125
USA

15 mars 2000

RE: Autorisation de microfilmage et microfichage

À qui de droit,

La présente a pour but de confirmer mon autorisation à tout éventuel microfilmage ou microfichage de la thèse de doctorat de Martin Houde. Cette thèse étant en partie composée d'articles dont je suis coauteur.

Bien à vous,

Thomas G. Phillips

John E. Carlstrom
University of Chicago
Chicago, IL 60637
USA

15 mars 2000

RE: Autorisation de microfilmage et microfichage

À qui de droit,

La présente a pour but de confirmer mon autorisation à tout éventuel microfilmage ou microfichage de la thèse de doctorat de Martin Houde. Cette thèse étant en partie composée d'articles dont je suis coauteur.

Bien à vous,

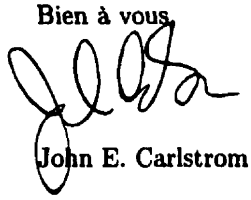

John E. Carlstrom

David A. Schleuning
Exponent-Failure Analysis Associates
San Francisco, CA 94025
USA

15 mars 2000

RE: Autorisation de microfilmage et microfichage

À qui de droit,

La présente a pour but de confirmer mon autorisation à tout éventuel microfilmage ou microfichage de la thèse de doctorat de Martin Houde. Cette thèse étant en partie composée d'articles dont je suis coauteur.

Bien à vous,

David A. Schleuning

Rachel L. Akeson
Infrared Process & Analysis Center
California Institute of Technology
Pasadena, CA 91125
USA

15 mars 2000

RE: Autorisation de microfilmage et microfichage

À qui de droit,

La présente a pour but de confirmer mon autorisation à tout éventuel microfilmage ou microfichage de la thèse de doctorat de Martin Houde. Cette thèse étant en partie composée d'articles dont je suis coauteur.

Bien à vous,

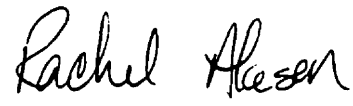

Rachel L. Akeson

Oliver P. Lay
Jet Propulsion Laboratory
California Institute of Technology
Pasadena, CA 91109
USA

15 mars 2000

RE: Autorisation de microfilmage et microfichage

À qui de droit,

La présente a pour but de confirmer mon autorisation à tout éventuel microfilmage ou microfichage de la thèse de doctorat de Martin Houde. Cette thèse étant en partie composée d'articles dont je suis coauteur.

Bien à vous,

Oliver P. Lay

Université de Montréal

Faculté des études supérieures

Cette thèse intitulée:

Étude du champ magnétique dans les nuages moléculaires

présentée par:

Martin Houde

a été évaluée par un jury composé des personnes suivantes:

Dr Anthony F. J. Moffat,	président-rapporteur
Dr Pierre Bastien,	directeur de recherche
Dr Daniel Nadeau,	membre du jury
Dr Alyssa A. Goodman,	examinateur externe

Thèse acceptée le: .....

Sommaire

Ce travail est une étude du champ magnétique dans l'environnement circumstellaire des étoiles jeunes. Il a pour origine la certitude qu'avait l'auteur qu'il se devait d'être possible de détecter la présence d'un champ magnétique, et de possiblement le caractériser, par le biais d'observations de profils spectraux d'espèces moléculaires ioniques.

Il en découle donc qu'un des buts principaux était de prouver que cela est effectivement possible. La thèse comporte alors des éléments théoriques et expérimentaux qui sont à la fois complémentaires et intimement liés. L'aspect théorique est basé sur l'interaction mutuelle que des particules neutres et chargées peuvent avoir l'une sur l'autre dans un plasma faiblement ionisé comme ceux existants dans les nuages moléculaires sites de formation stellaire. Il appert que la présence d'un champ magnétique a un effet direct sur le comportement des ions (via la force de Lorentz) et indirect sur les molécules neutres (via les nombreuses collisions entre les deux types de particules). Une telle interaction est, comme il est maintenant bien connu, présente dans les premières étapes de la formation d'une étoile. Il s'agit bien sûr de la diffusion ambipolaire. Nous montrerons qu'il existe cependant un autre type de diffusion, jusqu'ici inconnue, qui se manifeste plus tard au cours de l'évolution des nuages moléculaires. Celle-ci peut avoir un effet dramatique sur l'apparence des profils spectraux (de rotation moléculaire) des espèces ioniques lorsque comparés à ceux qu'exhibent des espèces neutres coexistantes. Mais pour ce faire, il doit y avoir existence de mouvements organisés (des flots ou jets) de matière ou encore la présence de turbulence dans les régions considérées. Une distribution de vélocité du type maxwellienne ne révèlera pas la présence du champ magnétique.

Les observations, qui ont pour but de confirmer la théorie, se situent dans le domaine des longueurs d'ondes millimétriques et sous-millimétriques. Plusieurs espèces moléculaires furent détectées dans un échantillon significatif de nuages moléculaires. L'effet prédit fut confirmé et ce peu importe si les raies observées sont opaques ou transparentes.

Dans le dernier chapitre, nous considérerons une application intéressante où nous utiliserons la manifestation de cet effet (ou son manque) pour vérifier l'alignement préférentiel des flots bipolaires, qui accompagnent souvent la présence de proto-étoiles, avec le champ magnétique local.

Table des Matières

Liste des Tableaux

Liste des Figures

"Prends ton temps... mais dépêche-toi!"

À la mémoire de mon grand-père Wilfrid Pomerleau, qui m'a appris ce dicton rempli de sagesse, lequel j'ai pu grandement apprécier au cours des cinq dernières années

Remerciements

L'auteur tient à remercier son directeur de recherches, Prof. Pierre Bastien, pour son aide tout au long de ce travail et de même que pour avoir accepté de diriger un étudiant situé à quelques milliers de kilomètres de distance. Il m'a donné la latitude nécéssaire pour me permettre d'explorer différentes avenues, qui se sont souvent montrées infructueuses, et m'a, par le fait même, permis d'apprendre par mes propres erreurs.

Ce travail fut facilité par le support financier des Fonds pour la formation de chercheurs et l'aide à la recherche (FCAR) et du département de physique de l'Université de Montréal.

There are also many other people that have been a constant source of encouragement and help. Prof. Roger Hildebrand and his Hertz group for allowing me to use their instrument (which I originally intended to use for this work) and for many insightful discussions on the nature of the magnetic field. Prof. John Carlstrom for allowing me to join him and his group for an observing session at the Owens Valley Radio Observatory. This led to the work presented in the appendix of this thesis. Many thanks to all of the staff at the Caltech Submillimeter Observatory (CSO), past and present. Especially Dr. Ruisheng Peng for his assistance with the great majority of observing runs (and there were many of them) and who, for a while, patiently endured my daily output of "new ideas" and ramblings before finally arriving to the final product.

I am deeply indebted to my superior, friend and golfing partner Prof. T. G. Phillips of the California Institute of Technology and director of the CSO. He first offered me an interesting and challenging job, then allowed me to pursue my ambitions and constantly

supported my efforts and studies for the obtention of my degree. There probably isn't another being in the whole Galaxy who had more observing time than I on a major telescope in the last couple of years. Hopefully, the work presented here will provide some justification for the confidence that was shown in me during this period.

Finally, to my wife Renée. You are definitively the most wonderful person I have ever met. Thank you for your unconditional support, patience and most importantly, all your love.

Avant-propos

Le corps de cette thèse est composé de quatres articles, tous présentés dans leur langue de publication (i.e. l'anglais). Les trois premiers forment les chapitres 1, 2 et 3 et le dernier, qui tient plutôt de la physique que de l'astrophysique, peut être trouvé en appendice. Puisque le champ magnétique de nature astronomique est le sujet central aux trois premiers articles, les unités Gaussiennes seront alors utilisées. Mais étant donné que le dernier article traite d'un sujet qui s'apparente beaucoup plus aux laboratoires terrestres qu'astronomiques, le Système International (SI) sera alors de mise.

Introduction

Lorsque Jeans émit, voilà bientôt un siècle, son "critère de masse" concernant l'effondrement d'un nuage de gaz pour la formation éventuelle d'étoiles (Jeans 1928), les astronomes savaient déja depuis belle lurette que les proto-étoiles originaient de tels nuages interstellaires. Ce critère peut être utilisé pour vérifier si une distribution de gaz, dans des conditions spécifiées par sa température et sa densité, sera stable sous l'effet de la gravité. Comme il le sera démontré à la section 1.1, son application aux nuages moléculaires observables dans notre Galaxie montre que pour la plupart d'entre eux, la force d'attraction gravitationnelle est suffisamment grande pour vaincre la pression thermique (Wynn-Williams 1992). La réalisation que la présence d'un champ magnétique pouvait apporter un support substantiel contre l'attraction gravitationnelle et présenter une alternative viable à l'épuisement rapide et invraisemblable d'une fraction importante de la matière interstellaire (tel que prédit par l'application du critère de Jeans), fut probablement un des premiers indices de son importance dans le processus qui mène à la formation d'étoiles.

Son omniprésence sera aussi reconnue par une brève revue des différentes étapes du "modèle standard" de la formation d'une étoile de faible masse tel que présenté à la Figure 1. La discussion précédente concernant le support magnétique, qui caractérise la première étape de contraction et de l'effondrement éventuel du nuage moléculaire, peut se résumer par l'introduction du concept d'une masse critique déterminée par la quantité de flux magnétique contenue à l'intérieur du nuage initial (Shu et al. 1993). Il y aura effondrement si la masse de ce dernier est supérieure à cette masse critique. Il est cependant important de noter que même dans le cas contraire, le phénomène de diffusion ambipolaire (définit par la séparation

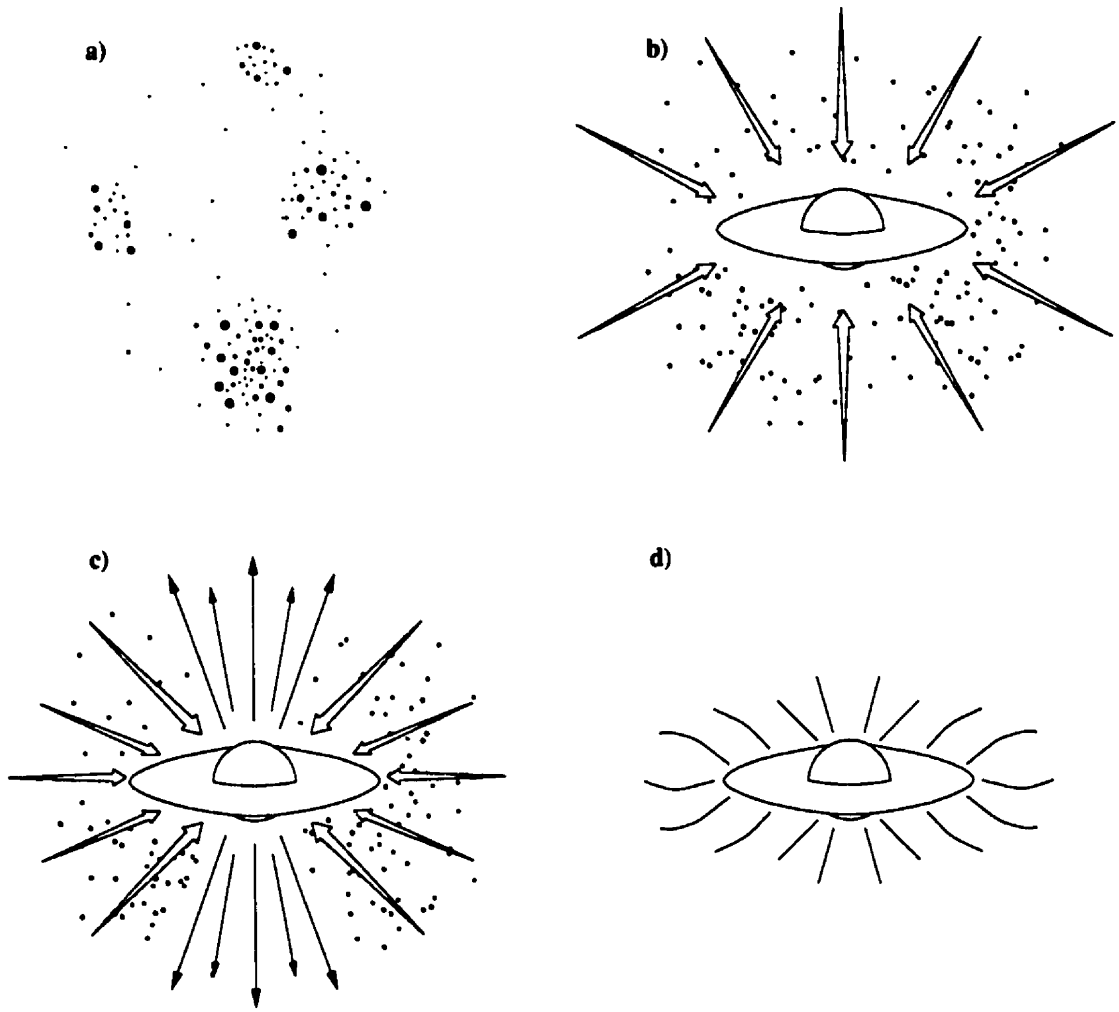

Fig. 1.— Les quatres étapes dans la formation d'une étoile de faible masse, selon Shu et al. (1993). a) effondrement gravitationnel. b) formation d'une proto-étoile et d'un disque d'accrétion. c) pertes de masse et apparition de jets bipolaires et d) fin de l'accrétion de masse et éclaircissement du système protostellaire.

graduelle des particules neutres et chargées causée par la présence du champ magnétique) pourrait éventuellement permettre un effondrement qui au préalable était impossible. La deuxième étape, caractérisée par l'effondrement du noyau protostellaire de l'intérieur vers l'extérieur ("inside-out collapse"), la création d'une proto-étoile et d'un disque d'accrétion, de même que la troisième avec ses pertes importantes de matière, de moment cinétique et la création de jets bipolaires (d'origine magnéto-hydrodynamique, voir Bachiller (1996)) sont celles qui correspondent le mieux à l'état de la majorité des sources étudiées dans ce travail (quoique plusieurs de ces objets correspondent à des régions massives de formation d'étoiles).

Par souci d'exhaustivité, mentionnons brièvement la dernière étape d'éclaircissement où le système disque/étoile devient visible dans les bandes proche-infrarouge, visuelle et ultraviolette. Quoiqu'une diminution de l'intensité du champ magnétique ait probablement un rôle à jouer dans cet éclaircissement (par un élargissement des jets bipolaires qui provoquerait le freinage de l'accrétion de matière), nous aurons peu à dire sur cette période de l'évolution protostellaire.

Nous montrerons, dans ce travail, que l'avènement de mouvements systématiques de matière en présence d'un champ magnétique a des conséquences observationnelles facilement détectables. Nous présenterons un résumé de notre étude dans les sections qui suivent, mais nous ferons auparavant un résumé des principales caractéristiques des nuages moléculaires où nous reprendrons certains des aspects que nous avons brièvement mentionnés dans les paragraphes précédents.

1. Les nuages moléculaires.

1.1. Effondrement gravitationnel.

Les nuages moléculaires pourraient être simplement définis comme étant une phase dans le processus de formation stellaire où la matière interstellaire se transforme et traverse une période plutôt froide, dense et relativement complexe. Une caractéristique fondamentale des nuages moléculaires est que, contrairement à la matière interstellaire diffuse et aux étoiles, ils ne peuvent être supportés uniquement par la pression thermique. Plus spécifiquement, une utilisation simple du théorème du viriel (sans les termes magnétique ou turbulent) montre que la masse critique minimale requise pour l'effondrement d'un nuage de température T et de densité de masse ρ est donnée par (Battaner 1996; Evans 1999):

$$M_J \simeq \left(\frac{\pi kT}{mG}\right)^{1.5} \rho^{-0.5} = 18 M_\odot T^{1.5} n^{-0.5} \ ,$$

où $\rho = mn$, avec m la masse moléculaire moyenne et n la densité volumique. M_J est bien entendu la masse de Jeans dont il fut question dans la section précédente. Lorsque l'équilibre est rompu et que l'effondrement prend place, en supposant qu'on puisse négliger le support magnétique et celui dû à la rotation, la pression interne ne sera pas suffisante pour freiner la contraction dans les cas où celle-ci s'effectue de façon isothermique (Spitzer 1978). Le temps de chute libre t_{ff} ("free-fall time") nous donne alors un ordre de grandeur pour le temps requis pour que l'effondrement s'effectue (Spitzer 1978; Evans 1999):

$$t_{ff} = \left(\frac{3\pi}{32 G \rho}\right)^{0.5} = 3.4 \times 10^7 n^{-0.5} \text{ ans.}$$

Il appert que la plus grande partie de la masse de gaz contenue dans les nuages moléculaires est stérile et que seulement une fraction de la matière totale sera impliquée dans la formation d'étoiles. Or, si nous posons $T = 10$ K et $n \geq 50$ cm^{-3} comme paramètres typiques

pour ces régions stériles , nous obtenons $M_J \leq 80\,M_\odot$ et $t_{ff} \leq 5 \times 10^6$ années. Étant donnée la masse gazeuse de $\sim 10^9\,M_\odot$ contenue dans la Galaxie (avec la majorité résidant dans des nuages massifs) nous obtenons un taux de formation stellaire $\frac{dM_*}{dt} \gtrsim 200\,M_\odot$ année^{-1}, ce qui est beaucoup plus élevé que la valeur moyenne récemment évaluée à 3 $M_\odot$ année^{-1}. Et si on ajoute le fait que la durée de vie typique d'un nuage est $\sim 10^7$ années, nous sommes dans l'obligation de conclure qu'il se doit d'exister d'autres agents de support s'opposant à l'attraction gravitationnelle (Evans 1999).

Puisque les nuages moléculaires sont sujet à un niveau d'ionisation non-négligeable causé par le champ de radiation interstellaire, il devient alors évident que la présence d'un champ magnétique sera susceptible d'affecter le phénomène de contraction et d'effondrement des nuages. Une nouvelle étude du théorème du viriel permet de se rendre compte que la présence d'un champ magnétique contribue un terme de pression magnétique qui joue un rôle similaire à la contrepartie thermique (Choudhuri 1998) et permet d'introduire le concept de masse critique présenté auparavant (Shu 1992; Battaner 1996):

$$M_B \approx \frac{\int \mathbf{B} \cdot d\mathbf{S}}{\sqrt{6\pi^2 G}} ,$$

où $\mathbf{S}$ réfère à la surface extérieur du nuage considéré. Un nuage de masse inférieure à M_B ne pourra initialement s'effondrer sous l'effet de sa propre gravité (si le champ est "gelé" dans le fluide composé des particules chargées). Bien entendu, le phénomène de diffusion ambipolaire pourra changer les données et permettre un effondrement éventuel. Le temps requis pour ce faire, qui dépend du niveau d'ionisation, sera de l'ordre de $\sim 10^6 - 10^7$ années (Spitzer 1978; Evans 1999), un nombre qui se compare bien à l'âge moyen d'un nuage typique cité plus haut.

Mais le théorème du viriel permet et prédit l'existence d'un autre terme qui s'ajoutera au support contrant l'effondrement, il s'agit du terme qui tient compte des mouvements de

matière à grande échelle (rotation, ...) et de la turbulence présente dans les nuages. En ce qui nous concerne, la combinaison de ces deux phénomènes (magnétique et turbulent) et leur interaction nous permettra d'arriver à des prédictions et conclusions intéressantes concernant la détection du champ magnétique dans les nuages moléculaires.

1.2. Détermination des paramètres physiques.

La tâche de déterminer les conditions physiques présentes dans les nuages moléculaires est rendue particulièrement ardue par le fait que leur composante majoritaire (i.e., l'hydrogène moléculaire H_2) est pratiquement invisible à l'observateur. Il fut donc impératif de développer d'autres méthodes de détection qui permettent de cerner certains des paramètres qui définissent l'état de la matière constituante.

1.2.1. La poussière.

La présence de poussière à l'intérieur des nuages moléculaires est une des raisons principales pour cette obscuration de l'hydrogène moléculaire, puisqu'elle absorbe la radiation ultraviolette qui témoignerait des transitions électroniques qui nous donneraient de l'information sur les conditions physiques internes existantes. Mais heureusement, elle peut aussi nous permettre d'évaluer certains paramètres importants tels la masse du nuage, la température des grains, ... comme nous le montrerons bientôt (Hildebrand 1983).

En supposant que les grains sont dans un état d'équilibre avec le champ de radiation ambiant, la quantité d'énergie absorbée dans l'ultraviolet se doit aussi d'être réémise sous forme de radiation dans le continu. Il est possible de montrer (Whittet 1992) que pour des grains de taille moyenne de l'ordre du micron, la vaste majorité de l'énergie sera libérée dans le domaine des longueurs d'ondes infrarouges et sous-millimétriques ($30\,\mu\text{m} \lesssim \lambda \lesssim 1000\,\mu\text{m}$).

À ces longueurs d'ondes, il est possible de prendre avantage de la petite taille relative des grains pour montrer que dans ce cas leur facteur d'efficacité d'émission Q_λ est simplement relié à la longueur d'onde (Whittet 1992):

$$Q_\lambda \propto \lambda^{-\beta} ,$$

où $1 \lesssim \beta \lesssim 2$ est un indice qui dépend de la nature des grains. En supposant de plus que l'opacité τ_β est faible, il appert que le flux de radiation F_λ détecté, et originant du nuage, est donné par:

$$F_\lambda = (1 - \exp(-\tau_\beta)) Q_\lambda B_\lambda (T_g) \Delta\Omega ,$$

avec T_g la température des grains, B_λ la fonction de Planck et $\Delta\Omega$ la dimension angulaire de la région considérée. En observant le nuage sur une large gamme de longueurs d'ondes, il est possible de modéliser l'équation précédente aux flux détectés et de déterminer ainsi la température T_g et l'indice β (et par le fait même l'opacité en fonction de la longueur d'onde). La Figure 2 montre un exemple d'un tel modèle pour le nuage moléculaire OMC2-FIR4. La courbe pleine montre le modèle de l'équation du flux superposé aux données alors que la droite brisée donne l'opacité aux différentes longueurs d'ondes. Ce modèle nous permet d'estimer la température des grains de poussière à ≈ 32 K et l'indice $\beta \simeq 1.15$.

En faisant certaines hypothèses concernant les paramètres des grains (entre autres pour leur dimension radiale a et leur densité ρ_g) et le ratio r de la masse totale de poussière à la masse gazeuse (Hildebrand 1983), il est possible de montrer que la masse du nuage est donnée par:

$$M = \frac{4\rho_g F_\lambda d^2}{3B_\lambda (T_g) r} \left(\frac{a}{Q_\lambda}\right) .$$

Dans le cas de OMC2-FIR4, nous avons obtenons ainsi $M \approx 15 M_\odot$ (avec $r^{-1} = 100$).

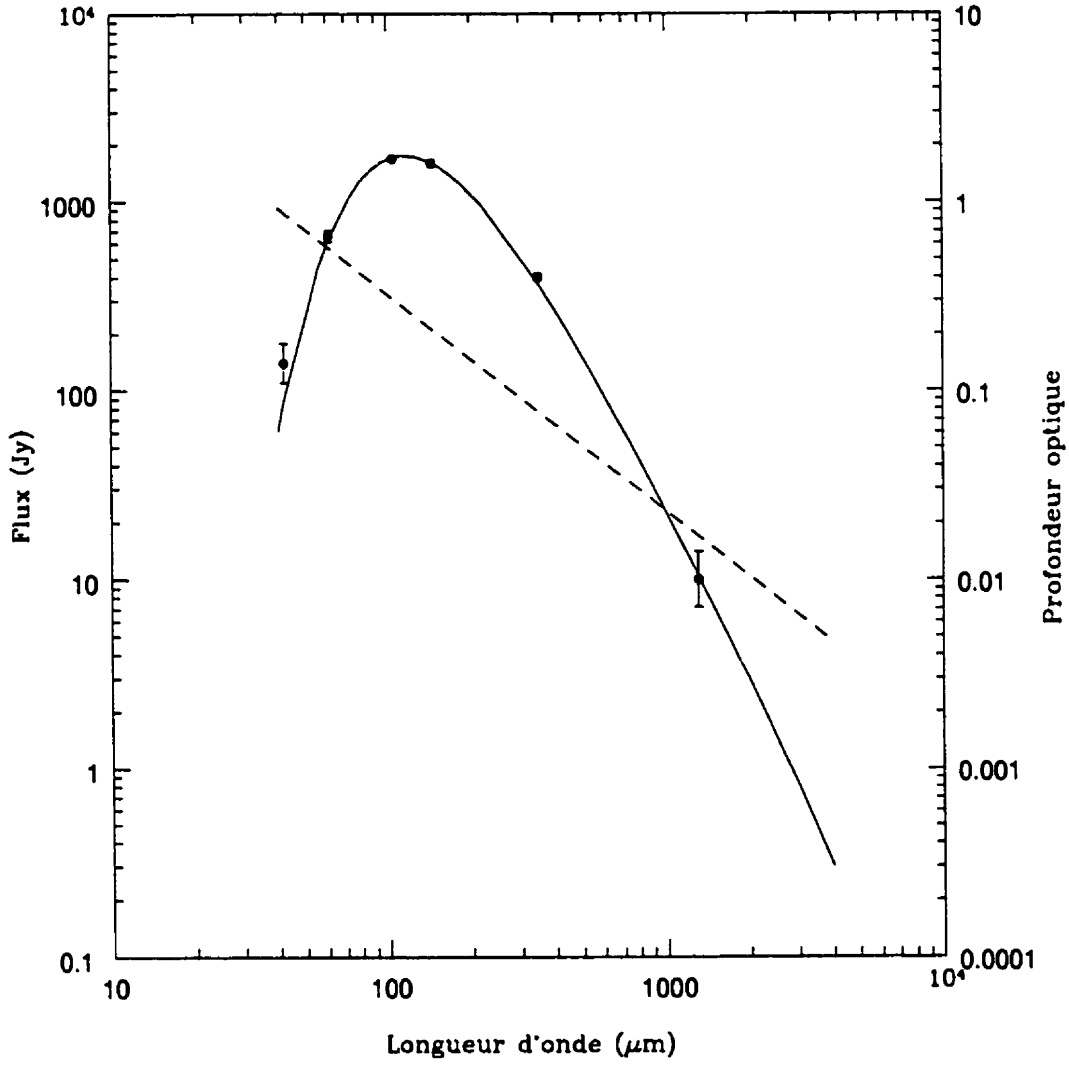

Fig. 2.— Courbes de flux (pleine) et d'opacité (brisée) des grains de poussière pour OMC2-FIR4. Le modèle donne un paramètre $\beta \simeq 1.15$ et $T_g \approx 32$ K. Les données sont de Thronson et al. (1978); Mezger et al. (1990); Lis et al. (1998). OMC2-FIR4 est situé à une distance de ≈ 450 pc.

Il est donc aisé de constater que la présence de poussière n'est pas nécéssairement qu'une nuisance mais aussi un outil de diagnostique important. Cela deviendra d'autant plus évident quand nous discuterons, dans les sections 2.1 et 2.2, de l'effet que la forme des grains peut avoir sur le niveau de polarisation de la radiation continue qui émane des nuages moléculaires.

1.2.2. Le gaz moléculaire.

Le spectre de rotation des molécules qui émettent dans les domaines millimétriques et sous-millimétriques est parfaitement adapté pour sonder les conditions physiques et les champs de vélocité régnant dans les nuages moléculaires et les régions avoisinantes aux proto-étoiles. À ces longueurs d'ondes, l'opacité de la poussière ambiante est négligeable (voir la Figure 2) et il est possible d'observer des régions situées à des profondeurs importantes qui sont autrement obscurcies à de plus courtes longueurs d'ondes. Bien sûr, l'abondance de la molécule utilisée peut limiter la profondeur observable accessible à l'observateur. Par exemple, la molécule la plus abondante (après l'hydrogène moléculaire H_2), le monoxyde de carbone CO, présente des raies qui sont opaques dans la direction du coeur des nuages moléculaires. Cependant, les espèces isotopiques qui lui sont associées, telles ^{13}CO ou $C^{18}O$, sont beaucoup moins abondantes et nous permettent d'observer plus loin à l'intérieur des nuages (les abondances isotopiques relatives dans le voisinage du soleil donnent les ratios suivants: $^{12}C/^{13}C \simeq 90$ et $^{16}O/^{18}O \simeq 490$).

Les raies opaques sont aussi très utiles (et utilisées) pour donner une mesure approximative et simple de la masse (habituellement avec CO, voir Scoville & Sanders (1987)) et de la température d'un nuage. Le premier estimé, qui n'est pas nécéssairement limité à l'observation de raies opaques, est dû à une application simplifiée du théorème du viriel (où le champ magnétique et les pressions externes sont négligés) qui nous donne la relation suivante (Choudhuri 1998; Evans 1999):

$$M \approx \frac{R(\Delta v)^2}{G} = 210 M_\odot R\,(\mathrm{pc})\,[\Delta v\,(\mathrm{km/s})]^2 \ ,$$

où R est le rayon de la région concernée et Δv une mesure de la largeur de la raie observée (pleine largeur à demi-hauteur dans l'expression de droite). La température peut être calculée à partir de la solution de l'équation de transfert radiatif dans les cas où on suppose qu'elle est constante à l'intérieur du nuage. La température de la raie T_r est alors donnée par (Rybicki & Lightman 1979):

$$T_r \simeq T_r\,(0) \exp(-\tau) + T\,(1 - \exp(-\tau)) \ ,$$

avec $T_r\,(0)$ est la température du champ de radiation à "l'arrière" du nuage. Il est aisé de voir que la température de la raie s'approche de la température du nuage lorsque l'opacité est élevée ($\tau \gg 1$).

L'utilisation de la combinaison d'une raie opaque et d'une raie transparente, ou encore de deux raies minces, nous permet d'évaluer d'autres paramètres. Prenons l'exemple où nous connaissons l'intensité (la température) d'une raie ^{12}CO (opaque) en plus de celle d'une raie C^{18}O (transparente) pour une transition donnée. En utilisation l'équation précédente, il est facile de montrer la relation suivante (en supposant $T_r\,(0)$ négligeable):

$$\frac{T_r\,(\mathrm{C^{18}O})}{T_r\,(^{12}\mathrm{CO})} \simeq 1 - \exp(-\tau_t) \ .$$

L'inversion de cette équation nous donne alors τ_t, l'opacité de la raie transparente. Il peut aussi être démontré que les températures de deux raies transparentes d'un isotope d'une espèce moléculaire sont aussi (relativement) simplement liées dans les cas où on suppose un équilibre thermodynamique local (ÉTL). Il est alors possible d'évaluer la température

d'excitation à laquelle est soumise cette espèce moléculaire et l'opacité de chacune des raies (Emerson 1996, p. 310).

Il est cependant de mise de préciser que l'hypothèse d'ÉTL n'est pas toujours valable. L'excitation des niveaux d'énergie de rotation d'une molécule est régie par ses nombreuses collisions avec le gaz environnant (composé en grande majorité d'hydrogène moléculaire) et possiblement par son interaction avec le champ de radiation local. La probabilité d'occupation d'un niveau d'excitation dépend de deux quantités: son niveau d'énergie et sa densité critique. La première quantité nous donne une indication de la température cinétique du gaz requise pour que les collisions soient suffisament énergétiques pour exciter un niveau donné, alors que la densité critique spécifie quand le taux d'excitation (ou de dé-excitation) dû aux collisions devient supérieur au taux d'émissions spontanées de photons par la molécule à partir de ce niveau. Ceci implique que pour des densités élevées (i.e., supérieures à la densité critique), les collisions dominent et les niveaux d'excitation adoptent une fonction de distribution de Boltzmann; l'hypothèse d'ÉTL est alors valide. Les niveaux d'excitation de molécules qui ont une densité critique suffisamment basse en comparaison avec la densité de gaz ambiant satisfont à cette condition. C'est presque toujours le cas pour la molécule de monoxyde de carbone qui a une densité critique $n_c \sim 10^4 - 10^5$ cm^{-3} dans les longueurs d'ondes sous-millimétriques alors que d'autres molécules telles HCN et HCO$^+$ (qui ont un moment dipolaire plus élevé et $n_c \sim 10^6 - 10^7$ cm^{-3}) ne rencontreront habituellement pas cette condition.

Enfin, ceci implique aussi que l'observation de molécules qui exhibent des densités critiques significativement différentes devrait nous permettre de sonder des régions de densité toutes aussi différentes. Nous en présentons un exemple à la Figure 3 avec des cartes d'intensité de OMC2-FIR4 pour les molécules ^{12}CO ($J \rightarrow 6 - 5$) ($n_c \sim 10^5$ cm^{-3}) et ^{12}CS ($J \rightarrow 7 - 6$) ($n_c \sim 10^7$ cm^{-3}) obtenues au Caltech Submillimeter Observatory (CSO). On

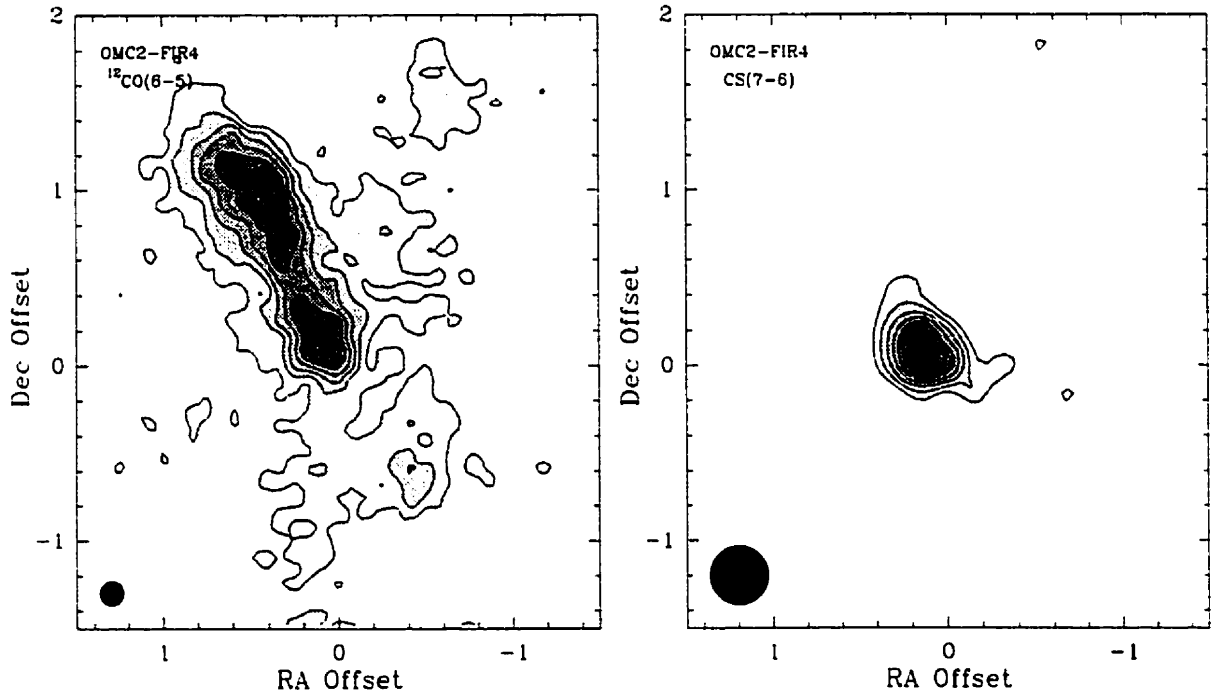

Fig. 3.— Cartes d'intensité ^{12}CO ($J \rightarrow 6-5$) (gauche) et ^{12}CS ($J \rightarrow 7-6$) (droite) du nuage moléculaire OMC2-FIR4. La largeur des faisceaux, montrée dans les coins gauches inférieurs, est de $\approx 8''$ et $\approx 20''$ respectivement.

peut voir que le monoxyde de carbone couvre une vaste région alors que le monoxyde de soufre n'est détecté qu'au coeur du nuage où la densité est probablement maximale.

2. Techniques de mesure du champ magnétique.

Dans cette section nous présentons une brève revue de quelques méthodes de détection du champ magnétique qui sont maintenant couramment utilisées. Ceci nous permettra de mieux comprendre les difficultés inhérentes à cette tâche et de juger de l'utilité de la nouvelle méthode de détection qui sera présentée dans ce travail.

2.1. Absorption dichroïque.

Il est maintenant bien établi que la présence de grains de poussière anisotropiques (par exemple de forme allongée) peut causer une polarisation linéaire dans le champ de radiation d'une source lumineuse, qu'on assume non-polarisée, placée à l'arrière plan de l'agglomération de grains (nuages moléculaires, plan de la Galaxie, ...).

Davis & Greenstein (1951) ont proposé une théorie d'alignment des axes de rotation principaux des grains avec le champ magnétique environnant. Dans le cas d'un grain paramagnétique (un grain pour lequel les composants de base ont un moment cinétique fini) ayant une géométrie allongée, la relaxation paramagnétique permet l'amortissement (et l'annulation) de la rotation selon deux des trois axes principaux. De plus, l'axe de rotation résultant sera celui possédant le plus grand moment cinétique (l'axe court si on suppose qu'une équipartition d'énergie fut atteinte).

Le procédé d'alignement est relativement compliqué mais peut être résumé de la façon suivante. La présence d'un champ magnétique **B** externe induit dans un grain paramagnétique une magnétisation **M** donnée par:

$$\mathbf{M} = \chi_o \mathbf{B} \, .$$

Dans le cas où l'amplitude du champ externe varie sinusoïdalement quand elle est vue dans le référentiel du grain (comme ce serait le cas s'il est en rotation par rapport au référentiel de l'observateur et de **B**), la susceptibilité magnétique χ_o est une quantité complexe. Dans ce cas, il est possible de montrer que le couple développé, agissant sur le grain, et le changement de l'énergie de rotation du grain sont donnés par:

$$\begin{aligned} \mathbf{T} &= \frac{d\mathbf{L}}{dt} &&= V\frac{\chi_i}{\Omega}((\mathbf{\Omega} \times \mathbf{B}) \times \mathbf{B}) \\ \frac{dE_r}{dt} = \mathbf{T} \cdot \mathbf{\Omega} &&&= -V\frac{\chi_i}{\Omega}(\mathbf{\Omega} \times \mathbf{B})^2 \ , \end{aligned}$$

où **L** est le moment cinétique, **T** le couple, E_r l'énergie de rotation, $\mathbf{\Omega}$ la vitesse angulaire de rotation, χ_i la partie imaginaire de la suceptibilité magnétique χ_o et V le volume du grain.

Une étude de ces équations nous montre que l'effet du couple paramagnétique est d'aligner **L** avec **B** et de réduire l'énergie de rotation à une valeur minimum tout en gardant constante la composante du moment cinétique parallèle au champ externe. Ceci ne peut être accompli dans le cas du type de grain considéré que s'il tourne selon son axe principal le plus court puisque ce dernier a le plus grand ratio de moment cinétique par rapport à l'énergie de rotation. "Le grain tourne de bout en bout".

Dans ce cas, si l'axe de rotation des grains alignés par le champ magnétique fait un angle non-nul par rapport à la ligne de visée entre la source lumineuse et l'observateur, il y aura une atténuation plus prononcée selon l'axe perpendiculaire à la projection du champ magnétique sur le plan du ciel. Autrement dit, le vecteur de polarisation est parallèle au champ.

Il est maintenant bien connu que la matière interstellaire produit ce genre de polarisation dans le champ de radiation émanant d'étoiles du plan galactique. Le phénomène fut bien étudié et une dépendance de la polarisation en fonction de la longueur d'onde (dans le visible et le proche infrarouge) fut déterminée empiriquement (Serkowski 1973; Whittet 1992). La polarisation maximum se situe habituellement entre 0.4 μm et 0.8 μm avec une moyenne de 0.55 μm. Ce type de polarisation peut aussi être observé dans la même bande pour des nuages moléculaires denses et la même dépendance en fonction de la longueur d'onde est alors mesurée.

L'interprétation des observations est souvent rendue difficile par la présence d'autres phénomènes comme la diffusion et l'émission de radiation synchrotron dans la même bande de fréquences. Dans le cas où ces complications peuvent être éliminées, les résultats permettent d'imposer des contraintes sur les modèles existants concernant la composition des grains de poussière (Hildebrand 1988).

Nous discuterons brièvement au chapitre 3 d'observations réalisées dans le passé (Cohen et al. 1984) qui utilisent cet effet pour mesurer l'alignement potentiel du champ magnétique avec les flots bipolaires dans l'environnement circumstellaire d'étoiles jeunes. Dans ces cas, une mesure des vecteurs de polarisation de la radiation provenant d'étoiles situées à l'arrière plan des flots fournit l'information nécéssaire.

2.2. Émission dichroïque.

L'émission de radiation par les grains de poussière dans l'environnement proto-stellaire n'a rien de surprenant, ce n'est qu'une conséquence directe de l'absorption d'énergie provenant du champ de radiation environnant. Si on suppose qu'un équilibre énergétique fut atteint, l'énergie absorbée par les grains sur toute la gamme de fréquences du spectre électromagnétique doit être réémise sous forme de radiation concentrée principalement dans les bandes

infrarouge, millimétrique et sous-millimétrique.

Il n'y a plus qu'un pas à franchir pour réaliser que si la géométrie des grains est telle que l'absorption est sélective, c'est-à-dire qu'il y a une polarisation telle que décrite auparavant, alors l'émission doit elle aussi être partiellement polarisée (Hildebrand 1988). En fait, un simple calcul permet de trouver une relation entre la polarisation due aux émissions P_{em} et la polarisation due à l'absorption P_{abs} à une longueur d'onde λ donnée. Dans le cas où $P_{abs} \ll 1$ et l'opacité $\tau \ll 1$, on peut montrer que (Hildebrand 1988):

$$P_{em}(\lambda) = -\frac{P_{abs}(\lambda)}{\tau_\lambda} ,$$

où la polarisation est définie en fonction de l'intensité I par:

$$P = \frac{I_{max} - I_{min}}{I_{max} + I_{min}} .$$

De par ces relations et la théorie de Davis & Greenstein (1951), il est facile de montrer que les vecteurs de polarisation pour l'émission et l'absorption sont orthogonaux. Il est important de prendre note que cette relation n'est valide que pour une longueur d'onde donnée; par exemple P_{em} peut grandement différer de $-\frac{P_{abs}}{\tau}$ si les observations sont faites dans des bandes de fréquences différentes. Cependant, si ces observations sont conduites dans une même région d'un nuage moléculaire, on peut s'attendre à ce que les vecteurs de polarisation soient orthogonaux si l'absorption et l'émission originent de la même population de grains.

La Figure 4 montre une carte de polarisation de NGC 2264 à une longueur d'onde de 350 μm obtenue au CSO avec le polarimètre Hertz (Dowell et al. 2000, 1998; Schleuning et al. 1997). Les niveaux de polarisation mesurés pour cet objet sont généralement inférieurs à 1 %, ce qui est en soi relativement faible. Il est commun d'obtenir des niveaux de polarisation plus élevés pour des sources du même type. Un autre exemple est présenté à la Figure 5 où une

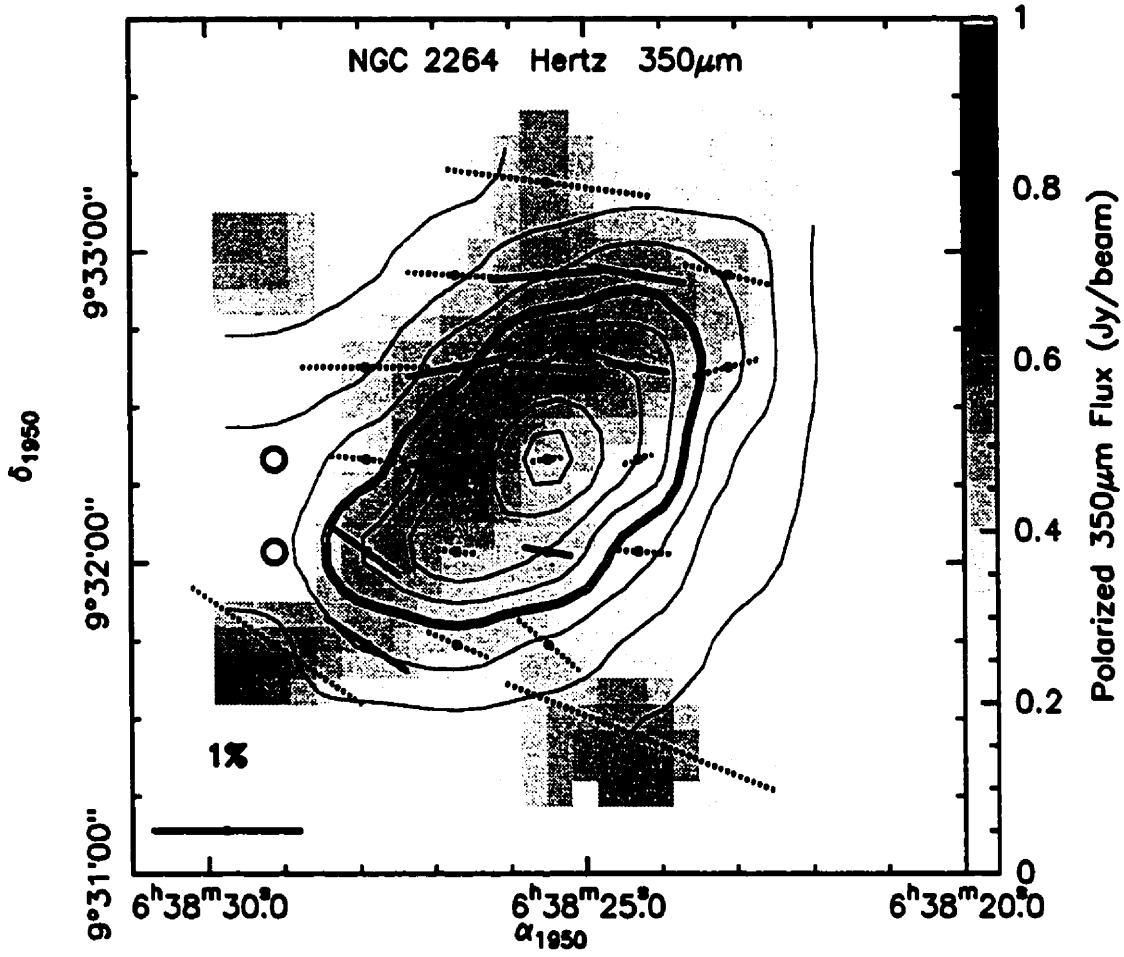

Fig. 4.— Carte polarimétrique de NGC 2264 à 350 μm obtenue au CSO avec le polarimètre Hertz (Dowell et al. 2000). Les niveaux de gris correspondent à l'intensité du flux polarisé, les contours au flux total et les traits aux vecteurs de polarisation (3-σ pour les traits pleins et 2-σ pour ceux en pointillé). Les cercles correspondent à un niveau de polarisation nul.

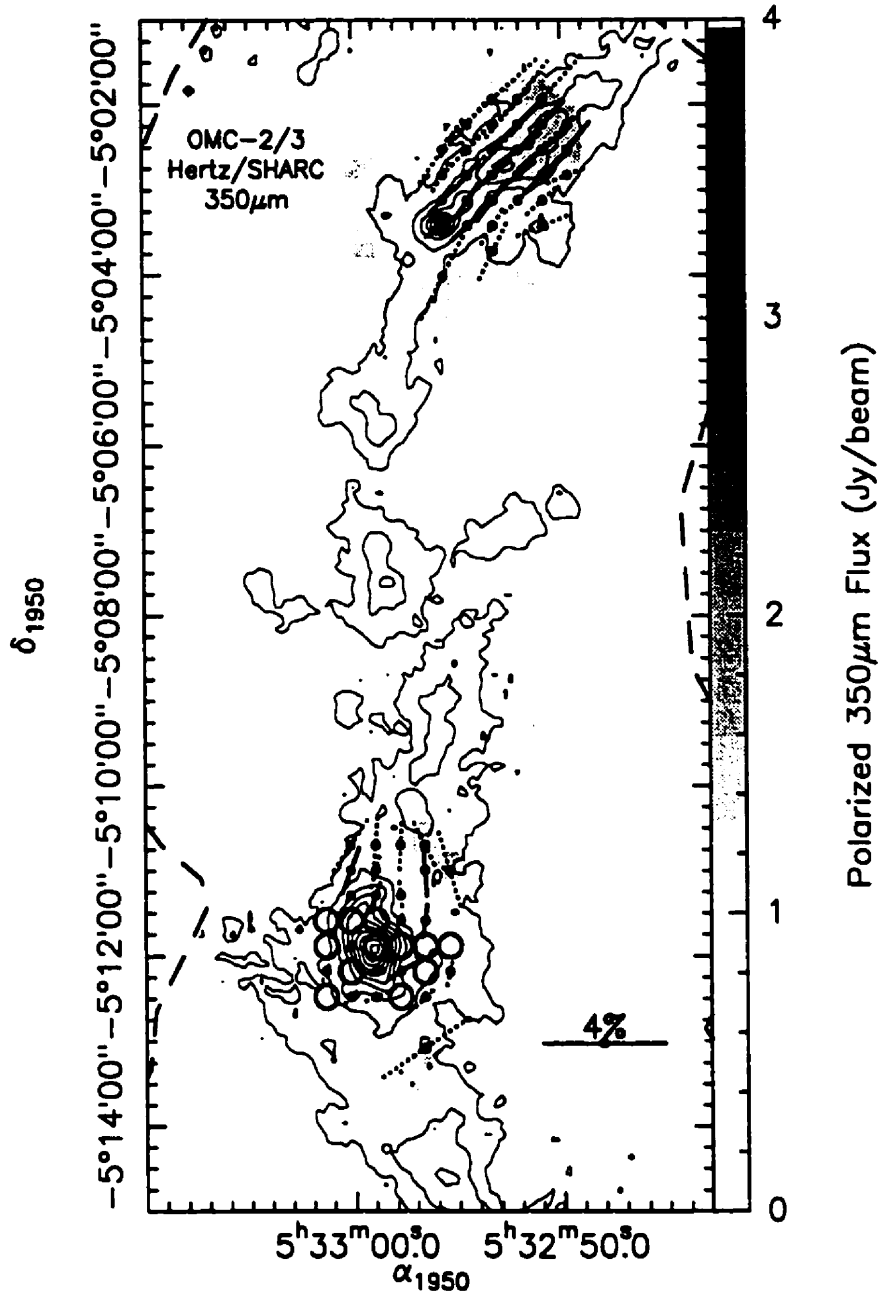

Fig. 5.— Carte polarimétrique de OMC2 (au sud) et OMC3 (au nord) à 350 μm obtenue au CSO avec le polarimètre Hertz (Dowell et al. 2000). Les niveaux de gris correspondent à l'intensité du flux polarisé, les contours au flux total et les traits aux vecteurs de polarisation (3-σ pour les traits pleins et 2-σ pour ceux en pointillé). Les cercles correspondent à un niveau de polarisation nul.

carte similaire est présentée pour les nuages moléculaires OMC2 et OMC3. Dans ce cas-ci, le niveau de polarisation varie grandement entre les deux objets. La polarisation est presque inexistante au coeur de OMC2-FIR4 alors qu'elle atteint un niveau respectable ($\approx 3-4$ %) autour de OMC3-MMS6. Comme les vecteurs de polarisation sont perpendiculaires à la composante du champ magnétique qui est tangente au plan de ciel, il est possible de discerner la géométrie à grande échelle de ce dernier. Le champ semble être orienté perpendicualirement à la direction privilégiée par le nuage d'Orion dans cette région alors que la situation est contraire dans le cas de NGC 2264 (Figure 4) où l'orientation du champ semble se mouler relativement bien à l'allure générale de ce nuage. Ces deux cartes donnent un bel exemple de l'utilité que peuvent avoir des observations semblables pour l'étude de la structure du champ magnétique dans les régions de formation d'étoiles.

Nous retrouverons ces trois objets un peu plus tard dans ce travail où nous présenterons et étudierons des spectres de raies d'émission obtenus pour plusieurs espèces moléculaires.

2.3. Polarisation de raies d'émission.

Les grains de poussière ne sont pas les seuls à émettre une radiation polarisée dans le domaine des longueurs d'ondes millimétriques et sous-millimétriques. En effet, Goldreich & Kylafis (1981, 1982) firent la prédiction que les raies interstellaires détectées dans cette même bande de fréquences devraient aussi présenter un certain niveau de polarisation (linéaire). Pour ce faire, certaines conditions sont cependant requises: i) le taux de transitions radiatives et le taux de collisions doivent être comparables (i.e., la densité ne doit pas être trop élevée) et ii) l'opacité de la source observée doit être de l'ordre de l'unité et anisotropique.

En plus de la détection du niveau de polarisation, il est aussi possible d'obtenir de l'information concernant l'orientation de son vecteur. Dans la limite du "champ fort" (i.e., lorsque la séparation Zeeman (voir la section 2.4) est supérieure aux taux de radiation et

de collisions), le vecteur de polarisation se devrait d'être parallèle ou perpendiculaire à la projection du champ magnétique dans le plan du ciel.

Après plusieurs essais infructueux, cet effet fut finalement confirmé par Greaves et al. (1999) qui ont détecté de faibles niveaux de polarisation ($\approx 0.5\% - 2\%$), dans la direction du centre galactique et du nuage moléculaire S140, à l'aide de raies d'émission de monoxyde de carbone (^{12}CO et ^{13}CO). Les prédictions théoriques semblent donc maintenant solidement vérifiées expérimentalement. Il est cependant probablement pertinent de noter qu'étant donné les conditions requises pour qu'une région observée se prête bien à de telles mesures (en particulier des niveaux modérés pour l'opacité et la densité), cette méthode de détection semble avoir une utilité quelque peu restreinte. Elle pourra cependant être complémentaire aux mesures de polarisation due à l'alignement des grains de poussière dans les régions où ceux-ci sont peu abondants. Ces endroits pourraient justement arborer des niveaux d'opacité favorables pour certaines espèces de molécules (telle ^{12}CO) qui sont habituellement trop abondantes dans le coeur des nuages moléculaires pour satisfaire les conditions requises et favorables à la détection de polarisation.

2.4. L'effet Zeeman.

Si les techniques d'observation discutées précédemment permettent de détecter la présence du champ magnétique dans les nuages moléculaires, elles ne permettent pas d'en évaluer l'intensité. En fait, il n'existe présentement qu'une seule méthode qui puisse nous permettre d'atteindre ce but: la mesure de l'effet Zeeman. Cette dernière se manifeste par une séparation des raies d'émission ou d'absorption causée par la présence du champ magnétique environnant et permet la détermination de la composante radiale de ce dernier.

Plus précisément, une raie spectrale à une fréquence ν_o donnée se verra scindée en trois composantes, par l'effet de Zeeman dit "normal" (Marion & Heald 1980), si la région de

formation de la raie est soumise à la presence d'un champ magnétique **B**. En plus de la raie originale à ν_o (qui sera polarisée longitudinalement), il y aura formation de deux raies supplémentaires à $\nu_o \pm \nu_z$ (avec polarisations circulaires) où:

$$\nu_z = BZ \ ,$$

avec Z le paramètre de sensibilité Zeeman (Crutcher 1999b). Dans le domaine de fréquences qui nous concerne, la séparation entre ces deux nouvelles raies et la raie principale sera beaucoup moindre que la largeur de cette dernière; on ne peut alors mesurer qu'un élargissement de la raie et non pas vraiment un scindage. La valeur du champ (où plutôt de sa composante qui est parallèle à la ligne de visée) est déterminée par une mesure des paramètres de Stokes V et I (qui spécifient, respectivement, l'intensité polarisée circulairement et l'intensité totale (Rybicki & Lightman 1979)). En fait ces deux quantités sont liées par la relation suivante:

$$V \simeq \frac{dI}{d\nu} \nu_z \cos(\theta) \ ,$$

où θ est l'angle fait entre la direction du champ magnétique et la ligne de visée. Il est maintenant aisé de voir qu'il est possible d'obtenir un estimé pour $B\cos(\theta)$ en comparant le spectre V avec la dérivée en fréquences du spectre I.

Parce que cette technique de mesure est sujette à plusieurs problèmes instrumentaux, il est préférable d'utiliser pour les observations des molécules qui possèdent plusieurs raies dans un intervalle de fréquence restreint. Pour cette raison, l'hydroxyle (OH) et le cyanure (CN) se sont avérés des candidats de choix (Crutcher 1999b). Les observations OH (faites en absorption à 1665 et 1667 MHz) tracent des régions de faible densité ($n \sim 10^3$ cm^{-3}) alors que les observations plus récentes réalisées avec la molécule CN ($\approx$ 113 GHz) sondent de plus grandes densités ($n \sim 10^6$ cm^{-3}). Les intensités de champ ainsi mesurées s'échelonnent généralement sur une plage allant de quelques dizaines jusqu'à plusieurs centaines de μG. Une compila-

tion des observations faites jusqu'à présent (Crutcher 1999a) permettent de tirer quelques conclusions. Entre autres, il semble y avoir indication que i) le ratio masse/flux magnétique est généralement suffisament grand pour suggérer que l'intensité du champ magnétique est trop faible pour supporter les nuages et que ii) la relation qui lie le champ magnétique à la densité est du type $B \propto \rho^{0.5}$ tel que prévu par la théorie (Shu 1992).

3. But de la thèse - une nouvelle méthode de détection du champ magnétique dans les nuages moléculaires.

Suite à cette brève revue de quelques méthodes de détection et de mesure du champ magnétique, nous présentons maintenant un résumé de la thèse qui a pour but principal l'élaboration et l'utilisation d'une nouvelle technique de détection du champ magnétique dans les nuages moléculaires.

3.1. Observations de raies opaques dans les nuages turbulents - chapitre 1.

Supposons une région donnée dans un nuage moléculaire où les mouvements de gaz se font de façon turbulente (comme lors des deuxième et troisième étapes de la Figure 1). Plus précisément, nous définissons deux modes différents de turbulence (Emerson 1996): un premier où les mouvements gazeux concernés s'établissent sur des distances qui sont plus grandes que la région où une raie observée se forme, et un deuxième où ces mouvements gazeux se situent sur des distances complètement contenues dans la région de formation de la raie. Le premier type de turbulence est connu sous le nom de macro-turbulence alors que le deuxième l'est sous celui de micro-turbulence.

Le chapitre premier ne concernera que l'étude d'objets qui exhibent des modes macro-turbulents. Quoique la question de l'interprétation et la compréhension de la nature de la

macro-turbulence est plutôt épineuse, plusieurs mécanismes de création de flots de matière sont connus et susceptibles d'en expliquer l'origine. Il est maintenant bien établi qu'en présence d'une proto-étoile, différents types de vents stellaires peuvent provenir de sa surface (Lamers & Cassinelli 1999). Deux d'entre eux sont particulièrement intéressants et peuvent aussi servir à démontrer l'importance de la présence des champs magnétiques dans l'environnement circumstellaire. Nous faisons ici allusion aux vents stellaires causés par des rotors magnétiques (qui requièrent une rotation de l'atmosphère stellaire et la présence de lignes ouvertes de champ) ainsi que des vents de type Alfvén (absence de rotation). Dans les deux cas, il est possible de démontrer que le mouvement de masses gazeuses émanant de la surface de l'étoile peut atteindre des vitesses terminales allant parfois jusqu'à plusieurs centaines de km/s. Ceci peut expliquer, entre autres, les grandes largeurs des raies souvent observées dans certains nuages moléculaires qui sont le site de formation d'étoiles massives, comme le cas du grand nuage de la nébuleuse d'Orion (OMC1) que nous aurons l'occasion d'étudier dans les deux premiers chapitres.

Le problème que nous considérons, et qui est au coeur de cette thèse, concerne l'effet que peut avoir la présence d'un champ magnétique sur l'apparence des profils de raies d'espèces moléculaires ioniques qui existent dans des régions caractérisées par des modes dynamiques tels que ceux décrits ci-haut. Les espèces considérées dans cette partie du travail seront l'oxomethylium (HCO^+) et le diazenylium (N_2H^+) qui seront comparés à une espèce neutre (HCN, le cyanure d'hydrogène) qui leur est possiblement coexistante. Nous présenterons des évidences théoriques et expérimentales qui démontrent que la présence d'un champ magnétique peut avoir un effet dramatique sur l'apparence des profils de raies ioniques. Plus précisément, l'étude du problème nous premettra d'arriver à trois conclusions principales:

- les espèces moléculaires ioniques montreront des profils spectraux plus étroits et une suppression significative des "ailes" ou composantes de haute vélocité, comparativement

aux spectres d'espèces neutres coexistantes, dans les cas où le champ magnétique moyen local est suffisamment puissant et s'il existe un manque d'alignement entre ce dernier et les flots de gaz présents dans la région concernée

- les spectres ioniques et neutres seront similaires dans les cas où il y a un alignement complet entre le champ magnétique moyen et les flots gazeux
- les spectres ioniques et neutres seront similaires dans les cas où la région étudiée est micro-turbulente ou en équilibre thermique.

Ces prédictions (particulièrement la première) sont importantes puisqu'elles sont susceptibles de suggérer des interprétations complètement différentes, ou tout au moins de modifier celles qui sont courantes, lors de l'utilisation de spectres de molécules ioniques pour l'étude des nuages moléculaires. Prenons comme exemples, le dépistage, avec l'aide de HCO^+, des enveloppes circumstellaires des proto-étoiles (Hogerheijde et al. 1997), l'étude des flots moléculaires (de l'anglais "molecular outflows") qui émanent du même type d'objets (Girart et al. 1999) et bien sûr, ce qui nous intéresse particulièrement, la détection de champs magnétiques.

Au niveau expérimental, la difficulté est de prouver que deux espèces moléculaires (dans notre cas, une ionique et une neutre) coexistent dans le milieu interstellaire. Nous présenterons donc des évidences qui justifient notre choix de molécules (nous adressons aussi ce problème dans le deuxième chapitre). Comme il le sera démontré, il semble que l'utilisation de la combinaison HCO^+/HCN soit amplement justifiée. Malheureusement, on ne peut arriver à la même conclusion lorsque N_2H^+ est comparé a HCN. Certains croient que cet ion est uniquement confiné à des régions dynamiquement plus calmes (Bachiller 1996, 1997), mais il est plus que probable que la cause principale relève d'une différence des abondances relatives (N_2H^+ étant moins abondant). Ceci ne nous cause cependant aucune difficulté puisque toutes nos conclusions peuvent être obtenues avec une seule espèce ionique (HCO^+).

Nous présenterons des spectres obtenus au CSO pour quatre objets bien connus (OMC1, OMC2-FIR4, OMC3-MMS6 et DR21OH) qui semblent confirmer notre première prédiction (à cet effet, un champ magnétique fut déjà mesuré pour deux d'entre eux, soit OMC1 et DR21OH, voir Crutcher (1999a)). Il est cependant important de noter que ces molécules sont suffisamment abondantes pour que les raies détectées soient probablement opaques. Comme il le sera expliqué sous peu, il est possible que ceci amène une certaine confusion dans l'interprétation des résultats. Il est donc préférable de faire une étude similaire avec des espèces qui exhibent des raies qui sont transparentes. Nous adressons cette question au deuxième chapitre.

3.2. Observations de raies transparentes et étude de nuages peu turbulents - chapitre 2.

Il n'est pas inconcevable que la question de l'abondance relative des espèces étudiées puisse apporter un certain niveau de confusion dans l'interprétation de nos résultats. Tel pourrait être le cas si, pour quelques raisons que ce soit, l'espèce neutre (HCN) était beaucoup plus abondante que l'espèce ionique (HCO^+). Ceci pourrait potentiellement résulter en une augmentation de l'importance relative des ailes de haute vélocité dans les profils des spectres de HCN, et par le fait même à une sous-estimation artificielle des largeurs de raies ioniques lorsque comparées à celles obtenues pour l'espèce neutre. L'abondance relative des espèces étudiées est donc importante.

Pour s'assurer qu'aucun effet semblable ne puisse brouiller les données, nous démontrerons dans le deuxième chapitre que les resultats obtenus sont à toute fin pratique inchangés lorsque des espèces ioniques et neutres peu abondantes sont observées. Pour ce faire, nous présenterons des observations similaires à celles du chapitre premier mais cette fois avec les molécules suivantes: $H^{13}CN$ (la molécule neutre), $H^{13}CO^+$, HCS^+ et H_3O^+ (les trois ions

considérés). De plus, nous élargirons considérablement notre échantillon d'objets. En effet, en plus des quatre nuages moléculaires étudiés au chapitre précédent, nous présenterons des spectres obtenus pour sept autres nuages, portant ainsi leur nombre total à onze.

Nous confirmerons cette méthode de détection de la présence d'un champ magnétique moyen dans les nuages moléculaires macro-turbulents et vérifierons que les résulats obtenus sont en accord avec ceux obtenus avec les raies opaques, et ce pour toutes les espèces moléculaires observées. De plus, en faisant certaines suppositions concernant la géométrie des objets observés, il nous sera possible de vérifier la tendance qu'ont le champ magnétique et les flots de matière gazeuse à s'aligner. Ceci peut être accompli en calculant la moyenne du rapport de la largeur de raie ionique à celle de la raie neutre (définies par leur déviation standard) sur l'ensemble des objets inclus dans notre échantillon. Nous conclurons que même si ce ratio peut varier de façon significative d'un objet à l'autre, il ne semble pas y avoir de tendance évidente qui nous force à croire à un alignement systématique.

Dans la dernière section du chapitre, nous considérerons les résultats obtenus par Benson et al. (1998) dans leur étude d'un grand ensemble de nuages froids et relativement denses où ils comparent des spectres obtenus pour l'ion N_2H^+ avec ceux de molécules neutres (NH_3, CCS et C_3H_2). Comparativement aux sources considérées précédemment, ces objets montrent des largeurs de raies qui sont beaucoup plus étroites. De plus, la plupart d'entre eux sont principalement supportés par leur pression thermique et exhibent des densités qui sont significativement moindres (par environ deux ordres de grandeur). De par ces différences, nous serions sûrement en droit à s'attendre à des résultats tout aussi différents.

En fait, les résultats obtenus par ces auteurs nous permettent de tester la dernière des prédictions faites au chapitre premier que nous réécrivons ici:

- les spectres ioniques et neutres seront similaires dans les cas où la région étudiée est micro-turbulente ou en équilibre thermique.

Nous démontrerons que, effectivement, les différences observées ne sont pas significatives et nous obtiendrons ainsi une autre validation en faveur de notre exposé.

3.3. Alignement entre champ magnétique et flots bipolaires dans les régions de formation d'étoiles - chapitre 3.

Nous savons déjà, selon le travail présenté dans les deux premiers chapitres, que les spectres ioniques et neutres seront similaires dans les cas où il y a un alignement complet entre le champ magnétique moyen et les flots gazeux présents dans une région macro-turbulente donnée. Or, ceci est particulièrement intéressant pour l'étude de proto-étoiles pour lesquelles nous pouvons observer des flots bipolaires qui originent de leurs pôles. C'est ce que nous ferons dans le troisième chapitre où nous étudierons en détails le cas du nuage moléculaire NGC 2071.

Si le coeur dense des sources macro-turbulentes est souvent difficile à interpréter (de par, entre autre, un manque de résolution; la plupart de nos observations furent obtenues avec un faisceau de 20″, soit $\sim$ 0.05 pc à la distance du nuage moléculaire d'Orion), il n'en va pas toujours de même pour les flots bipolaires qui souvent en émanent. De par sa nature et sa proximité relative, NGC 2071 est un objet qui se prête particulièrement bien au travail proposé. Effectivement, cet objet arbore d'importants flots bipolaires, facilement détectables (étant donnée une orientation favorable) et qui sont d'une dimension telle qu'ils ne posent aucun problème de résolution angulaire avec la dimension du faisceau utilisé (Girart et al. 1999).

Comme nous l'avons mentionné plus tôt, même s'il existe encore plusieurs inconnus dans l'interprétation de ce phénomène, les modèles les plus prometteurs pour l'explication des méchanismes à l'origine des flots bipolaires sont magnéto-hydrodynamiques de nature. Un point commun important qui existe entre les différents modèles est la prédiction de

l'alignement des flots bipolaires et du champ magnétique local (voir Bachiller (1996) pour une brève revue).

Nous montrerons que la ressemblance remarquable des profils spectraux entre les espèces neutre (HCN) et ionique (HCO^+) obtenus dans les flots bipolaires de NGC 2071 laisse peu de doute quant à l'applicabilité de cette prédiction pour cet objet.

3.4. Les grilles de polarisation - appendice.

Les grilles de polarisation sont souvent utilisées en radioastronomie. Une application très commune concerne leur utilisation pour la détection et la mesure du niveau de polarisation que possède la radiation qu'émettent les nuages de poussière dans le domaine du continu (Dowell et al. 1998; Schleuning et al. 1997). Comme il le fut discuté dans les section 2.1 et 2.2, cette polarisation origine probablement de la combinaison d'une anisotropie dans la géométrie des grains et de leur alignement avec le champ magnétique local (Davis & Greenstein 1951; Draine & Weingartner 1996). Or, quoique le travail présenté en appendice, concernant une étude approfondie du comportement des grilles de polarisation, n'est pas directement rélié au sujet central à cette thèse, il en demeure néanmoins pertinent. Et ce, d'autant plus qu'il s'agit d'un problème physique qui fait appel à des outils théoriques qui s'apparentent grandement à la théorie de Mie (van de Hulst 1957), un sujet pertinent à l'obtention d'un doctorat en physique.

Ce travail résulte de tests faits au Owens Valley Radio Observatory (OVRO) où plusieurs problèmes furent découverts lors de l'incorporation de telles grilles dans un système de polarimétrie pour les longueurs d'ondes millimétriques (Akeson et al. 1996; Akeson 1997). Une recherche de la littérature sur le sujet montra que les études et solutions existantes étaient souvent incomplètes et voir même erronées. Ce travail est donc important puisqu'il donne un solution analytique des équations de Maxwell appliquées au problème des grilles de po-

larisation. Plusieurs des résultats présentés sont nouveaux et apportent des simplifications significatives qui facilitent la spécification des paramètres optimaux requis pour une grille dans une application donnée.

Chapitre 1

Probing the magnetic field with molecular ion spectra - I [1]

Abstract

Observations of the effect of the magnetic field on its environment are usually achieved with techniques which rely on the interaction with the spin of the particles under study. Because of the relative weakness of this effect, extraction of the field characteristics proves to be a most challenging task. We take a totally different approach to the problem and show that the manifestation of the magnetic field can be directly observed by means of a comparison of the spectra of molecular ions with those of neutral molecules. This takes advantage of the strong cyclotron interaction between the ions and the field, but requires the presence of flows or turbulent motion in the gas. We compare our theory to data obtained on the OMC1, OMC2, OMC3 and DR21OH molecular clouds.

Subject headings: ISM: cloud — ISM: magnetic field — ISM: molecules

1. Introduction.

The suspected effects of the magnetic field in the process of star formation are well documented in the literature. They may occur during the initial collapse of clouds, by

---

[1]Houde, M., Bastien, P., Peng, R., Phillips, T. G., and Yoshida, H. 2000, ApJ, 536

providing frictional support through collisions between ions and neutrals, or through the establishment of a pressure associated with long wavelength magnetohydrodynamic waves arising from small scale fluctuations in the field, or again as source of magnetohydrodynamic forces at the center of the molecular outflow phenomenon (Shu et al. 1987; Mouschovias 1991a,b; Crutcher et al. 1993). The need for accurate measurements of the magnetic field and its effects on the environment cannot be understated. This is, however, a formidable task. Up to now, the observed manifestations of the magnetic field, in star forming regions, consist of Zeeman line broadening measurements (which are best carried out at low frequencies, due to the increasing dominance of the Doppler width over Zeeman splitting with increasing frequency) and in the magnetic alignment of the dust grains known to exist in molecular clouds.

Despite the weakness of the interaction between the field and the observed molecular species and the numerous difficulties inherent to the technique, Zeeman measurements provide us with the only way of measuring the intensity of the magnetic field (more specifically its component normal to the plane of the sky (Crutcher et al. 1993, 1999)). On the other hand, a measure of the degree of alignment of the grains can be obtained from the level of linear polarization detected from continuum emission emanating from molecular clouds. The polarization is believed to be caused by anisotropic emission from dust grains. Recent studies (Hildebrand et al. 1999; Draine & Weingartner 1996) reveal that the intensity of the magnetic field has very little to do with the level of polarization induced by the dust. The field is needed to align the grains and the level of polarization is basically a function of the spin imparted to the individual grains by some agent, most likely the radiation field. The thermally generated spin is known to be too small to explain the observed effect (Draine & Weingartner 1996).

In this paper, we present theoretical and observational evidence for a different effect

which demonstrates the presence of the magnetic field. Its signature resides in the line profiles of molecular ion species at millimeter and submillimeter wavelengths. It will be shown that, under the right conditions, even a weak field ($\sim$ 10 μG) will cause ions to exhibit narrower profiles and a suppression of high velocity wings when compared to the lines of neutral species.

There are of course several possible effects that could confuse the issue, including optical depth differences between species and lack of spatial coexistence. We deal with such problems in part in this paper and in more depth in a subsequent one.

2. Ion spectra versus neutral spectra.

Probably the first thing we should point out is that the lines observed in molecular clouds are usually many times broader than their thermal width. It is generally assumed that this is due to the presence of turbulence in the interstellar medium (Zuckerman & Evans 1974; Falgarone & Phillips 1990). This will be the point of view adopted here. Turbulence is characterized by vortex streaming, the motions taking place in eddies of different sizes (Tennekes & Lumley 1972). In what follows, we will concentrate on a small portion of a given eddy so that the region considered is small enough that motions of the local flow can be approximated as being linear, with the understanding that on a larger scale the motion exhibits vorticity. This analysis can be applied without approximation to cases involving linear flows (e.g., jets, outflows, ...).

The effect to be discussed is the tendency for ions to be forced into gyromagnetic motion about the magnetic field direction, rather than following the streaming flow of the general neutral motion. It is necessary to discuss the ion-neutral collisions and we start with a simplified approach. We will assume that we are dealing with a weakly ionized plasma, where the neutral flow is mainly composed of molecular hydrogen; we therefore assume a

molecular mass number of $A_n = 2.3$ for its constituents.

2.1. Approximate solution - head on collisions.

The equation of motion of a single ion subjected to a flow of neutral particles in the presence of a magnetic field is given by:

$$\frac{d\mathbf{v}}{dt} = \frac{e}{m_i c}\mathbf{v} \times \mathbf{B} + \mathbf{F}_c \,, \tag{1.1}$$

where m_i, $\mathbf{v}$, $\mathbf{B}$ are the mass of the ion, its velocity and the magnetic field. $\mathbf{F}_c$ is the force (per unit mass) on the ion due to the collisions with neutrals. The nature of the interaction during a collision can be quite complicated and how the momentum is transfered between the particles needs to be handled carefully. But in order to get an idea of the behavior of the ion we will initially assume that all the collisions are perfectly elastic and "head on". Accordingly, the force of interaction can be approximated by:

$$\mathbf{F}_c = -2\frac{\mu}{m_i}(\mathbf{v} - \mathbf{v}^n) \sum_{m=-\infty}^{\infty} \delta(t - \tau_m) \,, \tag{1.2}$$

where μ, $\mathbf{v}^n$, τ_m are the reduced mass, the neutral flow velocity and the different times at which collisions randomly occur. It will make things easier if we break up the velocities into two components, one parallel to the mean magnetic field ($\mathbf{v}_{||}$ and $\mathbf{v}^n_{||}$) and the other perpendicular ($\mathbf{v}_\perp$ and $\mathbf{v}^n_\perp$). In steady state conditions, it can be shown that the mean and variance of the velocity components are given by (see the appendix for details):

$$\langle \mathbf{v}_{||} \rangle \;=\; \langle \mathbf{v}^n_{||} \rangle \tag{1.3}$$

$$\langle \mathbf{v}_\perp \rangle = \frac{\langle \mathbf{v}_\perp^n \rangle + \langle \omega_r \rangle^{-1} \left[\langle \mathbf{v}_\perp^n \rangle \times \langle \vec{\omega_g} \rangle \right]}{1 + \left(\frac{\langle \vec{\omega_g} \rangle}{\langle \omega_r \rangle} \right)^2} \tag{1.4}$$

$$\sigma_\parallel^2 = \frac{\left[\sigma_\parallel^n \right]^2}{\left[\frac{m_i}{\mu} - 1 \right]} \tag{1.5}$$

$$\sigma_\perp^2 = \frac{\left\langle |\mathbf{v}_\perp^n|^2 \right\rangle - \langle \mathbf{v}_\perp \rangle^2}{\left[\frac{m_i}{\mu} - 1 \right]} \tag{1.6}$$

$$\sigma_T^2 = \sigma_\parallel^2 + \sigma_\perp^2 \tag{1.7}$$

with

$$\langle \vec{\omega_g} \rangle = \frac{e \langle \mathbf{B} \rangle}{m_i c} \tag{1.8}$$

$$\langle \omega_r \rangle = 2 \frac{\mu}{m_i} \nu_c \tag{1.9}$$

$\langle \omega_r \rangle$ is what we will call, for reasons to be discussed later, the relaxation rate. $\langle \vec{\omega_g} \rangle$, ν_c are the mean ion gyrofrequency vector and the (mean) collision rate.

Equation (1.4) represents the drift that the ion can possess in relation to the neutral flow and it is at the heart of the effect that we are now studying. Equation (1.6) gives a measure of the gyration amplitude of the ion around a guiding center in the region occupied by the magnetic field. We have also allowed for an inherent velocity dispersion in the neutral flow as can be seen by the presence of the term $\sigma_\parallel^n$ and the fact that $\left\langle |\mathbf{v}_\perp^n|^2 \right\rangle \neq \langle \mathbf{v}_\perp^n \rangle^2$.

From equations (1.3)-(1.7) it can be deduced that, as could be expected, the ion completely follows the flow when the latter is aligned with the field ($\mathbf{v}_\perp^n = 0$). More interesting, however, is the ion behavior when the neutral flow is perpendicular to the field ($\mathbf{v}_\parallel^n = 0$). In such cases, the following observations can be made:

- for weak field intensities ($\langle \omega_g \rangle \ll \langle \omega_r \rangle$) the ion follows the flow as $\langle \mathbf{v}_\perp \rangle \sim \langle \mathbf{v}_\perp^n \rangle$

- as the field gains in strength the ion starts to drift in a direction perpendicular to both the flow and the field until we get to the point where $\langle \mathbf{v}_\perp \rangle \sim 0$ when the field reaches high intensities ($\langle \omega_g \rangle \gg \langle \omega_r \rangle$). The ion is then basically trapped in the field and its mean square velocity can be evaluated solely with equation (1.6), $\sigma_\perp$ is found to be smaller than the flow velocity by a factor of a few. For example, if we choose $A_i = 29$ and $A_n = 2.3$ for the ion and neutral molecular mass numbers we find this factor to be ~ 3.5. That is, *an ion would have on average an effective velocity at least* ~ 3.5 *times smaller than that of a neutral molecule of the same mass.*

This last observation has important implications. Let us assume that an observed emission line from a neutral molecular species is composed of contributions from a family of flows (or eddies) of different velocities. We can then infer that *for regions inhabited with a strong enough magnetic field which is, on average, not aligned with the local flow(s), we expect ionic lines to exhibit narrower profiles and a suppression of high velocity wings when compared to neutral lines.*

Obviously, we cannot expect all the flows to be perpendicular to the mean magnetic field. In any given case, there will be a distribution in the value of the angle existing between the directions of the flows and the field. We have only considered the extremities of this distribution (flows aligned or perpendicular to the mean field direction), in general for a given angle both velocity components ($\mathbf{v}_\parallel$ and $\mathbf{v}_\perp$) would have to be simultaneously included in the analysis. The total resulting effect observed will, in general, reside somewhere in between what is obtained for these special cases.

It is also important to note that this phenomenon will only be observable in regions where the motions of the neutral particles do not have a zero mean velocity, i.e. $\langle \mathbf{v}^n \rangle \neq 0$. For, if they did, equations (1.5) and (1.6) would have exactly the same form and the velocity dispersions would be the same for ions and neutrals. In other words, *a thermal (or*

microturbulent) line profile would not show any manifestation of the presence of the magnetic field.

2.2. Refined solution.

It can be seen from equations (1.4), (1.6) and (1.9) that the amplitude of the effective velocity not only depends on the mean magnetic field strength but also on the amount of momentum transfered during a collision. It is therefore important to solve the problem for the more realistic cases where the collisions are not necessarily "head on". We, however, still retain the assumption that all are perfectly elastic.

We now we get for the mean velocities and dispersions:

$$\langle \mathbf{v}_{\parallel} \rangle = \langle \mathbf{v}_{\parallel}^{n} \rangle \tag{1.10}$$

$$\langle \mathbf{v}_{\perp} \rangle = \frac{\langle \mathbf{v}_{\perp}^{n} \rangle + \langle \omega_r \rangle^{-1} \left[\langle \mathbf{v}_{\perp}^{n} \rangle \times \langle \vec{\omega_g} \rangle \right]}{1 + \left(\frac{\langle \vec{\omega_g} \rangle}{\langle \omega_r \rangle} \right)^2} \tag{1.11}$$

$$\sigma_{\parallel}^2 = \frac{\left[\langle |\mathbf{v}_{\perp}^{n}|^2 \rangle - \langle \mathbf{v}_{\perp} \rangle^2 \right] M(a,\gamma) + \left[\sigma_{\parallel}^{n} \right]^2 N(a,\gamma)}{\left[\frac{2\langle a\cos(\gamma) \rangle}{\langle a^2 \rangle} - 1 \right] D(a,\gamma)} \tag{1.12}$$

$$\sigma_{\perp}^2 = \frac{\left[\langle |\mathbf{v}_{\perp}^{n}|^2 \rangle - \langle \mathbf{v}_{\perp} \rangle^2 \right] P(a,\gamma) + \left[\sigma_{\parallel}^{n} \right]^2 Q(a,\gamma)}{\left[\frac{2\langle a\cos(\gamma) \rangle}{\langle a^2 \rangle} - 1 \right] D(a,\gamma)} \tag{1.13}$$

$$\sigma_{T}^2 = \frac{\left[\langle |\mathbf{v}_{\perp}^{n}|^2 \rangle - \langle \mathbf{v}_{\perp} \rangle^2 \right] + \left[\sigma_{\parallel}^{n} \right]^2}{\left[\frac{2\langle a\cos(\gamma) \rangle}{\langle a^2 \rangle} - 1 \right]} \tag{1.14}$$

where:

$$D(a,\gamma) = 2\langle a\cos(\gamma) \rangle - \langle a^2 \cos^2(\gamma) \rangle + \frac{1}{2} \langle a^2 \sin^2(\gamma) \rangle$$

$$M(a,\gamma) = \frac{\langle a\cos(\gamma) \rangle}{\langle a^2 \rangle} \langle a^2 \sin^2(\gamma) \rangle$$

$$
\begin{aligned}
N(a,\gamma) &= \left[\frac{2\langle a\cos(\gamma)\rangle}{\langle a^2\rangle} - 1\right]\langle a^2\cos^2(\gamma)\rangle + \frac{1}{2}\langle a^2\sin^2(\gamma)\rangle \\
P(a,\gamma) &= D(a,\gamma) - M(a,\gamma) \\
Q(a,\gamma) &= D(a,\gamma) - N(a,\gamma)\ .
\end{aligned}
$$

The relaxation rate is now given by:

$$\langle\omega_r\rangle = \langle a\cos(\gamma)\rangle\,\nu_c\ . \tag{1.15}$$

a is the ratio of the change in velocity of the ion after a collision to the initial relative velocity between the two particles, γ is the scattering angle of the ion as measured in its initial rest frame and the different averages ($\langle a\cos(\gamma)\rangle$, ...) are evaluated over the space of the scattering angle of the colliding neutral particle in the same frame of reference. We give in Table I set of values for the different averages for two different ion molecular masses ($A_i = 29$ and 45). We would also like to point out that from numerical calculations we obtain the following relations (which could also be derived from simple physical considerations):

$$
\begin{aligned}
\langle a\cos(\gamma)\rangle &\simeq \frac{\mu}{m_i} \\
\frac{2\langle a\cos(\gamma)\rangle}{\langle a^2\rangle} &= \frac{m_i}{\mu}
\end{aligned}
$$

which allow us to see that our first evaluation of the relaxation rate in equation (1.9) was wrong by a factor of two whereas the denominator in equation (1.14) for σ_T^2 is unchanged. Another difference between equations (1.12)-(1.13) and (1.5)-(1.6) is that we now have a "mixing" between the two variances; the neutral dispersion parallel (perpendicular) to the magnetic field affects the ion velocity dispersion perpendicular (parallel) to the field. This is of course due to our more realistic treatment of the collisions where momentum can now be

transfered between different directions. But despite these few changes, all the conclusions reached in the previous section still hold.

In Figure 6, we have plotted curves for the ion effective velocity (according to equations (1.10)-(1.15)) as a function of the mean magnetic field intensity when $\left\langle \mathbf{v}_{\parallel}^{n} \right\rangle = 0$, $|\langle \mathbf{v}_{\perp}^{n} \rangle| = 10$ km/s and the neutral density $n = 5{\times}10^{6}$ cm^{-3}. For simplicity, we also set $\left\langle |\mathbf{v}^{n}|^{2} \right\rangle = \langle \mathbf{v}^{n} \rangle^{2}$. As can be seen, the field makes its presence felt even for relatively weak intensities ($\langle B \rangle \gtrsim 10\,\mu$G) and the transition between the regimes where ions follow the neutral flow to where they are trapped by the field is quite abrupt ($1\,\mu\text{G} \lesssim \langle B \rangle \lesssim 10\,\mu\text{G}$). It is important to point out that it is, in principle, possible to evaluate the mean intensity of the magnetic field from this Figure. One would have to compare the width of neutral and ion spectra and find the field strength that matches it at a given angle between the direction of the field and the line of sight to the observer. When this line of sight is parallel (perpendicular) to the field, the ion velocity should follow the curve for $\sqrt{\left\langle \mathbf{v}_{\parallel}^{2} \right\rangle}$ ($\sqrt{\langle \mathbf{v}_{\perp}^{2} \rangle}$). There are, however, a few things that stop us from achieving this. Among these are the unknown amount of velocity dispersion inherent to the neutral flow and the uncertainty in the neutral density (used to determine the collision rate). We should also point out that recent observations indicate that field strengths in molecular clouds are in the range of a few hundreds μG (Crutcher et al. 1999) where our curves in Figure 6 are basically flat and the ion velocity is insensitive to field

	$A_i = 29$	$A_i = 45$
$\langle a\cos(\gamma) \rangle$	0.07734	0.05028
$\langle a^2\cos^2(\gamma) \rangle$	0.00778	0.00332
$\langle a^2\sin^2(\gamma) \rangle$	0.00359	0.00157
$\langle a^2 \rangle$	0.01137	0.00489

Table I: Numerical values for the different averages present in equations (1.10)-(1.15) for ion molecular masses of 29 and 45.

strength variations. But we should not rule out the possibility that the determination of the field properties could become feasible in the future when using more complete models. Still at this point, it is nonetheless possible to assign a lower value for the field strength (given the density of the gas).

3. Observational evidence.

We would now like to bring support to our assertion of the previous section that we should expect that in certain conditions ion lines should have narrower profiles than neutral species. Furthermore, we contend that this situation is likely to happen frequently. The reason for this lies with equations (1.10)-(1.11).

As we recall, the requirement is for a poor alignment between the local magnetic field and the "mean" flow; the effect being maximized when they are perpendicular to each other. Assuming that the magnetic field is strong enough, we can see from the aforementioned equations that ions in general will not follow the motion of the flow but will tend to drift away in a direction perpendicular to it. But since the total mean ionic velocity is minimal when the flow and the field are perpendicular to each other, charged particles will be more likely to aggregate in regions where this is the case. It is therefore very tempting to define two groups of objects (as far as the observation of the effects of the magnetic field is concerned):

1. the field is aligned with the flow, no significant differences between the spectra of comparable neutral and ion
2. no general alignment between the field and the flow(s), the ion species exhibit narrower line profiles and suppression of the high velocity wings in their spectra.

In what follows, we present observational evidence showing some examples that we believe

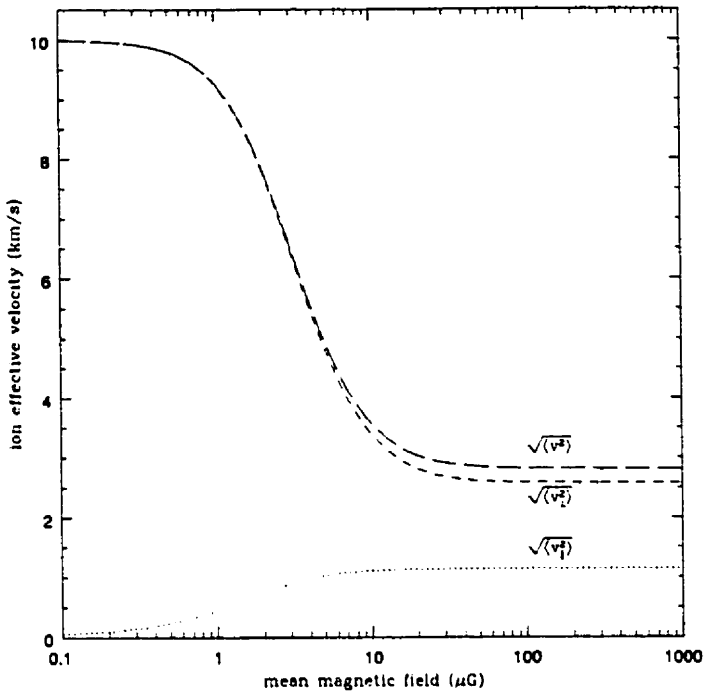

Fig. 6.— Ion effective velocity ($\sqrt{\left\langle \mathbf{v}_{\parallel}^2 \right\rangle}$, $\sqrt{\langle \mathbf{v}_{\perp}^2 \rangle}$ and $\sqrt{\langle \mathbf{v}^2 \rangle}$) as a function of the mean magnetic field strength when $\mathbf{v}_{\parallel}^n = 0$, $|\mathbf{v}_{\perp}^n| = 10$ km/s, $n = 5 \times 10^6$ cm^{-3} and $A_i = 29$.

object	coordinates (1950)		σ_v (km/s)		
	RA	DEC	HCN	HCO^+	N_2H^+
OMC1	$5^h32^m47^s.2$	-05°24′25″.3	17.42	3.23	1.87
OMC2-FIR4	$5^h32^m59^s.0$	-05°11′54″.0	3.59	2.72	1.34
OMC3-MMS6	$5^h32^m55^s.6$	-05°03′25″.0	1.40	0.71	0.56
DR21OH	$20^h37^m13^s.0$	42°12′00″.0	5.75	4.61	2.08

Table II: Comparisons of line widths (standard deviations σ_v) between HCN, HCO^+ and N_2H^+ for the four objects presented in Figure 7.

belong to the second class.

3.1. Observations of HCN, HCO^+ and N_2H^+.

In HCN, HCO^+ and N_2H^+ we have three fairly similar molecules except for the obvious fact that the last two are ions whereas the first is a neutral. Indeed, they are all linear molecules with comparable atomic mass, similar rotation spectra and almost identical critical densities ($n_c \sim 10^6$ cm^{-3}). They therefore appear to be excellent candidates to test our proposal.

We present in Figure 7 spectra of these three molecules in the $J \rightarrow 3-2$ transition for OMC1 and $J \rightarrow 4-3$ for OMC2-FIR4, OMC3-MMS6 and DR21OH obtained at the Caltech Submillimeter Observatory with the 200-300 GHz and 300-400 GHz receivers. The observations (including the maps presented in Figure 8) were done on several nights during the months of March, April, June and August 1999. Pointing was checked at regular interval using scans made on planets available at the time. Telescope efficiencies were calculated to be ≈ 70 % for the 200-300 GHz receiver (beam width of $\approx 32''$) and ≈ 60 % for the 300-400 GHz receiver (beam width of $\approx 20''$).

As can be seen from Figure 7, all these spectra show the characteristics described earlier; the ion lines are all significantly narrower than the HCN lines and the suppression of the wings is also obvious. These conclusions are made more definite in Table II where we present a comparison of the line widths (more precisely the standard deviations σ_v) of the species for these molecular clouds. The widths were measured after the lines were modeled with a multi-Gaussian profile. We interpret the fact that the predictions made here on the differences in the appearance in the spectra between comparable neutral and ion molecular species seem to be easily observable in molecular clouds as strong evidence in favor of our assertions.

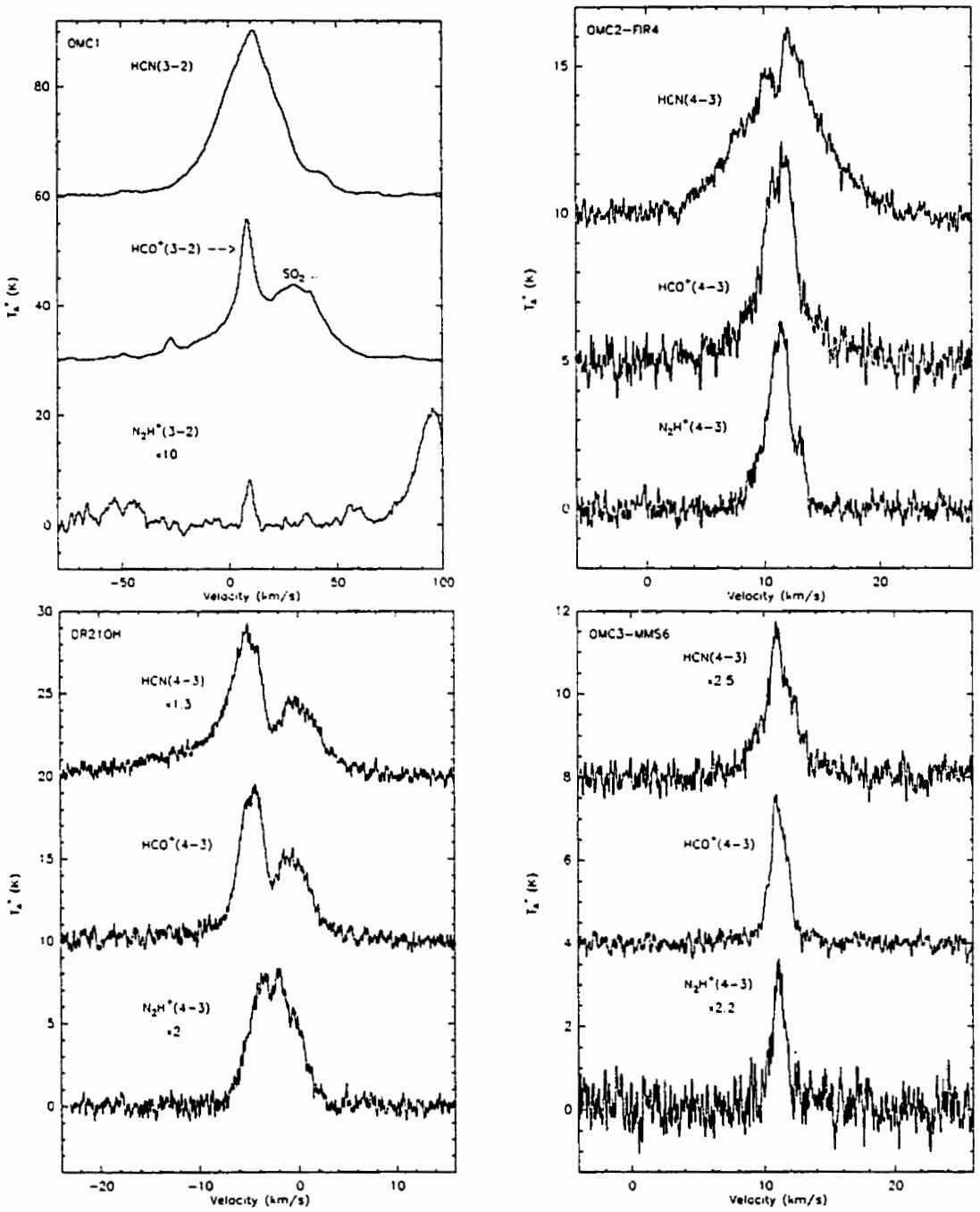

Fig. 7.— HCN (top), HCO^+(middle) and N_2H^+ (bottom) observations at the center position of (clockwise starting from top left): OMC1, OMC2-FIR4, OMC3-MMS6 and DR21OH. The bump at $\sim$ 30 km/s in the middle spectrum of OMC1 is a contamination from other species (SO_2, $^{13}CH_3CN$, ...).

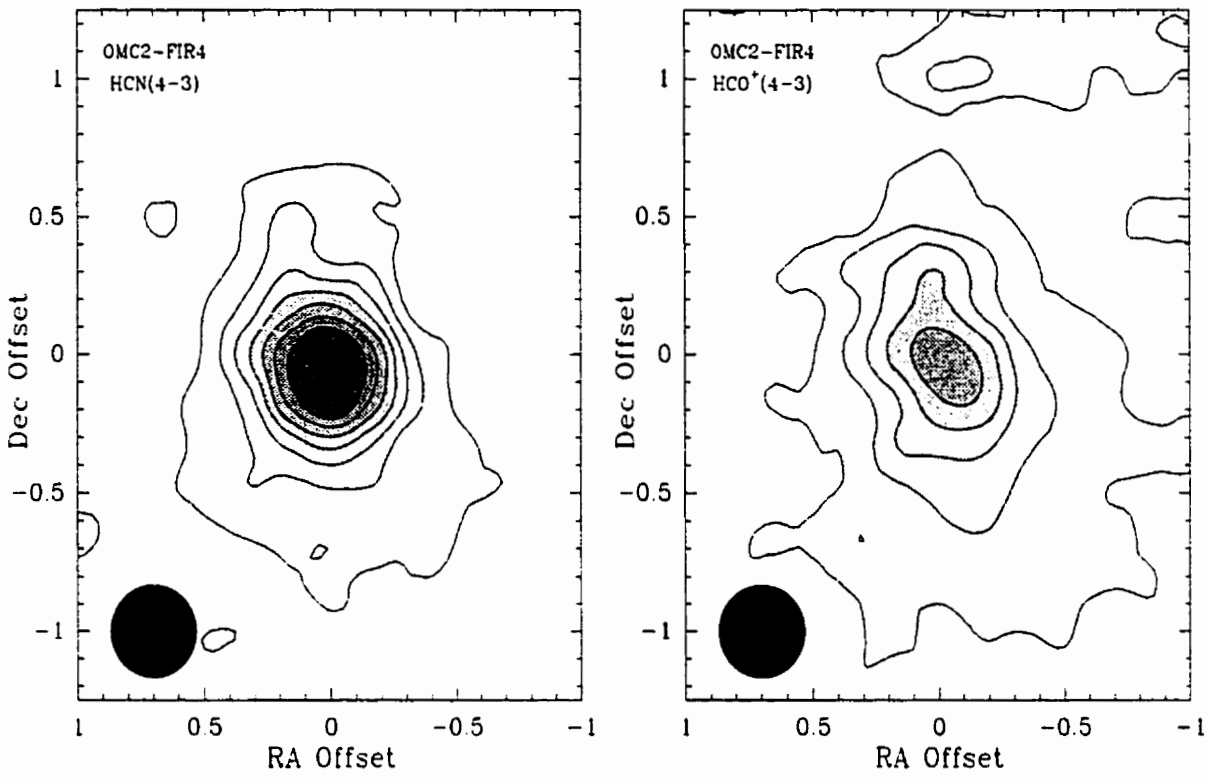

Fig. 8.— HCN and HCO^+ ($J \rightarrow 4-3$) maps of OMC2-FIR4. Although the ion spatial distribution appears somewhat more extended, the two peaks are well aligned and the HCN and HCO^+ systematic velocities agree (from Figure 7). The two maps have the same lowest contour level of 5 K·km/s ($\approx 10\sigma$) and the following levels increase linearly with an interval of 5 K·km/s. The maps' grid spacing of 10″ is half of the beam width (shown in the lower left corners). The pointing accuracy is better than $\approx 5''$.

We should however point out that the differences between the line profiles of neutral and ion species could be partly due to other factors. Indeed, the assumed coexistence of the different molecular species is not necessarily correct. Although we tried to choose ion and neutral species that are as similar as possible, it is likely that their observations sample different parts of the molecular clouds. In some cases, it might even be possible that two species are exposed to significantly different dynamical processes that could cause one of them to exhibit a narrower or larger line profile no matter what the effect of the magnetic field might be. Maps of the different molecular species for a given object could shed some light on this question. In the case of OMC1, Ungerechts et al. (1997) have extensively mapped the Orion molecular cloud (around OMC1) with 20 different chemical and isotopic molecular species. Amongst other things, they find an impressive degree of uniformity in the chemical abundances; but most interesting to us is how similar their maps of HCN and HCO^+ are ($J \rightarrow 1-0$, beam width of $\approx 50''$). On the other hand, N_2H^+ seems to have a very different spatial distribution (see their Figure 2). We also present in Figure 8 our maps of OMC2-FIR4 in HCN and HCO^+ ($J \rightarrow 4-3$) done at the CSO. Although the ion species appears somewhat more extended, the two peaks are well aligned. This and the fact the two species have similar line center velocity (see Figure 7) brings support to the coexistence assumption for these molecules in the OMC2 cloud.

The question of abundances is also important. For example, a given species could exhibit more opaque lines which could change some characteristics of the line profiles (such as the relative importance of the high velocity wings, saturation or self-absorption). In fact, we believe that the differences between the spectra of N_2H^+ and HCO^+ are probably the result of this effect (see the case of DR21OH in Figure 7, the self-absorption feature at ≈ -2.5 km/s is much weaker in the N_2H^+ spectrum implying a lower abundance).

Chemical differentiation could also play a role in explaining the differences between

spectra. In this effect, we expect that our analysis only applies to long-lived ion species (like the protonated molecules considered here), other more reactive species (CO^+, SO^+, ...) should more or less behave as neutrals as almost every collision in which they are involved would entail a chemical reaction (Schilke 1999).

4. Relaxation time and interaction between charged particles.

In our analysis of the problem in section 2, we have considered the behavior of a given ion without taking into account the presence of any other charged particles. One might intuitively guess that for a weakly ionized plasma, like the ones probed with our observations at the CSO presented in the last section, it is probably safe to do so.

One can make sure of this by comparing the mean time between collisions for charged particles in such a plasma with the time it takes an ion to relax to its steady state after being excited to a different velocity. The excitation could occur, for example, during a collision with an electron. However, because of the huge disparity between the masses of the two particles, it is unlikely that the ion would be much perturbed by such an encounter. A collision with another ion is more likely to produce a significant change in its velocity.

At any rate, it turns out that the ion relaxation time is given by the reciprocal of the relaxation rate defined by equation (1.15), as one can verify when solving the equation of motion (1.1) for a mean collision force $\langle \mathbf{F}_c \rangle$. The solution shows that the ion velocity decays exponentially with a time constant equal to $\langle \omega_r \rangle^{-1}$. When this time is compared to the mean collision time between ions, it is seen to be at least a few orders of magnitude smaller. Our simplified analysis is therefore justified.

5. Conclusion.

We argue that the presence of a magnetic field in a weakly ionized plasma can be easily detected through a comparison of ion and neutral line profiles. More precisely, we expect ion lines to often exhibit narrower profiles and significant suppression of high velocity wings. We have presented observational evidence obtained for four different molecular clouds which agrees with our theory.

Because of the low intensities of field required for the effect to be noticeable, we expect the phenomenon to be widespread. However, regions where the mean magnetic field is aligned with the neutral flow(s), or where the line width is dominated by the thermal width, should not show any significant differences between comparable neutral and ion spectra. These aspects of the problem will be treated in subsequent papers.

We thank Prof. J. Zmuidzinas for his help during the preparation of this paper. M. Houde's work was done in part with the assistance of grants from FCAR and the Département de Physique of the Université de Montréal. The Caltech Submillimeter Observatory is funded by the NSF through contract AST 9615025.

Appendix - Derivations.

Equations (1.3) and (1.4) can be easily derived by taking the mean of the equation of motion (1.1) and then assuming a steady state:

$$\left\langle \frac{d\mathbf{v}}{dt} \right\rangle = 0$$

Using equation (1.2) as an approximation for the force of interaction between ions and neutrals we get from the mean equation of motion:

$$\langle \mathbf{F}_{c\parallel} \rangle = 0 \tag{1.16}$$

$$\langle \mathbf{F}_{c\perp} \rangle = -\frac{e}{m_i c} \langle \mathbf{v}_\perp \rangle \times \langle \mathbf{B} \rangle \tag{1.17}$$

with

$$\langle \mathbf{F}_c \rangle = -2\frac{\mu}{m_i} \nu_c \left(\langle \mathbf{v} \rangle - \langle \mathbf{v}^n \rangle \right) \tag{1.18}$$

where ν_c is the mean collision rate. From equation (1.16) and (1.18) it is straightforward to get equation (1.3) for $\langle \mathbf{v}_\parallel \rangle$. Equation (1.17) can be transformed to:

$$\langle \mathbf{v}_\perp \rangle = -\frac{\langle \omega_r \rangle}{\langle \vec{\omega_g} \rangle^2} \left[\left(\langle \mathbf{v}_\perp \rangle - \langle \mathbf{v}_\perp^n \rangle \right) \times \langle \vec{\omega_g} \rangle \right]$$

into which we can insert equation (1.17) using (1.18) and finally get equation (1.4) which we rewrite here:

$$\langle \mathbf{v}_\perp \rangle = \frac{\langle \mathbf{v}_\perp^n \rangle + \langle \omega_r \rangle^{-1} \left[\langle \mathbf{v}_\perp^n \rangle \times \langle \vec{\omega_g} \rangle \right]}{1 + \left(\frac{\langle \vec{\omega_g} \rangle}{\langle \omega_r \rangle} \right)^2} \tag{1.19}$$

$\langle \vec{\omega_g} \rangle$ and $\langle \omega_r \rangle$ are defined in equation (1.8) and (1.9) respectively.

Equations (1.5) and (1.6) for the velocity dispersions can be derived by using the following procedure. We concentrate on the equation for $\sigma_\perp^2$. If we assume that the time of interaction during a collision is infinitively small, we can express $\mathbf{v}'_\perp$, the ion velocity (perpendicular to the field) immediately after a collision, as a function of the velocity $\mathbf{v}_\perp$ just before the collision:

$$\mathbf{v}'_\perp = \mathbf{v}_\perp + \frac{\Delta \mathbf{p}_\perp}{m_i} \tag{1.20}$$

with $\Delta \mathbf{p}_\perp = -2\mu(\mathbf{v}_\perp - \mathbf{v}_\perp^n)$ the change in the ion momentum. Upon taking the mean of the square of equation (1.20) while once again imposing steady state conditions, i.e. $\langle|\mathbf{v}'_\perp|^2\rangle = \langle|\mathbf{v}_\perp|^2\rangle$, we are left with:

$$\left\langle \mathbf{v}_\perp \cdot \frac{\Delta \mathbf{p}_\perp}{m_i} \right\rangle = -\frac{1}{2}\left\langle \left| \frac{\Delta \mathbf{p}_\perp}{m_i} \right|^2 \right\rangle . \tag{1.21}$$

Taking into account the fact that $\langle \mathbf{v}_\perp \rangle \cdot \langle \mathbf{v}_\perp^n \rangle = \langle \mathbf{v}_\perp \rangle^2$, as can be verified with equation (1.19), it is then straightforward to obtain:

$$\sigma_\perp^2 = \frac{\langle|\mathbf{v}_\perp^n|^2\rangle - \langle \mathbf{v}_\perp \rangle^2}{\left[\frac{m_i}{\mu} - 1\right]} . \tag{1.22}$$

The equation for $\sigma_\parallel^2$ follows from the same procedure.

The more refined set of equations (1.10)-(1.15) can also be obtained in similar fashion but the task is rendered somewhat more complicated by the fact the interaction force $\mathbf{F}_c$ is not simply given by equation (1.2). We will omit their derivation here as they are somewhat lengthy and don't bring anything substantially new to the discussion.

One last word concerning the energetics involved in the collision process. From the above discussion, it is apparent that an ion which starts off with the same velocity as the neutral flow would eventually settle into a steady state of lower kinetic energy (assuming a strong magnetic field). Once again focusing on the approximate head-on collision model as seen in the reference frame of the observer, we can understand this loss of energy by noting that the drag force felt by the ion (equation (1.2)) is proportional to the relative velocity between the colliding particles. As the ion is attempting to travel in a circular orbit around a given guiding center, this relative velocity is greater when it is going upstream (and losing energy through collisions) than when it is going downstream (and gaining energy from the

collisions). This will lead, on average, to a net loss of energy over a complete orbit.

Chapitre 2

Probing the magnetic field with molecular ion spectra - II[1]

Abstract

We present further observational evidence in support of our earlier proposal (Houde et al. 2000a) for detecting the presence of the magnetic field in molecular clouds by comparing spectra of molecular ions with those of neutral molecules. The ion lines tend to be narrower and do not show the wings due to flows, when the magnetic field is sufficiently strong. We obtained spectra for the optically thin lines of the $H^{13}CN$ and $H^{13}CO^+$ species in a sample of ten molecular clouds and found the results to be in agreement with our previous observations of the main isotopic species, HCN and HCO^+, made in OMC1, OMC2, OMC3 and DR21OH, thus eliminating the possibility of optical depth effects playing a role in the ion line narrowing. HCS^+ was also detected in four of these star forming regions. We also discuss previously published results by Benson et al. (1998) of N_2H^+ detections in a large sample of dark clouds. We show that the similarity in line widths between ion and neutral species in their sample is consistent with the relatively small amount of turbulence and other flows observed in these clouds.

Subject headings: ISM: cloud — ISM: magnetic field — ISM: molecules

---

[1]Houde, M., Peng, R., Phillips, T. G., Bastien, P., and Yoshida, H. 2000, ApJ, 537

1. Introduction.

In a previous paper (Houde et al. 2000a, hereafter Paper I), we argued that the presence of a magnetic field in a weakly ionized plasma can be detected through comparisons between ion and neutral molecular line profiles. It was shown that, for regions inhabited with a sufficiently strong magnetic field, we expect ions to exhibit narrower line profiles and a significant suppression of high velocity wings in cases where there is non-alignment between the mean field and the neutral flow(s). A further condition is that the flow(s) involved (which could also exist in the form of vorticity, i.e. turbulence) must not have a local zero mean velocity. For a Maxwellian gas velocity distribution there will be no effect.

As supporting evidence for our assertions, we presented observations of HCN, HCO^+ and N_2H^+ for the OMC1, OMC2, OMC3 and DR21OH molecular clouds obtained at Caltech Submillimeter Observatory (CSO). In each instance, we observed the effect described above. One could, however, argue that if for some reason the lines of the neutral species were to be significantly more opaque than their ionic counterparts, the differences in the line profiles between the neutrals and ions could simply be the result of greater saturation of the neutral lines rather than the presence of the magnetic field. It would then appear necessary to verify the effect on less abundant species which are more likely to exhibit optically thin lines. This paper addresses this question by presenting detections of $H^{13}CN$ and $H^{13}CO^+$ in a group of ten molecular clouds, including the four studied in Paper I. Furthermore, HCS^+ was also detected in four of them: OMC3, DR21OH, S140 and W3 IRS5. These detections are important in that they provide comparisons of another ion with a suitable neutral species. We also present HCN, HCO^+ and N_2H^+ data for L1551 IRS5. This brings to eleven the number of objects studied so far.

As will be shown, the same effects are observed with the less abundant isotopic species ($H^{13}CN$ and $H^{13}CO^+$); the ion species generally exhibiting narrower line profiles and signif-

icantly suppressed wings.

Another argument that could be used to counter our assertions is the importance that chemical differentiation can have on the spectral appearance of different molecular species. In fact, dramatic abundance variations between species have been observed in some molecular cores, as in the case of L1498 (Kuiper et al. 1996), and one might worry that species with different spatial distributions would also exhibit different velocity profiles. But as will be shown, the consistent success of our specific physical model in predicting the relative narrowing of the ion lines renders the need for such chemical postulate less immediate. Moreover, a case can be made against chemical differentiation being the dominant factor in explaining the relative line widths. For example, why are the observed ion lines always narrower, not broader often? Why are the ion lines narrower in cases where the spatial distributions are shown to be the same? Certainly many factors must be taken into account in order to explain the differences in the velocity profiles, but our model's success in answering questions like these forces us to emphasize the fact that the presence of the magnetic field is most important and, therefore, should not be neglected.

In the last section of the paper, we discuss recent N_2H^+ observations of dense cores in dark clouds (Benson et al. 1998). As these cores exhibit, on average, narrow line profiles ($\Delta v \approx 0.4$ km/s) and are believed to be primarily thermally supported, they provide us with a good opportunity to test the assertion made in Paper I that there should not be any significant differences between the widths of ion and neutral molecular lines in regions of low turbulence and void of flows.

2. Ion velocity behavior.

It was shown in Paper I that it is possible to calculate the components of the effective velocity of an ion subjected to a flow of neutral particles in a region inhabited with a magnetic

field. Under the assumptions that the flow is linear, the plasma is weakly ionized and that all collisions between the ion and the neutrals are perfectly elastic, we get for the mean and variance of the ion velocity components:

$$\langle \mathbf{v}_{\|} \rangle = \langle \mathbf{v}_{\|}^n \rangle \tag{2.1}$$

$$\langle \mathbf{v}_{\perp} \rangle = \frac{\langle \mathbf{v}_{\perp}^n \rangle + \langle \omega_r \rangle^{-1} \left[\langle \mathbf{v}_{\perp}^n \rangle \times \langle \vec{\omega_g} \rangle \right]}{1 + \left(\frac{\langle \vec{\omega_g} \rangle}{\langle \omega_r \rangle} \right)^2} \tag{2.2}$$

$$\sigma_{\|}^2 = \frac{a \left[\langle |\mathbf{v}_{\perp}^n|^2 \rangle - \langle \mathbf{v}_{\perp} \rangle^2 \right] + b \left[\sigma_{\|}^n \right]^2}{\left[\frac{m}{\mu} - 1 \right]} \tag{2.3}$$

$$\sigma_{\perp}^2 = \frac{g \left[\langle |\mathbf{v}_{\perp}^n|^2 \rangle - \langle \mathbf{v}_{\perp} \rangle^2 \right] + h \left[\sigma_{\|}^n \right]^2}{\left[\frac{m}{\mu} - 1 \right]} \tag{2.4}$$

$$\sigma_T^2 = \frac{\left[\langle |\mathbf{v}_{\perp}^n|^2 \rangle - \langle \mathbf{v}_{\perp} \rangle^2 \right] + \left[\sigma_{\|}^n \right]^2}{\left[\frac{m}{\mu} - 1 \right]} \tag{2.5}$$

with

$$\langle \vec{\omega_g} \rangle = \frac{e \langle \mathbf{B} \rangle}{mc} \tag{2.6}$$

$$\langle \omega_r \rangle \simeq \frac{\mu}{m} \nu_c \tag{2.7}$$

$$[\sigma^n]^2 = \langle |\mathbf{v}^n|^2 \rangle - \langle \mathbf{v}^n \rangle^2 \tag{2.8}$$

m and μ are the ion mass and the reduced mass. The ion and neutral flow velocities ($\mathbf{v}$ and $\mathbf{v}^n$) were broken into two components: one parallel to the magnetic field ($\mathbf{v}_{\|}$ and $\mathbf{v}_{\|}^n$) and another ($\mathbf{v}_{\perp}$ and $\mathbf{v}_{\perp}^n$) perpendicular to it. $\langle \omega_r \rangle$, $\langle \vec{\omega_g} \rangle$ and ν_c are the relaxation rate, the mean ion gyrofrequency vector and the (mean) collision rate.

Under the assumption that the neutral flow consists mainly of molecular hydrogen and has a mean molecular mass $A_n = 2.3$, we get $a \simeq 0.16$, $b \simeq 0.67$, $g = 1 - a$ and $h = 1 - b$ (these are functions with a weak dependence on the ion and neutral masses, the values given here apply well to the different ion masses encountered in this paper).

In the "strong" magnetic field limit ($\langle\omega_g\rangle \gg \langle\omega_\tau\rangle$), the previous set of equations is simplified by the fact that the ion gets trapped in the magnetic field, this implies that $\langle \mathbf{v}_\perp \rangle \sim 0$ (by equation (2.2)). This condition is probably easily met in a typical cloud where the required magnetic field strength, which scales linearly with the density, can be calculated to be $\langle B \rangle \gtrsim 1\,\mu$G for a density of $\sim 10^6$ cm^{-3}.

Upon studying the implications of these equations, we developed three expectations concerning the differences between the line profiles of coexistent ion and neutral species:

- for regions inhabited with a strong enough magnetic field which is, on average, not aligned with the local flows ($\left\langle \mathbf{v}_{||}^n \right\rangle$ is not dominant), we expect ionic lines to exhibit narrower profiles and a suppression of high velocity wings when compared to neutral lines since $\langle \mathbf{v}_\perp \rangle \sim 0$

- there should be no significant differences between the line profiles when the flows and the mean magnetic field are aligned as the ion velocity is completely determined by $\langle \mathbf{v}_{||} \rangle$ (or equivalently $\left\langle \mathbf{v}_{||}^n \right\rangle$)

- a thermal (or microturbulent) line profile would not show any manifestation of the presence of the magnetic field since the mean velocity of the neutral flow is zero.

We refer the reader to Paper I for more details.

2.1. Line widths and profiles.

Equations (2.1)-(2.8) describe the effect the mean magnetic field has on ions. To derive the line profile for ion species, one could, in principle, apply this set of equations to each and every neutral flow present in a region of a given molecular cloud and project the resulting ion velocities along the line of sight. The sum of all these contributions would give us the observed line profile.

Even though we don't have such a detailed knowledge of the dynamics of molecular clouds, we can still apply this procedure to the study of simple cases. More precisely, we will concentrate on a given position in a cloud where all the neutral flows are such that they have i) azimuthal symmetry about the axis defined by the direction of the mean magnetic field and ii) reflection symmetry across the plane perpendicular to the same axis. For example, a bipolar outflow would fit this geometry. With these restrictions, we get for the observed ion line profiles:

$$\langle v_{obs} \rangle = 0 \tag{2.9}$$

$$\sigma_{obs}^2 = \sum_k C^k \left[\left\langle \left| \mathbf{v}_{\parallel}^k \right|^2 \right\rangle \cos^2(\alpha) + \frac{1}{2} \left\langle \left| \mathbf{v}_{\perp}^k \right|^2 \right\rangle \sin^2(\alpha) \right] \tag{2.10}$$

where α is the angle between the direction of the mean magnetic field and the line of sight. The summation runs over every flow contained in any given quadrant of any plane which is perpendicular to the plane of reflection symmetry and which also contains the axis of symmetry. C^k is the weight associated with the flow k, which presumably scales with the ion density (if the line is optically thin). An equivalent set of equations applies equally well to any coexistent neutral species (which we assume to exist in proportions similar to that of the ion), provided we replace v_{obs} by v_{obs}^n, σ_{obs} by σ_{obs}^n and $\mathbf{v}^k$ by $[\mathbf{v}^n]^k$. Using (2.1)-(2.8), one can easily verify that these two sets of equations (for neutrals and ions) are identical when

the mean magnetic field is negligible ($\langle\omega_g\rangle \ll \langle\omega_r\rangle$).

Under the assumptions that there is no intrinsic dispersion in the neutral flows and that the mean magnetic field is strong ($\langle\omega_g\rangle \gg \langle\omega_r\rangle$), we get for the neutral and ion line widths:

$$[\sigma^n_{obs}]^2 = \sum_k C^k \left\langle [\mathbf{v}^n]^k \right\rangle^2 \left[\left\langle \cos\left(\theta^k\right)\right\rangle^2 \cos^2(\alpha) + \frac{1}{2}\left\langle \sin\left(\theta^k\right)\right\rangle^2 \sin^2(\alpha)\right] \tag{2.11}$$

$$\sigma^2_{obs} \simeq \sum_k C^k \left\langle [\mathbf{v}^n]^k \right\rangle^2 \left[\left\langle \cos\left(\theta^k\right)\right\rangle^2 \cos^2(\alpha) + \frac{\left\langle \sin\left(\theta^k\right)\right\rangle^2}{\left[\frac{m}{\mu} - 1\right]} \left[a\cos^2(\alpha) + \frac{g}{2}\sin^2(\alpha)\right]\right] \tag{2.12}$$

where θ^k is the angle between flow k and the axis of symmetry. From equations (2.11)-(2.12) one can see that if the flows are aligned with the mean magnetic field ($\theta^k \simeq 0$), then neutrals and ions will have similar line widths. On the other hand, when the flows are perpendicular to the field ($\theta^k \simeq \frac{\pi}{2}$) the ions have a much narrower profile which scales with their molecular mass as $\left[\frac{m}{\mu} - 1\right]^{-\frac{1}{2}}$.

We can further consider the average width one would expect for both kinds of molecular species when a sample of objects is considered. This can be achieved by averaging equations (2.11)-(2.12) over the angle α (assuming the sources in the sample to be more or less similar). Assuming that there is no privileged direction in space for the mean magnetic field, we get:

$$\left\langle [\sigma^n_{obs}]^2 \right\rangle = \frac{1}{3}\sum_k C^k \left\langle [\mathbf{v}^n]^k \right\rangle^2 \tag{2.13}$$

$$\left\langle \sigma^2_{obs} \right\rangle \simeq \frac{1}{3}\sum_k C^k \left\langle [\mathbf{v}^n]^k \right\rangle^2 \left[\left\langle \cos\left(\theta^k\right)\right\rangle^2 + \frac{\left\langle \sin\left(\theta^k\right)\right\rangle^2}{\left[\frac{m}{\mu} - 1\right]}\right] . \tag{2.14}$$

A variation of the angle α between the mean magnetic field and the line of sight can

have a significant effect on the width of the observed ion line profile from a given object (see equation (2.12)). But this is not necessarily true for neutral species, we can see from equation (2.11) that the line width is a lot less sensitive to variations in α than that of the ion. The same statements are true for the sample of similar sources (of different orientations) considered here. We can therefore expect the mean width of a neutral line to be larger than its variation between sources and make the following approximation:

$$\frac{\langle \sigma_{obs}^2 \rangle}{\langle [\sigma_{obs}^n]^2 \rangle} \simeq \left\langle \frac{\sigma_{obs}^2}{[\sigma_{obs}^n]^2} \right\rangle .$$

The term on the right hand side represents the average of the square of the ratio of the ion to neutral line widths. By computing this ratio, one can get an idea of the propensity shown by the flows and the mean magnetic field for alignment with each other.

Going back to equations (2.13)-(2.14), we once again see that if the flows are parallel to the field ($\theta^k \simeq 0$), the mean ratio of ion to neutral line widths is close to unity. When the flows are perpendicular ($\theta^k \simeq \frac{\pi}{2}$) to the field, the square of this ratio is proportional to $\left[\frac{m}{\mu} - 1\right]^{-1}$. On the other hand, if the flows don't have any preferred direction and are randomly oriented (with a uniform distribution) we then find:

$$\left\langle \frac{\sigma_{obs}^2}{[\sigma_{obs}^n]^2} \right\rangle \simeq \frac{1}{3}\left[1 + \frac{2}{\frac{m}{\mu} - 1}\right] \tag{2.15}$$

which equals 0.38 (0.37) for an ion of molecular mass $A_i = 30$ (45).

3. Observations of $H^{13}CN$, $H^{13}CO^+$ and HCS^+.

In this section we complement our previous observations of HCN, HCO^+ and N_2H^+ in OMC1, OMC2, OMC3 and DR21OH with observations of $H^{13}CN$, $H^{13}CO^+$ and HCS^+ on

a sample of ten objects. These observations are important in that they allow us to ensure that the effect reported in Paper I was not caused by excess saturation of the HCN line profiles. $H^{13}CN$, $H^{13}CO^+$ and HCS^+ are substantially less abundant than HCN and HCO^+, so their emission lines are more likely to be optically thin. Another fundamental reason for the importance of these further observations is that the effects of the magnetic field should be felt by all species of ions. It is therefore desirable to test our concept with observations from as many ion species as possible.

We present the spectra in Figures 9, 10 and 11. All observations were obtained with the 200-300 GHz and 300-400 GHz receivers at the CSO over a total of fifteen nights during the months of October, November and December 1999. The spectra were calibrated using scans made on planets available during this period (Mars, Jupiter and Saturn). Telescope efficiencies were calculated to be ≈ 70 % for the 200-300 GHz receiver (beam width of $\approx 32''$) and ≈ 60 % for the 300-400 GHz receiver (beam width of $\approx 20''$). The maps of NGC 2071 and NGC 2264 in HCN and HCO^+ ($J \rightarrow 4-3$) presented in Figure 12 were obtained with the 300-400 GHz receiver in April 1999.

As can be seen, all objects show the line profiles of the ion species as being narrower than those of the neutral species. This is most evident in OMC1, OMC2-FIR4 and W3 IRS5. A suppression of the high velocity wings is the most obvious feature in the case of DR21OH.

Upon closer inspection of the spectra obtained for OMC2-FIR4, we note that the neutral species exhibit profiles that can easily be separated into two components: one narrow line with a FWHM ≈ 1 km/s that we can associate with the quiescent part of the cloud and a broad feature with a FWHM ≈ 8 km/s which we assume to be related to (out)flows. On the other hand, the flow component is virtually non-existent in the ion spectra. From this, we can conclude that there is probably a significant misalignment between the direction of the flows and that of the mean magnetic field for this object.

In the case of DR21OH, it is worth noting the striking difference between this set of spectra and the one obtained for the main isotopes (see Figure 2 of Paper I). Indeed, a double peaked profile was the most obvious feature in the HCN and HCO^+ spectra. This was also observed in CN observations by Crutcher et al. (1999) which lead them to identify the peaks as representing two different velocity components and assign two different magnetic field values as measured with the Zeeman effect. But as pointed out before, these molecular species are certainly abundant enough that we should not be surprised if they exhibited strongly self-absorbed line profiles. This effect is well known and can lead to an underestimation of the kinetic temperature of molecular clouds as described, for instance, by Phillips et al. (1981). The fact that the less abundant isotopes do not exhibit the same double peaked profile suggests that this is what is at play in the case of DR21OH and that we are really dealing with a single velocity component.

We present in Table III a comparison of the line widths (more precisely their standard deviations σ_v) for the different species discussed in this paper, as well as for those studied in Paper I, for our sample of molecular clouds. The widths were measured after the lines were modeled with a multi-Gaussian profile. We have separated the data into four different groups within which the comparison between ion and neutral species should be made. The separations occur naturally and are based on two criteria: i) the perceived optical depth of the lines and ii) the telescope beam applicable to different sets of observations (for example, for $H^{13}CN$ (and $H^{13}CO^+$) in the $J \rightarrow 4-3$ transition, the beam size is $\approx 20''$ whereas it is $\approx 32''$ for the lower $J \rightarrow 3-2$ transition). We have also included two detections of H_3O^+ made on W3 IRS5 by Phillips et al. (1992), these are important since they allow us to test our theory on a different ion species which has a significantly lower molecular mass ($A_i = 19$).

We have, whenever possible, verified that the opacity of the lines of the $H^{13}CN$, $H^{13}CO^+$,

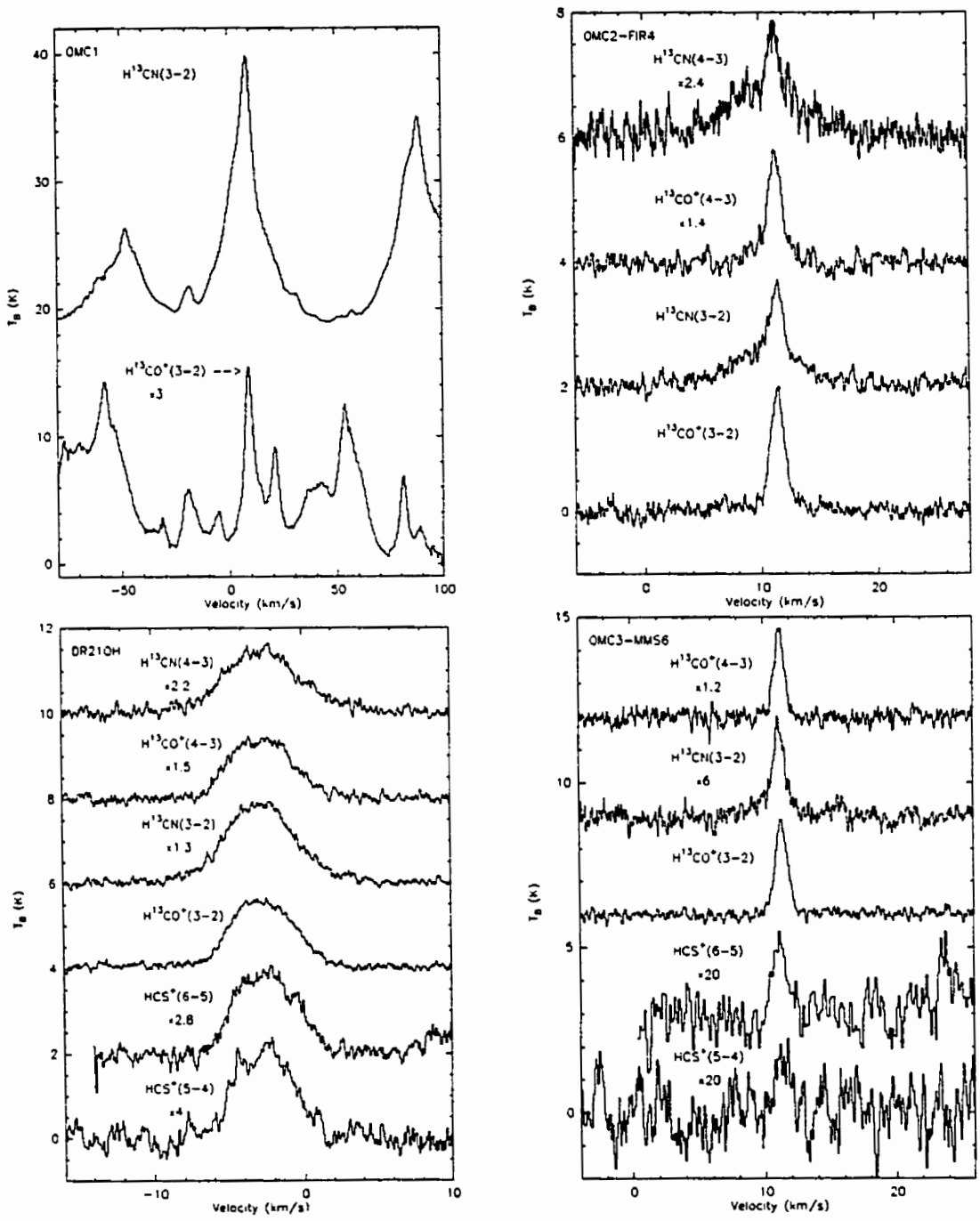

Fig. 9.— $H^{13}CN$, $H^{13}CO^+$ and HCS^+ (for DR21OH and OMC3-MMS6) observations at the center position of (clockwise starting from top left): OMC1, OMC2-FIR4, OMC3-MMS6 and DR21OH.

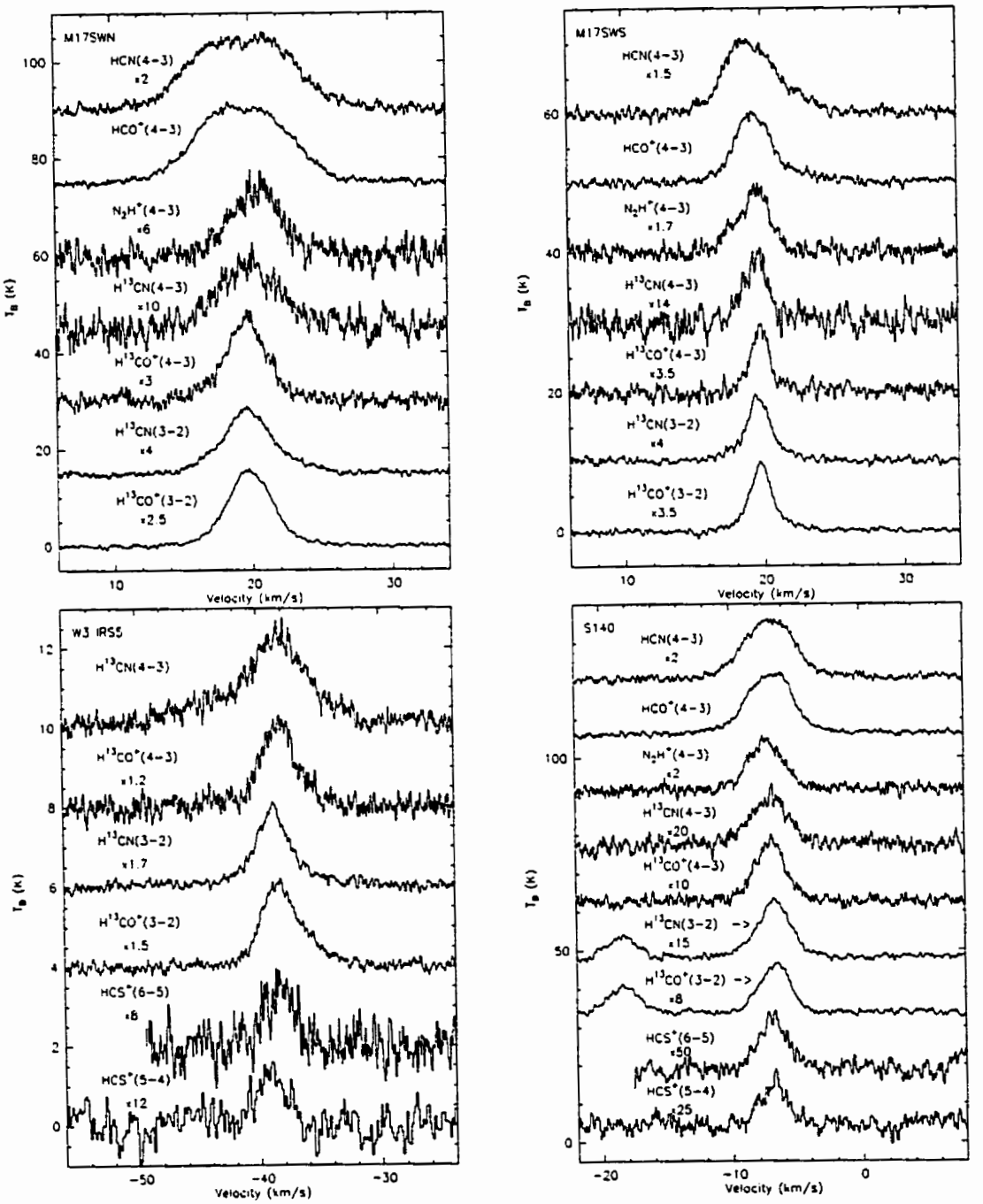

Fig. 10.— $H^{13}CN$, $H^{13}CO^+$ and HCS^+ (for S140 and W3 IRS5) observations at the center position of (clockwise starting from top left): M17SWN, M17SWS, S140 and W3 IRS5.

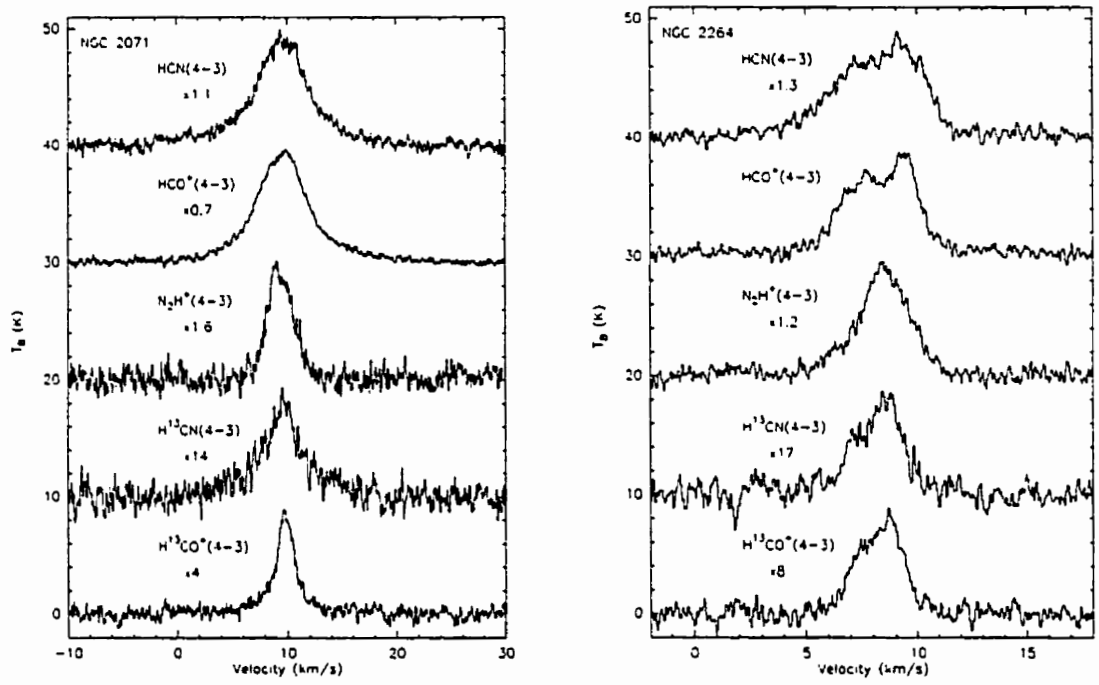

Fig. 11.— HCN, HCO^+, N_2H^+, $H^{13}CN$ and $H^{13}CO^+$ observations at the center position of NGC 2071 (left) and NGC 2264 (right).

HCS^+ and H_3O^+ species are indeed thin. This was accomplished using the ratio of the line temperature between two different transitions of a given species (assuming LTE and unity beam filling factors (Emerson 1996)). For example, in the case of the $H^{13}CO^+$ spectra for OMC2-FIR4 we have line temperatures of 1.9 K and and 1.3 K for the $J \rightarrow 3{-}2$ and $J \rightarrow 4{-}3$ transitions respectively. From their ratio and the assumptions made above, we calculated an excitation temperature of ≈ 11 K (assumed to be the same for both transitions) which then in turn allows us to obtain opacities of ≈ 0.17 and ≈ 0.12 for the $J \rightarrow 3-2$ and $J \rightarrow 4-3$ transitions respectively. It should be kept in mind that LTE may not be appropriate for these transitions/sources. Furthermore, the values thus obtained are quite sensitive to the beam filling factors which are probably different for lines observed with different beam sizes. However, we are not seeking a precise value for the opacities, but merely a reassurance that these lines are thin, which this technique provides.

In all cases, the lines were found to be optically thin with the ions generally more opaque than the neutrals, the highest opacity calculated was ≈ 0.3. One possible exception is the $H^{13}CN$ $J \rightarrow 3-2$ line for OMC1, where a comparison with the same transition of the main isotope gives an opacity of ≈ 0.6. At any rate, it appears that we can safely assume that differences in opacity between ion and neutral lines will not bring any ambiguity in studying the effects of the magnetic field (see section 1). We can therefore be confident that our widths comparisons are justified.

Upon examination of Table III, we note that in all cases the ion lines exhibit smaller widths (σ_v) than the comparable neutral lines. As was stated in Paper I, this difference in line width could also be partly due to other factors (sampling effect, chemical differentiation, ...). But to bring support to the hypothesis that HCN and HCO^+ are suitable candidate for our study, we discussed observational evidence from the extensive work of Ungerechts et al. (1997), more precisely the fact that their maps of the region surrounding OMC1 for

these two molecular species show similar spatial distributions. We, in turn, provided our own maps of OMC2-FIR4 for the same species which also show resemblance in the distributions as well as a good alignment of their respective peaks. We add to the evidence with Figure 12 where we again present HCN and HCO^+ maps in the $J \rightarrow 4-3$ transitions, but this time for NGC 2071 and NGC 2264. The same comments apply for those maps: although the ion spatial distributions are somewhat more extended, the two peaks are well aligned. And from Figure 11, we can also attest on the agreement of the systematic velocities for the two species.

If all is well with HCN and HCO^+, it appears reasonable to assume that the same is true for their less abundant isotopic counterparts $H^{13}CN$ and $H^{13}CO^+$. But we should point out that such comments are probably not true for N_2H^+ when compared to HCN. It is well known (Bachiller 1996, 1997) that N_2H^+ is only observed in the colder condensations of the gas whereas HCN often takes part in outflows, this would automatically result in the former exhibiting narrower line profiles. Our conclusions will, therefore, not be based on comparisons from the data obtained for these two species.

This being said, we interpret the fact that we consistently detect narrower ion line profiles over a sizable sample of molecular clouds for many different ion species as strong evidence in favor of our theory. The ratio of ion to neutral line widths ranges anywhere from ≈ 0.2 to ≈ 0.9 (see Table IV), which is not unexpected considering the analysis made in section 2.1. We then showed that ion line widths are strongly dependent on the alignment of the neutral flows with the mean magnetic field (see equation (2.12)) and are therefore liable to vary from one object to the next. The largest value for this ratio is $\simeq 0.93$ in the case of NGC 2071, implying a good alignment between the field and the flows. Interestingly, this object is known to exhibit strongly collimated jets (Girart et al. 1999, and references therein), this suggests the possibility that these are closely linked to the direction of the

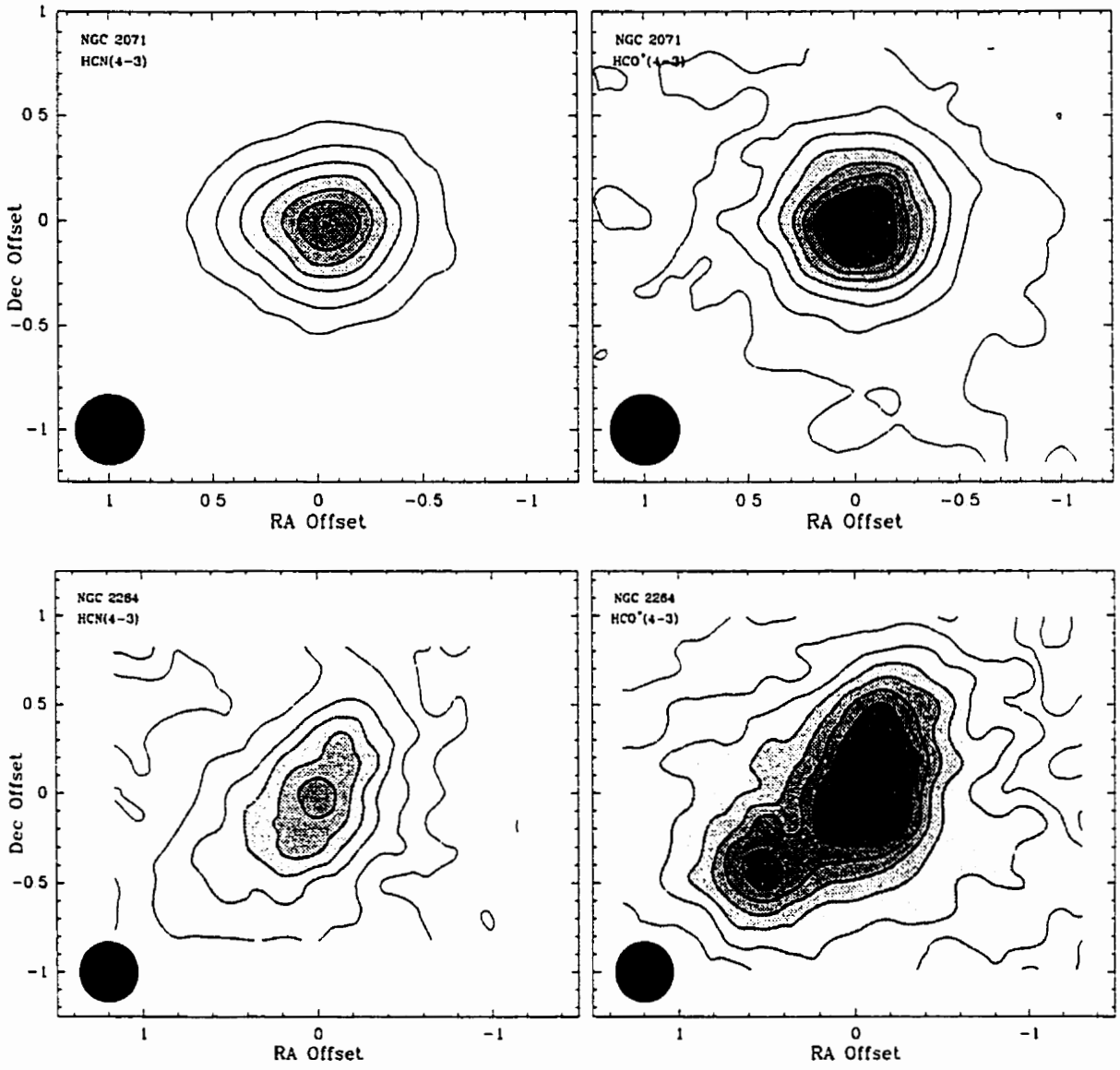

Fig. 12.— HCN and HCO^+ ($J \rightarrow 4-3$) maps of NGC 2071 (top) and NGC 2264 (bottom). Although the ion spatial distributions are somewhat more extended, the two peaks are well aligned and the HCN and HCO^+ systematic velocities agree (from Figure 11). The maps for NGC 2071 (NGC 2264) have the same lowest contour level of 5 K·km/s (2.5 K·km/s) and the following levels increase linearly with an interval of the same amount. The maps' grid spacing of 10″ is half of the beam width (shown in the lower left corners). The pointing accuracy is better than $\approx 5''$. Note that the spatial scale is not the same for the two sources.

mean magnetic field. This aspect will be studied in detail in a subsequent paper.

As a final comment in this section, we point out that the effect of the magnetic field on ion line profiles appears to be roughly similar in importance whether the lines observed are optically thick or thin. This can seen from Table IV where we show the ion to neutral line width ratios for our sample of objects.

Table III. Line widths in star forming regions.

	σ_v (km/s)[a]			σ_v (km/s)[b]			σ_v (km/s)[c]				σ_v (km/s)[d]			
	HCN	HCO^+	N_2H^+	HCN	HCO^+	N_2H^+	$H^{13}CN$	$H^{13}CO^+$	H_3O^+	H_3O^+	$H^{13}CN$	$H^{13}CO^+$	HCS^+	HCS^+
Source	4 – 3	4 – 3	4 – 3	3 – 2	3 – 2	3 – 2	4 – 3	4 – 3	$3_0^+ - 2_0^-$	$3_2^+ - 2_2^-$	3 – 2	3 – 2	6 – 5	5 – 4
W3 IRS5	6.88	2.96	...	...	...	...	5.25	1.51	2.38[f]	2.38[f]	4.25	1.99	1.21	1.20
L1551 IRS5	1.03	0.92	0.94	...	...	...	...	...	...	...	...	...	...	...
OMC3-MMS6	1.40	0.71	0.56	1.25	0.79	...	...	0.40	...	...	0.98	0.47	0.51[e]	0.55[e]
OMC1	...	...	...	17.42	3.23	1.87	...	...	...	...	8.55	1.85	...	...
OMC2-FIR4	3.59	2.72	1.34	...	...	...	3.33	1.05	...	...	3.02	0.65	...	...
NGC 2071	3.98	3.69	1.18	...	...	...	3.12	2.01	...	...	...	...	...	...
NGC 2264	1.88	1.60	1.38	...	...	...	1.04	0.92	...	...	...	...	...	...
M17SWN	3.29	2.96	1.82	...	...	...	2.82	1.91	...	...	2.19	2.03	...	...
M17SWS	2.04	1.84	1.32	...	...	...	0.89	0.69	...	...	1.51	1.19	...	...
DR21OH	5.75	4.61	2.08	...	...	2.41	2.95	1.93	...	...	2.82	2.04	1.86	1.72
S140	2.69	2.14	1.34	...	...	...	1.50	1.36	...	...	1.42	1.12	1.09	0.90

[a]Optically thick lines observed with a beam size of $\simeq 20''$.

[b]Optically thick lines observed with a beam size of $\simeq 32''$.

[c]Optically thin lines observed with a beam size of $\simeq 20''$.

[d]Optically thin lines observed with a beam size of $\simeq 32''$.

[e]The corresponding spectra have lower SNR with a line width uncertainty of $\simeq 0.1$ km/s.

[f]From Phillips et al. (1992). These spectra were obtained with a lower resolution spectrometer, their line width uncertainty is $\simeq 0.3$ km/s.

Table IV. Ion to neutral width ratios in star forming regions.

Source	Coordinates (1950) RA	DEC	v (km/s)	⟨ratio⟩ thick[a]	thin[b]
W3 IRS5	$2^h21^m53\overset{s}{.}3$	$61°52'21\overset{''}{.}4$	−38.1	0.43	0.39
L1551 IRS5	$4^h28^m40\overset{s}{.}2$	$18°01'41\overset{''}{.}0$	6.3	0.89	···
OMC1	$5^h32^m47\overset{s}{.}2$	$-05°24'25\overset{''}{.}3$	9.0	0.19	0.22
OMC3-MMS6	$5^h32^m55\overset{s}{.}6$	$-05°03'25\overset{''}{.}0$	11.3	0.51	0.48
OMC2-FIR4	$5^h32^m59\overset{s}{.}0$	$-05°11'54\overset{''}{.}0$	11.2	0.76	0.27
NGC 2071	$5^h44^m30\overset{s}{.}2$	$00°20'42\overset{''}{.}0$	9.5	0.93	0.64
NGC 2264	$6^h38^m25\overset{s}{.}6$	$09°32'19\overset{''}{.}0$	8.2	0.85	0.88
M17SWN	$18^h17^m29\overset{s}{.}8$	$-16°12'55\overset{''}{.}0$	19.6	0.90	0.81
M17SWS	$18^h17^m31\overset{s}{.}8$	$-16°15'05\overset{''}{.}0$	19.7	0.90	0.78
DR21OH	$20^h37^m13\overset{s}{.}0$	$42°12'00\overset{''}{.}0$	−2.6	0.80	0.69
S140	$22^h17^m40\overset{s}{.}0$	$63°03'30\overset{''}{.}0$	−7.0	0.80	0.85

[a]From the ratio of HCO^+ to HCN line width in table II.

[b]From the root mean square of ratios of $H^{13}CO^+$ to $H^{13}CN$ line width in table II.

3.1. Statistics of the ratios of line widths.

Following our discussion at the end of section 2.1, it is interesting to average the square of the ratio of the ion to neutral line widths over our sample and compare the results with equation (2.15). We find:

$$\left\langle \frac{\sigma^2_{H^{13}CO^+}}{\sigma^2_{H^{13}CN}} \right\rangle = 0.42 \tag{2.16}$$

$$\left\langle \frac{\sigma^2_{HCS^+}}{\sigma^2_{H^{13}CN}} \right\rangle = 0.32 \, , \tag{2.17}$$

which we interpret as meaning that, although this ratio can vary significantly from one object to the next, there is, on average, no obvious propensity for the alignment between the flows and the mean magnetic field in high density molecular clouds such as those studied here. For we know, from the aforementioned discussion, that if the neutral flows don't have any preferred orientation in relation to the magnetic field, these ratios would be 0.38 for $H^{13}CO^+$ and 0.37 for HCS^+. It should, however, be kept in mind that our sample of objects is not entirely composed of (more or less) similar objects, as was assumed when we derived equation (2.15).

4. Regions of low turbulence.

All the objects discussed so far present a fair amount of turbulence as can be attested by a comparison of the widths of the observed line profiles with their expected thermal width. The former being many times broader than the latter. In fact, as was mentioned earlier we would only expect to observe narrower ion lines in situations where this is the case. According to equations (2.1)-(2.8) and (2.12), we can identify three scenarios for which one should not expect any significant difference between the line widths of ion and neutral

species:

- the value of the mean magnetic field is such that $\langle \omega_g \rangle \ll \langle \omega_r \rangle$
- the mean magnetic field is aligned with the flow(s)
- the region under study has little or no (macro)turbulence.

In what follows, we will investigate some observational evidence that, we will argue, show cases where the last scenario is at work.

4.1. Dark clouds with dense cores.

Recently, Benson et al. (1998) studied, among other things, the correlation of the velocity and line widths between the spectra of N_2H^+ and other neutral species (C_3H_2, CCS and NH_3) on large samples of dark clouds (with dense cores). Their sample contains sources which are very different from those that we have been studying so far in that:

- they have much narrower line profiles, the mean line widths (FWHM) are 0.37 km/s for N_2H^+, 0.46 km/s for C_3H_2, 0.38 km/s for CCS and 0.36 km/s for NH_3
- most of the cores are primarily thermally supported, the corresponding thermal width of a neutral molecule of mean mass is 0.45 km/s at 10 K
- the densities probed with their observations are roughly two orders of magnitude lower, $n \gtrsim 10^4$ cm^{-3} in their case compared to $n \gtrsim 10^6$ cm^{-3} in ours.

Table V. Line widths in dense dark clouds.

Source	Coordinates (1950)		Δv (km/s)[a]		
	RA	DEC	N_2H^+	CCS	C_3H_2
Per 5	$3^h26^m45^s.5$	31°28′48″.0	0.37	0.27	0.43
B5	$3^h44^m28^s.7$	32°43′30″.0	0.43	0.41	0.48
L1498	$4^h07^m50^s.0$	25°02′13″.0	0.25	0.20	0.30
L1495	$4^h11^m02^s.7$	28°01′58″.0	0.25	0.25	0.32
L1527	$4^h36^m49^s.3$	25°57′16″.0	0.31	0.28	0.57
L1512	$5^h00^m54^s.4$	32°39′00″.0	0.19	0.18	0.26
L43E	$16^h31^m46^s.3$	−15°40′50″.0	0.27	0.69	0.45
L260	$16^h44^m22^s.3$	−09°30′02″.0	0.22	0.21	0.20
L234E	$16^h45^m22^s.6$	−10°51′43″.0	0.23	0.24	0.34
L63	$16^h47^m21^s.0$	−18°01′00″.0	0.24	0.36	0.27
L483	$18^h14^m50^s.5$	−04°40′49″.0	0.35	0.38	0.44
B133	$19^h03^m25^s.3$	−06°57′20″.0	0.62	0.46	0.39
B335	$19^h34^m33^s.3$	07°27′00″.0	0.32	0.26	0.45
L1251E	$22^h38^m10^s.8$	74°55′50″.0	0.93	1.03	0.85

[a]FWHM, from Benson et al. (1998).

As stated before, we expect that regions of low turbulence such as these dark cloud cores would not show significant differences between the width of the line profiles of ion and neutral species. The measured mean line widths reported by Benson et al. (1998) seem to indicate that this is the case, only the C_3H_2 species shows a mean line width noticeably different from that of the ion species. However, this situation improves when we limit the comparisons to only those objects which are common to each sample (i.e., the different sets of N_2H^+, CCS and C_3H_2 observations). This group of objects is listed in Table V along with the measured line widths. With this restriction, we find that the mean line widths are now 0.36 km/s for N_2H^+, 0.37 km/s for CCS and 0.41 km/s for C_3H_2. More to the point, if we calculate the root mean square value of the line widths ratios between the different species we get:

$$\sqrt{\left\langle \frac{\Delta v^2_{N_2H^+}}{\Delta v^2_{C_3H_2}} \right\rangle} = 0.90$$

$$\sqrt{\left\langle \frac{\Delta v^2_{N_2H^+}}{\Delta v^2_{CCS}} \right\rangle} = 1.05$$

$$\sqrt{\left\langle \frac{\Delta v^2_{CCS}}{\Delta v^2_{C_3H_2}} \right\rangle} = 0.97 .$$

It is therefore evident that the differences in mean line width between ion and neutral species are quite insignificant (compare with equations (2.16)-(2.17)). We should point out, however, that we have assumed that all the species are coexistent in the clouds. This is not necessarily true, the authors indeed discuss the lack of correlation between the column densities of N_2H^+ and those of the neutral species.

It is also worth mentioning that in a recent paper Crutcher (1999a) gives upper limits for the component of the magnetic field parallel to the line of sight for a few of the sources studied by Benson et al. (1998). These measurements were obtained using observations of

the Zeeman effect in OH emission lines at 1665 and 1667 MHz with a beam size of 18″ (Crutcher et al. 1993). The upper limits are all of the order of $\sim$ 10 μG, underlining the relative weakness of the magnetic field.

One might then argue that, according to equations (2.1)-(2.8), perhaps the field strength is too low to cause any narrowing in the line profiles of ions. But since we know that this manifestation should be apparent in the strong magnetic field limit ($\sim$ 0.01 μG at a density of $\sim$ 10^4 cm^{-3}, which is well below the typical value measured in the interstellar medium (Heiles 1987)), it is probably safe to assume that the low level of turbulence and other flows is the cause for the similarity between the ion and neutral spectral widths and not the weakness of the field.

5. Conclusion.

We have presented new observational evidence that helps to verify our assertions that the presence of a sufficiently strong magnetic field in a weakly ionized and turbulent plasma leads to ions exhibiting narrower line profiles and significantly suppressed high velocity wings when compared to neutral lines.

The effect was verified by comparing optically thin transitions of $H^{13}CN$, $H^{13}CO^+$ and HCS^+ made on a sample of ten high density molecular clouds. The results are in agreement with our previous observations (Paper I) of probably optically thick lines detected in OMC1, OMC2, OMC3 and DR21OH.

We also discussed the comparison of the line widths of N_2H^+, CCS, C_3H_2 and NH_3 made on samples of cold, thermally supported clouds previously published by Benson et al. (1998). We show that the lack of a significant difference between the widths of ion to neutral lines is exactly what would be expected for this type of object and therefore confirm a different

aspect of our concept presented in Paper I.

We thank Prof. G. A. Blake for directing us to the paper of Benson et al. (1998) and Prof. P. M. Solomon for his comments and suggestions. M. Houde's work was done in part with the assistance of grants from FCAR and the Département de Physique of the Université de Montréal. The Caltech Submillimeter Observatory is funded by the NSF through contract AST 9615025.

Chapitre 3

The alignment of the magnetic field and collimated outflows in star forming regions - the case of NGC 2071[1]

Abstract

The magnetic field is believed to play a crucial role in the process of star formation. From the support it provides during the initial collapse of molecular clouds to the creation of strong collimated jets responsible for large mass losses, current theories predict its importance in many different stages during the formation of stars. Here we report on observational evidence which tests one aspect that can be inferred from these theories: the predicted alignment between the local magnetic field and collimated bipolar outflows in such environments. The alignment is confirmed for the case of NGC 2071.

Subject headings: ISM: individual (NGC 2071) — ISM: cloud — ISM: magnetic field — ISM: molecules

---

[1]Houde, M., Phillips, T. G., Bastien, P., Peng, R., and Yoshida, H. 2000, submitted to ApJ

1. Introduction.

In two previous papers (Houde et al. 2000a,b), we presented theory and observations which established the possibility of detecting the presence of the magnetic field in molecular clouds through its effects on the profile of molecular ion emission lines. This new effect can be dramatic and can produce ion profiles with narrower line width and significantly suppressed high velocity wings when compared to the spectra of coexistent neutral molecular species. It is observed in the weakly ionized plasmas of the dense interstellar medium provided they are supported by turbulence or stellar outflows rather than thermally. It also requires some degree of misalignment between the local mean magnetic field and the neutral flows present in the gas. Differences between the line profiles of the ion and neutral species disappear if the flows and the magnetic field are aligned.

As can be inferred from the previous comments, the detection of a magnetic field is most easily established in cases where the differences between the lines profiles of ions and neutrals are strongly accentuated. However, under the assumption of the existence of a sufficiently large magnetic field, a high degree of similarity in the spectra can potentially tell us something about the alignment between the mean magnetic field and the flows. This is mostly interesting for the study of objects which show strong collimated bipolar outflows as it allows a comparison between theory and observation. Indeed, current theoretical models (see Bachiller (1996) for a review) predict the existence of bipolar jets emanating from the poles of the protostars during certain stages of star formation. One agent necessary for the presence of these jets is believed to be the magnetic field to which they are aligned. While these jets can be observed at optical and/or radio frequencies, molecular outflows, which appear to exist in irregular shells or in the walls surrounding the cavities formed by the jets, are also detected at millimeter and submillimeter wavelengths. The alignment between these molecular outflows and the magnetic field has been observed at optical wavelengths

with measurements of the orientation of the polarization vectors of the radiation emanating from background stars located behind bipolar outflows originating from protostars (Cohen et al. 1984; Heiles 1987). As far as we can tell, it has, however, never been confirmed with observations at millimeter or submillimeter wavelengths. The technique we present here, which we argue allows us to achieve this, has the advantage of being very simple. It only requires comparisons of the line profiles of coexisting neutral and ion molecular species, in our case HCN and HCO^+, taken at the same positions in the outflows.

To show how this can be done, we examine the following set of equations (Houde et al. 2000b) which applies to cases where the region under study has i) an azimuthal symmetry about the axis parallel to the orientation of the mean magnetic field and ii) a reflection symmetry across the plane perpendicular to this axis (see Figure 13). We also assume that the flows in the region under study are linear, the plasma is weakly ionized and all the collisions between ion and neutral molecules are perfectly elastic:

$$\left[\sigma^n_{obs}\right]^2 = \sum_k C^k \left\langle \left[\mathrm{v}^n\right]^k \right\rangle^2 \left[\left\langle \cos\left(\theta^k\right)\right\rangle^2 \cos^2(\alpha) + \frac{1}{2}\left\langle \sin\left(\theta^k\right)\right\rangle^2 \sin^2(\alpha)\right] \tag{3.1}$$

$$\left[\sigma^i_{obs}\right]^2 \simeq \sum_k C^k \left\langle \left[\mathrm{v}^n\right]^k \right\rangle^2 \left[\left\langle \cos\left(\theta^k\right)\right\rangle^2 \cos^2(\alpha) + \frac{\left\langle \sin\left(\theta^k\right)\right\rangle^2}{\left[\frac{m_i}{\mu} - 1\right]} \left[a\cos^2(\alpha) + \frac{g}{2}\sin^2(\alpha)\right]\right] . \tag{3.2}$$

The first equation gives an expression for the width (variance) of the neutral line profile and the second another expression for that of the ion. The summation runs over every flow present in any quadrant of any plane which is perpendicular to the plane of reflection symmetry and which also contains the axis of symmetry. C^k is the weight associated with the neutral flow k, which presumably scales with the particle density (we assume ions and

neutrals to exist in similar proportions), its velocity is given by $[\mathbf{v}^n]^k$, θ^k is the angle between its direction and that of the mean magnetic field and α is the angle between the latter and the line of sight to the observer. a and g are coefficients that are weak functions of the ion mass m_i and the reduced mass μ. If we choose the mean neutral molecular mass to be $2.3\,m_{\rm H}$, we get $a \simeq 0.16$ and $g = 1 - a$ for a wide range of ion masses. We can easily verify from equations (3.1) and (3.2) that, as was mentioned above, the ion and neutral species will have similar line widths if the magnetic field and the flows are aligned ($\theta^k \simeq 0$), irrespective of what the viewing angle α is. The difference between the line widths is maximized when the flows are perpendicular to the field ($\theta^k \simeq \frac{\pi}{2}$).

In general, the line narrowing and high velocity wing suppression effects are seen for many ion species (HCO^+, $H^{13}CO^+$, N_2H^+, HCS^+ and H_3O^+ have been studied so far) whether the observed lines are optically thin or not. Some notable examples are W3 IRS5, OMC1, OMC2-FIR4 and OMC3-MMS6. We also showed, in our previous study of a sample of eleven molecular clouds (Houde et al. 2000b), that the ratio of ion to neutral line width is likely to vary significantly from one source to another, with the ion species always exhibiting narrower line profiles. However, when averaged over the sample, it is fairly close to what would be expected if the flows were randomly oriented in relation to the direction of the mean magnetic field (as can be calculated from equations (3.1) and (3.2)). Perhaps this is a sign that there is no obvious propensity for the alignment between the two in the cores of such high density molecular clouds. But in at least one case of a well defined outflow, field and flow alignment is indicated.

In the next section, we present observations of the NGC 2071 molecular cloud where we argue that HCN and HCO^+ spectra provide conclusive evidence for the alignment between the magnetic field and the collimated outflows. This conclusion will be drawn from the remarkable similarities between the profiles observed in the outflows for these two molecular

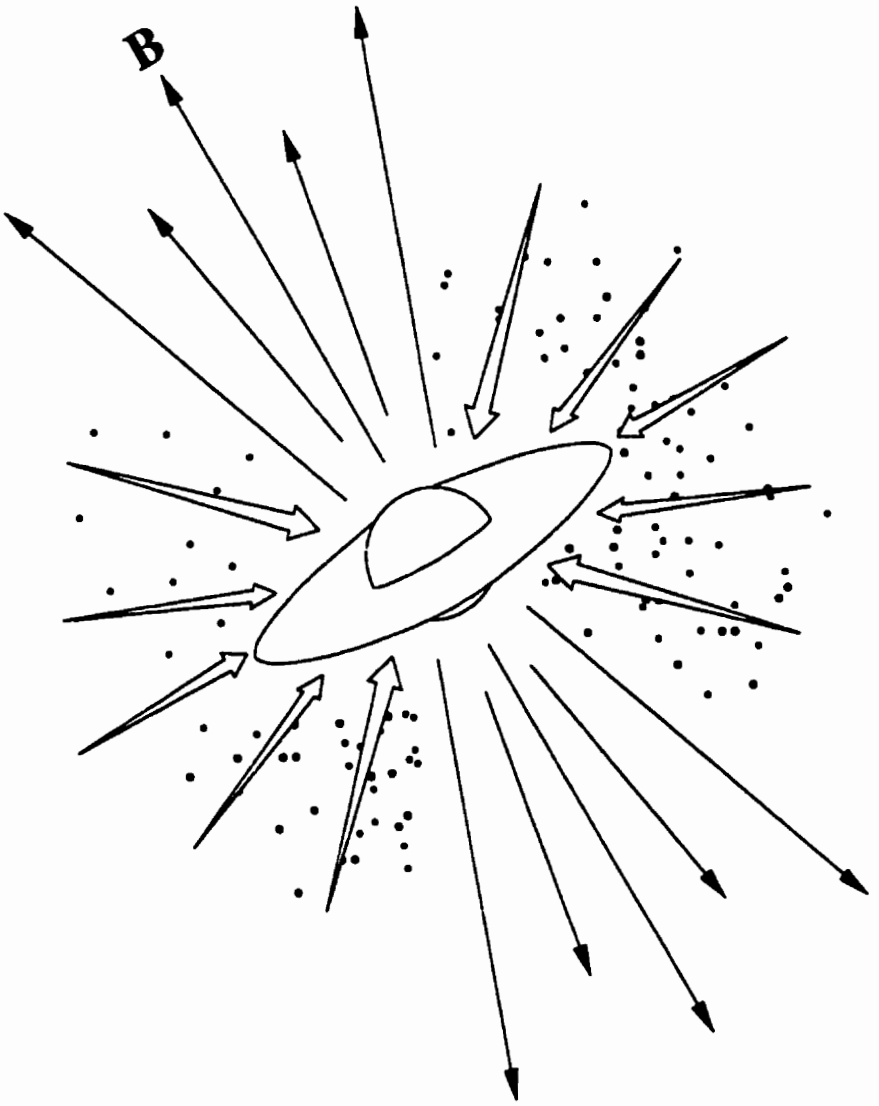

Fig. 13.— Example of a possible source geometry which exhibits the symmetries enumerated in the text.

species. In light of the above discussion concerning the significant difference in line widths which we observed in molecular clouds, we infer that, from a more general standpoint, this is rather unusual. An explanation for this might reside in the fact that the aforementioned narrowing of the ion lines could be an indication that the central structure of the clouds is more complex than the simple, bipolar outflow that will be dealt with here. A given core could harbor multiple flows and even, perhaps, a magnetic field which may be controlled from a system external to it. For example, one could conceive of the possible interactions between the fields and flows emanating from different protostellar sources residing in the core. Hopefully, possible future high-resolution (interferometric) observations will shed some light on this issue.

2. Observations.

NGC 2071 is an optical reflection nebula located at approximately 390 pc in the L1630 molecular cloud of the Orion B region. This object is known to exhibit strong molecular outflows which have been extensively studied with many different molecular species (Girart et al. 1999, and references therein). Some of the outflows' main characteristics are their relatively high degree of collimation, their large size and a favorable viewing angle which all contribute to a relatively well understood geometry, making this source a perfect candidate for the application of our technique.

Our observations of NGC 2071 were made at the Caltech Submillimeter Observatory (CSO) using the facility's 300-400 GHz receiver (beam width $\simeq 20''$). ^{12}CO ($J \rightarrow 3-2$) data was obtained on 29 January 1997 and 5 February 1999 while HCN ($J \rightarrow 4-3$) and HCO^+ ($J \rightarrow 4-3$) spectra were obtained on 29 October 1999 and 16 December 1999.

Figure 14 shows two ^{12}CO ($J \rightarrow 3-2$) maps, the contours highlight the integrated intensity of a) the red outflow (10 km/s $\leq v \leq$ 50 km/s) and b) the blue outflow (-50 km/s

$\leq v \leq$ 10 km/s). The underlying grey scale levels delineate the total integrated intensity (-50 km/s $\leq v \leq$ 50 km/s). As can be seen from these maps, the two outflows are very well defined and the overall appearance of the source seems, at least to some degree, to possess the symmetries enumerated earlier.

Figure 15a) shows three spectra (^{12}CO, HCN and HCO$^+$) taken at the source's center position. The HCN and HCO$^+$ spectra are very similar with their center velocity ($\approx$ 9.5 km/s) reasonably well aligned with the self-absorption feature of the ^{12}CO spectrum (presumably caused by and at the velocity of the ambient quiescent cloud). The HCO$^+$ to HCN line widths ratio was calculated to be 0.93 (Houde et al. 2000b). Although this position is not located in any of the two outflows, this number suggests that perhaps we have a good alignment between the mean magnetic field and the outflows. To verify this, we have obtained deep integration spectra in one position for each outflow.

Figure 15b) shows spectra of the same molecular species taken in the redshifted outflow (RA off. = $-40''$, DEC off. = $-60''$). The ^{12}CO spectrum shows an extended high velocity wing that goes as far as 40 km/s. The HCN and HCO$^+$ spectra are, of course, much weaker at this position than at the center but also exhibit redshifted velocity wings which indicate that they are taking part in the outflow motion. At first look, these two spectra show similar profiles, reinforcing the alignment hypothesis between the magnetic field and the collimated outflows. Note that the velocity at peak intensity ($\approx$ 10.5 km/s) differs somewhat from that of the quiescent part of the cloud ($\approx$ 9.5 km/s). Figure 15c) shows a similar set of spectra taken in the blueshifted outflow (RA off. = $40''$, DEC off. = $50''$). The ^{12}CO spectrum again exhibits a strong high velocity wing that extends to approximately -50 km/s. But this time, the HCN and HCO$^+$ line profiles are noticeably different. The HCN spectrum has a velocity wing that extends as far as that of ^{12}CO while also showing a narrow peak at the velocity of the ambient cloud. The HCO$^+$ profile also exhibits a strong component at the

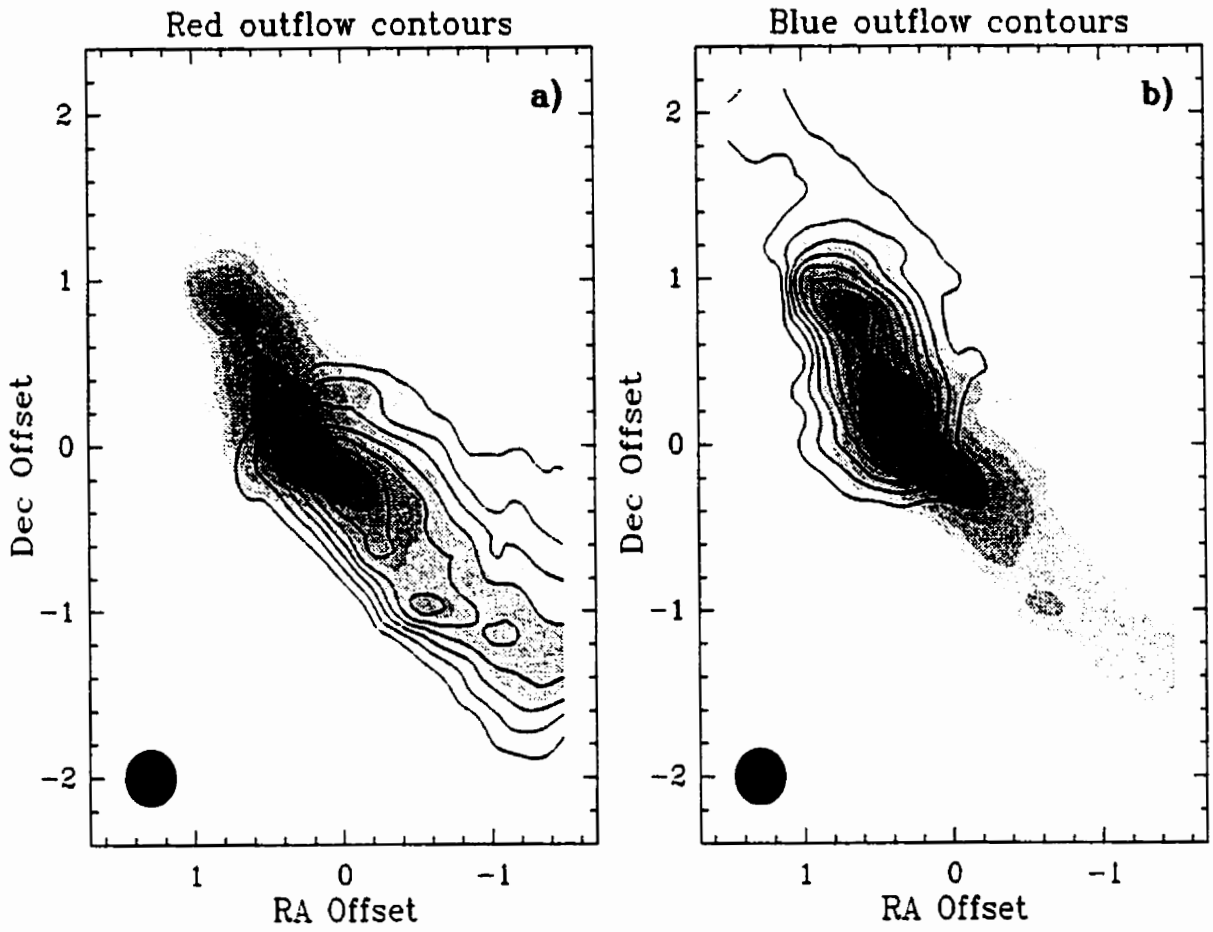

Fig. 14.— ^{12}CO ($J \rightarrow 3-2$) maps of NGC 2071. Map a) shows contours for the integrated intensity (10 km/s $\leq v \leq$ 50 km/s) of the red shifted lobe and map b) that of the blue shifted lobe (-50 km/s $\leq v \leq$ 10 km/s). The underlying grey levels delineate the total integrated intensity (-50 km/s $\leq v \leq$ 50 km/s). The two outflows are well defined and, to a good degree, possess the symmetries enumerated in the text. The maps have a grid spacing of 10″. The size of the telescope beam (FWHM$\simeq$ 20″) is shown in the lower left corners. The center position of the maps is RA = $5^h44^m30\overset{s}{.}2$, DEC = 00°20′42″.0 (J1950).

same velocity, but the high velocity wing is much weaker in proportion. This difference in appearance between the two spectra might lead us to abandon our assumption concerning the alignment of the magnetic field and the outflows. But a closer look at the last two spectra will convince us otherwise, as will be discussed in the next section.

In Figure 15d) we present a set of spectra taken at a position (RA off. = −60″, DEC off. = 40″) situated at approximately the same distance from the core as those of Figure 15b) and c) but in a direction roughly perpendicular to the axis joining the two outflows. At this position, both the HCN and HCO^+ show only one narrow component at the velocity of the ambient cloud, the ion profile being much stronger than the neutral. It is natural to assume that these lines are contributions from the quiescent part of the cloud. It then only requires a small step to conclude that the components located at the same velocity in the spectra of Figure 15b) and c) have a similar origin. That is, they are not part of the outflows and should be discarded in the comparison of the HCN and HCO^+ line profiles when studying spectra taken there.

3. Alignment of the magnetic field and the collimated outflows.

As we mentioned earlier, according to the material we presented in our two previous papers (Houde et al. 2000a,b), the line profiles of coexistent ion and neutral molecular species should show no significant differences in cases where there is a good alignment between the mean magnetic field and the flows present in a given region of a molecular cloud. In Figure 16, we have superposed the HCN and HCO^+ spectra obtained in the red and blueshifted outflows presented in Figure 15b) and c). We have also scaled the range of the vertical axis in order to better show the details of the different spectra and avoid any unwanted confusion that could be brought by the components of the quiescent part of the cloud. In both cases, the similarity between the HCN and HCO^+ spectra is striking. It is now obvious that the

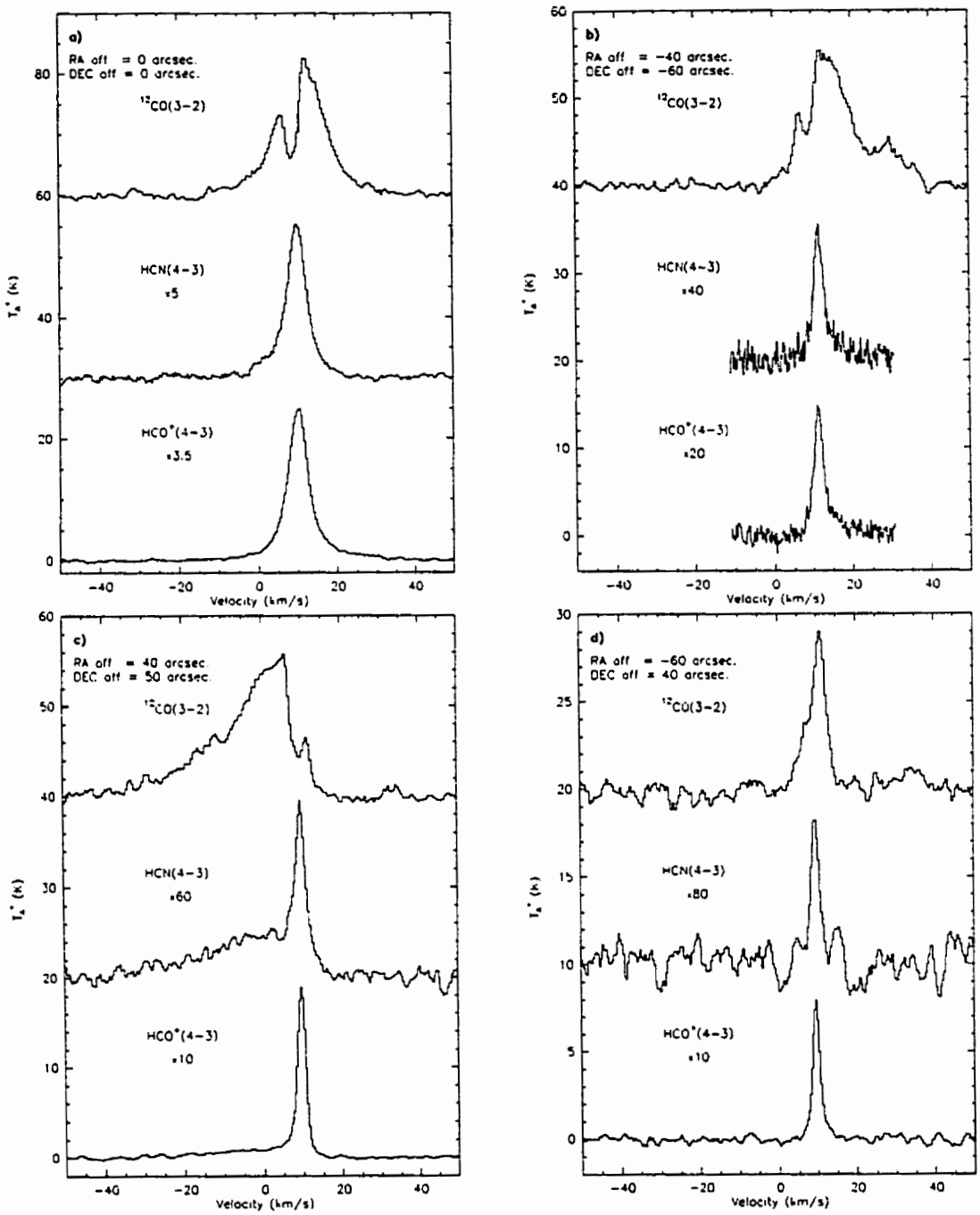

Fig. 15.— ^{12}CO ($J \rightarrow 3-2$), HCN ($J \rightarrow 4-3$) and HCO$^+$ ($J \rightarrow 4-3$) spectra in four different positions in the NGC 2071 molecular cloud. Emission line profiles a) at the center position (RA off. = 0″, DEC off. = 0″ in the maps shown in Figure 14), b) in the redshifted outflow (RA off. = −40″, DEC off. = −60″), c) in the blueshifted outflow (RA off. = 40″, DEC off. = 50″) and d) away from the three previous positions (RA off. = −60″, DEC off. = 40″).

high velocity wings have similar extent and even share many of the more subtle spectral features as can be seen in Figure 16b).

If we add to this the fact that comparison of optically thin lines ($H^{13}CN$ and $H^{13}CO^+$) which probe deeper in the source's center, presented in Houde et al. (2000b), give an ion to neutral line width ratio of 0.64 (establishing the presence of a magnetic field in the core), we are led to the conclusion that the magnetic field and the outflows must have a high degree of alignment with each other in the outflows of NGC 2071. For if it were not the case, the HCO^+ line profiles would be narrower and exhibit significant suppression of the high velocity wings when compared to those of HCN.

4. Magnetohydrodynamic waves and ion-neutral coupling.

The previous discussion and the conclusion we reached are partly based on the assumption, and likely hypothesis, that jets are the primary driving agent of molecular outflows. In this scenario, outflows with standard high velocities would consist of ambient cloud gas which has been swept up by underlying winds. Whether these winds are composed of the (ionized) jets alone or in combination with a significant neutral component is uncertain but there is evidence that entrainment of the ambient gas by bow shocks or turbulent mixing on the sides of the jets can be achieved (Bachiller 1996).

It is, however, pertinent to examine if magnetohydrodynamic (MHD) waves could in principle be at the origin of the molecular outflows if the jets were not the dominant driving force. It has been shown by Kulsrud & Pearce (1969, see their Appendix C) under which conditions will MHD waves propagate in a medium composed of both neutral and ionized parts. They actually defined two critical wavelengths which determine the allowed modes of propagation:

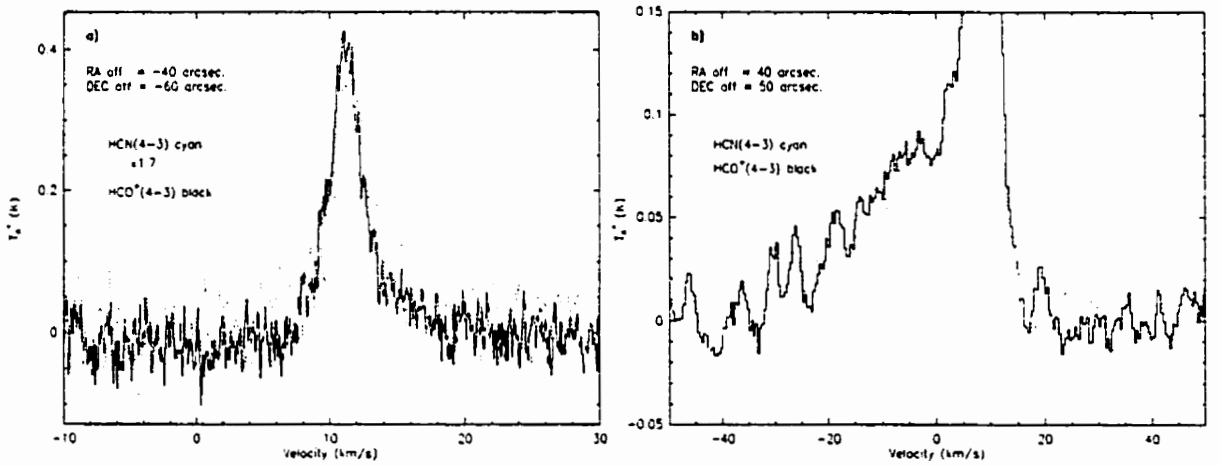

Fig. 16.— Superposition of the HCN ($J \rightarrow 4-3$) (cyan) and HCO^+ ($J \rightarrow 4-3$) (black) line profiles in the a) redshifted and b) blueshifted outflows. The profiles are remarkably similar for velocities different from that of the ambient cloud ($v \simeq 9.5$ km/s) allowing us to conclude that the mean magnetic field and the collimated outflows are aligned with each other. Note that the two figures have different velocity scales.

$$\lambda_1 = \frac{\pi v_A}{\nu_c} \cdot \sqrt{\frac{m_i n_n}{m_n n_i}}$$
$$\lambda_2 = \frac{4\pi v_A}{\nu_c} \cdot \frac{m_i}{m_n}$$

where v_A is the Alfvén speed of the ionized fluid alone without friction with the neutral part, m_i (m_n) and n_i (n_n) are respectively the mean mass and the density of the ions (neutrals) and ν_c is the collision rate of a given ion with the neutrals.

Cases where $\lambda > \lambda_1$ correspond to situations where the collisions between ions and neutrals are frequent enough that both components move together (the Alfvén speed is then reduced to $v_A \simeq B\,[4\pi m_n n_n]^{-\frac{1}{2}}$) whereas $\lambda < \lambda_2$ correspond to cases where collisions are infrequent and only the ions take part in the MHD wave motion. It can be shown that no waves can propagate at wavelengths $\lambda_2 < \lambda < \lambda_1$ (see Kulsrud & Pearce (1969) for more details).

Assuming a magnetic field strength $B \simeq 10\,\mu$G, a neutral density $n_n \simeq 10^5$ cm^{-3}, an ionization level of $\sim 10^{-8}$ and mean molecular masses of $29\,m_{\rm H}$ (ions) and $2.3\,m_{\rm H}$ (neutrals) we get $\lambda_1 \simeq 0.005$ pc and $\lambda_2 \simeq 7 \times 10^{-6}$ pc. From our observations of NGC 2071 presented in Figure 15, situations with $\lambda < \lambda_2$ can be ruled out since the ion and neutral species have similar profiles and, therefore, compatible motions. However, with the value obtained for λ_1 (almost an order of magnitude smaller than our beam size at the distance of NGC 2071), it is clear that some MHD waves could propagate. Under such circumstances, ions and neutrals will move together and will not show any differences in their line profiles irrespective of the orientation of the magnetic field in relation to the outflows. That is to say that it would then be impossible to draw any conclusion regarding the potential alignment of bipolar outflows and the local magnetic field.

We, however, consider this scenario to be unlikely in regard of our current knowledge and

understanding of the different mechanisms underlying the molecular outflow phenomena (as discussed at the beginning of the present section). In light of the evidence in favor of hydrodynamical processes (as opposed to magnetohydrodynamical) as driving agents of molecular outflows in star forming region, we believe that the alignment between the magnetic field and the outflows can be ascertained with the method presented in this paper.

5. Conclusion.

Using some of the material presented in our two previous papers (Houde et al. 2000a,b), we have shown how it is possible to find out if the mean magnetic field and collimated outflows are aligned with each other in star formation regions. We have applied this technique to data obtained at the CSO for the NGC 2071 molecular cloud and concluded that there is indeed a high degree of alignment in this case. This technique has the advantage of being very simple since it only requires a comparison of the width and high velocity wings between the line profiles of two coexistent molecular species (in our case HCN and HCO^+).

This also allows us to confirm one aspect of the current theoretical models which are striving to explain the different stages involved in the formation of stars.

M. Houde's work was done in part with the assistance of grants from FCAR and the Département de Physique of the Université de Montréal. The Caltech Submillimeter Observatory is funded by the NSF through contract AST 9615025.

Conclusion

Dans le travail qui a précédé, nous avons démontré l'existence d'un nouvel effet qui se manifeste lorsqu'il y a présence à la fois d'un champ magnétique local et de flots de matière (ou turbulence) dans l'environnement des nuages moléculaires. En effet, la présence du champ peut facilement être établie par une simple comparaison de la largeur des profils de raies de deux molécules coexistentes, une neutre et une autre ionique. Plus précisément, nous avons montré que cet effet se manifeste principalement de la façon suivante:

- les espèces moléculaires ioniques montreront des profils spectraux plus étroits et une suppression significative des "ailes" ou composantes de haute vélocité, comparativement aux spectres d'espèces neutres coexistantes, dans les cas où le champ magnétique moyen local est suffisamment puissant et s'il existe un manque d'alignement entre ce dernier et les flots de gaz présents dans la région concernée.

Étant donnée la faiblesse relative de l'intensité du champ requise ($\sim 10\,\mu$G pour un densité de l'ordre de 10^6 cm^{-3}), il ne serait donc pas surprenant que cette manifestation soit communément observée dans la majorité des nuages moléculaires. Mais notre étude va encore plus loin puisque nous avons detecté sa présence dans les spectres de tous les objets observés jusqu'à présent (onze).

Ce fait, nous croyons, apporte un support important en faveur de notre exposé. En effet, quoiqu'il soit possible d'évoquer l'existence d'autres phénomènes pour expliquer la différence entre les spectres ioniques et neutres, notre modèle est le seul qui est basé sur des principes physiques simples (comme la force de Lorentz) et qui prédit que les ions doivent,

dans ces circonstances, toujours exhiber des profils spectraux plus étroits. Par exemple, les gens impliqués dans cette étude, de même que la grande majorité des autres auxquels cette idée fut présentée, eurent la réaction première de tenter d'expliquer le phénomène par des arguments basés sur une différentiation chimique entre les espèces moléculaires concernées. Plus particulièrement, les hésitations rencontrées sont basées sur la supposition que des espèces chimiques différentes auraient des distributions spatiales différentes et par le fait même des distributions de vitesses tout aussi différentes. Cependant, le succès constant d'un modèle physique spécifique (comme celui présenté ici), à l'opposé d'un postulat chimique plutôt vague, ne peut être négligé. La nature du débat se transforme alors: pourquoi invoquer la supposition d'une différentiation chimique pour expliquer l'étroitesse relative des raies ioniques, quand un simple modèle physique spécifique la prédit? Pourquoi les raies ioniques sont-elles toujours plus étroites et non pas souvent plus larges? Pourquoi sont-elles toujours plus étroites quand la distribution spatiale des ions est similaire à celle de l'espèce neutre (comme pour OMC1, OMC2-FIR4, NGC 2071 et NGC 2264 avec HCO^+ et HCN)?

Tout aussi important est le fait que l'effet fut détecté pour chacune des espèces ioniques observées (HCO^+, $H^{13}CO^+$, N_2H^+, HCS^+ et H_3O^+) peut importe que la raie soit opaque ou transparente. Ceci exclut la possibilité que les évidences expérimentales initiales (obtenues avec HCN et HCO^+) soient artificielles et explicables par une plus grande opacité de la raie neutre. Il sera intéressant d'obtenir un plus grand nombre de détections avec des molécules de masses différentes. La mise en opération future d'un observatoire radioastronomique spatial tel que FIRST (Far InfraRed and Submillimeter Telescope) nous donnera, en ce sens, une occasion exceptionnelle pour la détection d'espèces de faible masse (telle que CH^+) qui sont autrement difficiles ou même impossible à observer avec des observatoires terrestres. Ces molécules ont généralement un spectre de rotation qui se situe dans un domaine de fréquences trop élevé pour ce faire.

Notre modèle fait aussi une prédiction applicable à un autre type de nuages moléculaires. Nous avons montré que nous sommes en droit de nous attendre à ce que les spectres ioniques et neutres seront similaires dans les cas où la région étudiée est micro-turbulente ou en équilibre thermique, et ce peu importe l'intensité du champ magnétique local. Ceci fut démontré expérimentalement lors de notre discussion du cas des sources observées par Benson et al. (1998) au chapitre 2.

Nous avons finalement appliqué la théorie développée pour vérifier l'alignement du champ magnétique et des flots bipolaires prédit par les différents modèles de formation stellaire. Nous avons vérifié ce fait pour NGC 2071. Bien sûr, il serait désirable que dans le futur une telle étude soit faite sur un groupe d'objets où l'alignement relatif des flots bipolaires et du champ est déjà connu (voir Cohen et al. (1984); Strom et al. (1987)). Il serait ainsi possible de comparer différentes méthodes d'observations et par le fait même, apporter un test additionnel en faveur de notre modèle.

Références

Akeson, R. L. 1997, Ph. D. Thesis, California Institute of Technology

Akeson, R. L., Carlstrom, J. E., Phillips, J. A., Woody, D. P. 1996, Ap. J., 456, L45

Bachiller, R. 1996, ARA&A, 34, 111

Bachiller, R. 1997, in Molecules in Astrophysics: Probes and Processes, ed. van Dishoeck, E. F. (Dordrecht: Kluwer), 103

Bastien, P. 1987, ApJ, 317, 231

Battaner, E. 1996, Astrophysical Fluid Dynamics (Cambridge)

Benson, P. J., Caselli, P., Myers, P. C. 1998, ApJ, 506, 743

Bloemhof, E. E. 1998, private communication

Chambers, W. G., Parker, T. J., Costley, A. E. 1986, Infrared and Millimeter Waves, 16, 77

Chambers, W. G., Costley, A. E., Parker, T. J. 1988, Int. J. of IR and MM Waves, vol. 9, No. 2, 157

Choudhuri, A. R. 1998, The Physics of Fluids and Plasmas, an Introduction for Astrophysicists (Cambridge)

Cohen, R. J., Rowland, P. R., and Blair, M. M. 1984, MNRAS, 210, 425

Collin, R. E. 1992, Foundations for Microwave Engineering (McGraw-Hill), 233-257

Crutcher, R. M. 1999a, ApJ, 520, 706

Crutcher, R. M. 1999b, in Interstellar Turbulence (Cambridge), 213

Crutcher, R. M., Troland, T. H., Lazareff, B., Paubert, G., Kazès, I. 1999, ApJ, 514, L121

Crutcher, R. M., Troland, T. H., Goodman, A. A., Heiles, C., Kazès, I., & Myers, P. C. 1993, ApJ, 407, 175

Davis, L. M. & Greenstein, J. L. 1952, ApJ, 114, 206

Dowell, C. D., Hildebrand, R. H., Schleuning, D. A., Vaillancourt, J. E., Dotson, J. L., Novak, G., Renbarger, T., and Houde, M. 1998, ApJ, 504, 588

Dowell, C. D., Hildebrand, R. H., Schleuning, D. A., Vaillancourt, J. E., Dotson, J. L., Davidson, J. A., and Houde, M. 2000, in preparation

Draine, B. T., & Weingartner, J. C. 1996, ApJ, 470, 551

Emerson, D. 1996, Interpreting Astronomical Spectra (Wiley)

Evans, N. J., II 1999, ARA&A, 37, 311

Falgarone, E. & Phillips. T. G. 1990, ApJ, 359, 344

Fowles, G. R. 1975, Introduction to Modern Optic (Dover), 164

Frisch, U. 1995, Turbulence (Cambridge)

Girart, J. M., Ho, P. T. P., Rudolph, A. L., Estalella, R., Wilner, D. J., and Chernin, L. M. 1999, ApJ, 522, 921

Goldreich, P., & Kylafis, N. D. 1981, ApJ, 243, L75

Goldreich, P., & Kylafis, N. D. 1982, ApJ, 253, 606

Gradshteyn, I. S., Ryzhik, I. M. 1980, Table of Integrals, Series and Products (Academic Press)

Greaves, J. S., Holland, W. S., and Friberg, P., and Dent, W. R. F. 1999, ApJ, 512, L139

Groves, W. E. 1953, J. Appl. Phys., 24, 845

Hartmann, L. 1998, Accretion Process in Star Formation (Cambridge), 154

Heiles, C. 1987, in Interstellar Processes, eds. Hollenbach, D. H., Thronson Jr, H. A. (Reidel), 171

Hildebrand, R. H. 1983, QJRAS, 24, 267

Hildebrand, R. H. 1988, QJRAS, 29, 327

Hildebrand, R. H., Dotson, J. L., Dowell, C. D., Schleuning, D. A., & Vaillancourt, J. E. 1999, ApJ, 516, 834

Hogerheijde, M. R., van Dishoeck, E. F., Blake, G. A. & van Langevelde, H. J. 1997, ApJ, 489, 293

Houde, M., Bastien, P., Peng, R., Phillips, T. G., and Yoshida, H. 2000a, ApJ, 536 (Paper I)

Houde, M., Peng, R., Phillips, T. G., Bastien, P. and Yoshida, H. 2000b, ApJ, 537 (Paper II)

Kuiper, T. B. H., Langer, W. D., and Velusamy, T. 1996, ApJ, 468, 761

Kulsrud, R., & Pearce, W. P. 1969, ApJ, 156, 445

Jackson, J. D. 1962, Classical Electrodynamics (Wiley)

Jeans, J. 1928, Astronomy and Cosmogony (Cambridge), republié 1961 (Dover)

Lamb, J. W. 1997, Modeling of Circular Polarizer Response, OVRO internal memo

Lamers, H. J. G. L. M., Cassinelli, J. P. 1999, Introduction to Stellar Winds (Cambridge)

Larsen, T. 1962, IRE Transactions on Microwave Theory and Techniques, 191

Lis, D. C., Serabyn, E., Keene, J., Dowell, C. D., Benford, D. J., Phillips, T. G., Hunter, T. R., Wang, N. 1998, ApJ, 509, 299

Longair, M. S. High Energy Astrophysics, vol. 2. 1994 (Cambridge), 219-221

Marion, J. B., Heald, M. A. 1980, Classical Electromagnetic Radiation (Harcourt Brace Jovanovich), 296

Mezger, P. G., Zylka, R., Wink, J. E., A&A, 228, 95

Mouschovias, T. Ch. 1991a, in The physics of star formation, eds. C. J. Lada, N. D. Kylafis (Dordrecht: Kluwer), 61

Mouschovias, T. Ch. 1991b, in The Physics of Star Formation, eds. C. J. Lada, N. D. Kylafis (Dordrecht: Kluwer), 449

Phillips, T. G., Knapp, G. R., Huggins, P. J., Werner, M. W., Wannier, P. G., and Neugebauer, G., and Ennis, D. 1981, ApJ, 245, 512

Phillips, T. G., van Dishoeck, E. F., and Keene, J. B. 1992, ApJ, 399, 533

Rybicki, G. B., Lightman. A. P. 1979, Radiative Processes in Astrophysics (Wiley-Interscience), 62

Schilke, P. 1999, private communication

Schleuning, D. A., Dowell, C. D., Hildebrand, R. H., Platt, S. R., Novak, G. 1997, PASP, 109, 307

Scoville, N. Z. & Sanders, D. B. 1987, in Interstellar Processes, eds. Hollenbach, D. H., Thronson Jr, H. A. (Reidel), 21

Serkowski, K. 1973, in IAU Symp. no. 52, Interstellar Dust and Related Topics, eds. Greenberg, J. M., van de Hulst, H. C. (Reidel), p. 145

Shapiro, J. B., Bloemhof , E. E. 1990, Int. J. of IR and MM Waves, vol. 11, No. 8, 973-980

Spitzer, L. Jr 1978, Physical Processes in the Interstellaire Medium (Wiley-Interscience)

Strom, S., Strom, K., and Edwards, S. 1987, in Galactic and Extragalactic Star Formation, eds. R. Pudritz, M. Fich, p.53

Shu, F. H. 1992, The Physics of Astrophysics, volume II: Gas Dynamics (University Science Books), 364.

Shu, F. H., Adams, F. C., & Lizano, S. 1987 ARA&A, 25 ,23

Shu, F., Najita, J., Galli, D., Ostriker, E. 1993, in Protostars and Planets III, 3

Tang, J. and Saito, S. 1995, ApJ, 451, L93

Tennekes, H & Lumley, J.L. 1972, A First Course in Turbulence (MIT Press)

Thronson, H. A., Jr, Harper, D. A., Keene, J., Moseley, H. Telesco, C. M. 1978, ApJ, 83, 492

Tinkham, M. 1964, Group Theory and Quantum Mechanics, (McGraw-Hill)

Ungerechts, H., Bergin, E. A., Goldsmith, P. F., Irvine, W. M., Schloerb, F. P., & Snell, R. L. 1997, ApJ, 482, 245

van de Hulst, H. C. 1957, Light Scattering by Small Particles (Dover), 119-121, 297-301

Wait, J. R. 1954, Can. J. Phys., 32, 571

Wait, J. R. 1955, Appl. Sci. Research, vol. 4, sect. B, 393

Wait, J. R. 1955, Can. J. Phys., 33, 189

Whittet, D. C. B. 1992, Dust in the Galactic Environment (Institute of Physics Publishing), 83, 165, 240

Wilson, Jr., E. B., Decius, J. C., Cross, P. C. 1955, Molecular Vibrations (Dover)

Wynn-Williams, G. 1992, The Fullness of Space (Cambridge)

Young, K. H. 1997, private communication

Zuckerman, B., Evans, N. J. II 1974, ApJ, 192, L149

Appendice: Polarizing grids, their assemblies and beams of radiation.[1]

Abstract

This paper gives an analysis of the behavior of polarizing grids and reflecting polarizers by solving Maxwell's equations, for arbitrary angles of incidence and grid rotation, for cases where the excitation is provided by an incident plane wave or a beam of radiation. The scattering and impedance matrix representations are derived and used to solve more complicated configurations of grid assemblies. The results are also compared with data obtained in the calibration of reflecting polarizers at the Owens Valley Radio Observatory (OVRO). From these analysis, we propose a method for choosing the optimum grid parameters (wire radius and spacing). We also provide a study of the effects of two types of errors (in wire separation and radius size) that can be introduced in the fabrication of a grid.

1. Introduction

The literature on wire grids is abundant and they have been studied with different techniques and for numerous applications. Most of the analysis were however restricted to special cases of incident field and grid orientations. The more general and arbitrary situation seems to have been first studied by Wait (1955a) (see also Larsen (1962)). This problem is

---

[1]Houde, M., Carlstrom, J. E., Schleuning, D. A., Akeson, R. L., Lay, O. P. 2000, to be submitted to Appl. Opt.

addressed again in this paper and follows a line of analysis fairly similar to the one used by Wait. Our treatment is however more general in that we don't assume that the wires of the grid are induced with only a longitudinal current; we will indeed show that an azimuthal component is also present. We also solve for the induced current by considering the tangential components of both the electric and magnetic fields at the surface of the wires, this brings about a correction in the expression for the current.

This analysis is carried in the next two sections and will serve as our basis for the treatment of the reflecting polarizer (section 4) and the introduction of the scattering and impedance matrix representations for a grid (section 3.3) which will in turn enable us to briefly discuss more complicated systems. These matrices will be particularly useful in allowing us to define what will be called the principal axes of a grid. These are two orthogonal and independent directions of polarization in the plane of the incident radiation along which an arbitrary electric field can be decomposed and shown to scatter without cross-polarization. With this representation at hand, it will then be possible to derive a set of optimal parameters (wire radius and spacing) to be used in the selection of a grid. We will also present an analysis of the effects of random errors that can be introduced in the fabrication of grids, the results obtained will then be compared to experimental results previously published by Shapiro & Bloemhof (1990).

The last section will be dedicated to the study of the more subtle impacts that the nature of the incoming radiation can have on the response of a grid assembly such as that of a reflecting polarizer (section 4). Although limited to this particular case, our discussion could possibly apply to other types instruments. We have also included at the end (Appendix II) a list of the symbols used in the different equations.

2. The case of a single wire.

Before trying to solve the problem of the grid or the reflecting polarizer, it is preferable to study the case of a single conducting wire. It will serve as the basis for our studies of the more complicated cases to follow in subsequent sections.

Let's suppose that a wire of radius a is oriented, as depicted in Figure 17, parallel to the x-axis at $y = y_o$, $z = z_o$ and that it is subjected to an incident plane wave $\mathbf{E}_i(\mathbf{r})$ of arbitrary direction and polarization:

$$\mathbf{E}_i(\mathbf{r}) = E_o(\alpha'\mathbf{e}_x + \beta'\mathbf{e}_y + \gamma'\mathbf{e}_z)\exp(-j(\mathbf{k}\cdot\mathbf{r} - \omega t)) \tag{A.3}$$

with

$$\mathbf{k} = k(\alpha\mathbf{e}_x + \beta\mathbf{e}_y + \gamma\mathbf{e}_z)$$

and where of course the following conditions of normalization and orthogonality apply: $\alpha^2 + \beta^2 + \gamma^2 = \alpha'^2 + \beta'^2 + \gamma'^2 = 1$ and $\alpha\alpha' + \beta\beta' + \gamma\gamma' = 0$. Using the coordinate system depicted in Figure 17 we have $\alpha = \sin(\chi_i)\sin(\varphi_g)$, $\beta = \sin(\chi_i)\cos(\varphi_g)$ and $\gamma = \cos(\chi_i)$ where χ_i is the angle of incidence and φ_g the angle of grid rotation.

In everything that follows we will drop the $\exp(j\omega t)$ term and assume it to be implicit in the equations. We will also suppose that the wire is of infinite length and made of a good conducting material of conductivity σ such that any current flowing through it can be accurately represented by a surface current vector $\mathbf{K}$. This quantity is related to the current density $\mathbf{J}(\mathbf{r})$ as follows:

$$\mathbf{J}(\mathbf{r}) = \mathbf{K}\,\delta(\rho - a)\,\exp(-j\mathbf{k}\cdot\mathbf{r}) \tag{A.4}$$

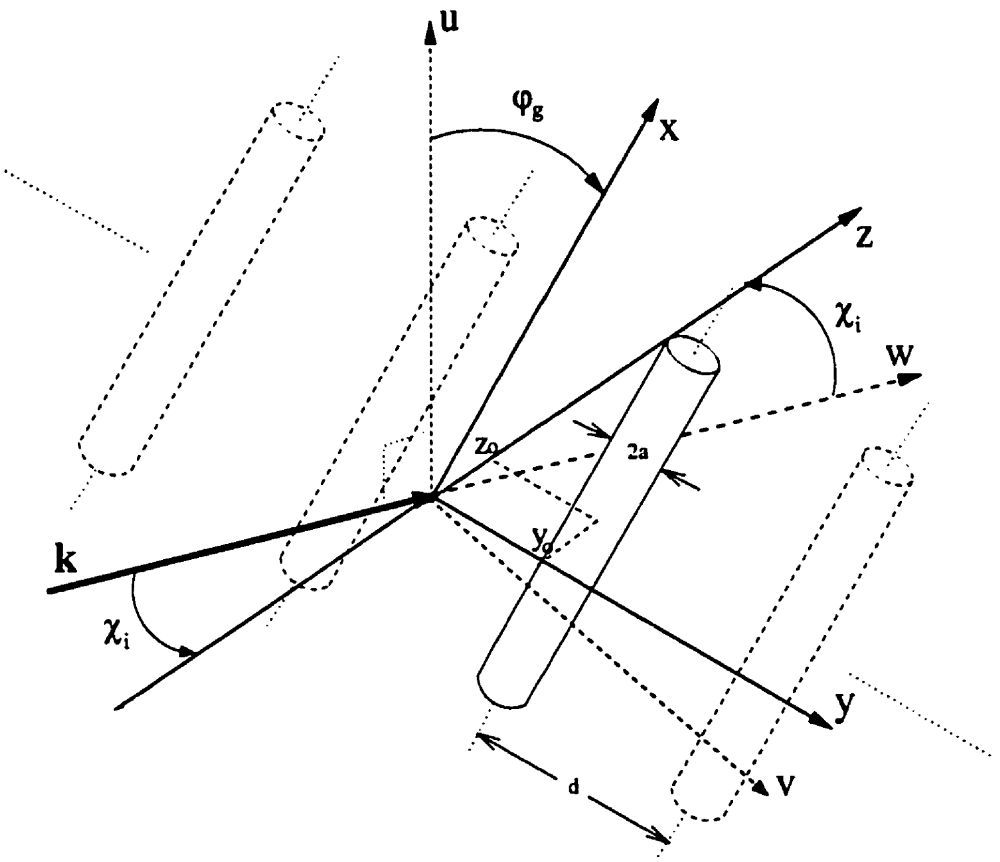

Fig. 17.— Coordinate systems for the study of a polarizing grid or a single wire. The wave vector **k** of the incident radiation is aligned with the w-axis, the u, x and y-axes are in the plane of the page, the w and z-axes are in the plane perpendicular to the u-axis and the wires are parallel to the xy-plane. We refer to the (u, v, w) and (x, y, z) systems as the laboratory and grid coordinates respectively.

where

$$\mathbf{K} = K^x \mathbf{e}_x + K^\theta \mathbf{e}_\theta$$

and $y - y_o = \rho\cos(\theta)$, $z - z_o = \rho\sin(\theta)$.

We will now solve for the scattered fields using the vector potential in the Lorentz gauge (Groves 1953):

$$\mathbf{A}_s(\mathbf{r}) = \frac{\mu_o}{4\pi}\int \mathbf{J}(\mathbf{r}')\frac{\exp(-jkR)}{R}d^3r' \tag{A.5}$$

$$\mathbf{E}_s(\mathbf{r}) = \frac{c^2}{j\omega}\nabla(\nabla\cdot\mathbf{A}_s(\mathbf{r})) - j\omega\mathbf{A}_s(\mathbf{r}) \tag{A.6}$$

$$\mathbf{H}_s(\mathbf{r}) = \frac{1}{\mu_o}\nabla\times\mathbf{A}_s(\mathbf{r}) \tag{A.7}$$

with

$$R^2 = (x-x')^2 + (y-y')^2 + (z-z')^2\,.$$

Equation (A.5) can be solved to give:

$$\begin{aligned}\mathbf{A}_s(\mathbf{r}) = \frac{\pi\mu_o a}{2j}\exp(-j\varphi)\sum_{n=-\infty}^{\infty}\mathbf{K}_n\exp(-jn\delta)\Big[&J_n(k'a)J_0(k'a)H_0^{(2)}(k'\rho)\\ &+\sum_{m=1}^{\infty}J_m(k'a)H_m^{(2)}(k'\rho)\left[J_{n+m}(k'a)\exp(-jm(\theta+\delta))\right.\\ &\left.+J_{n-m}(k'a)\exp\left(jm\left(\theta+\delta\right)\right)\right]\Big]\end{aligned} \tag{A.8}$$

with $\delta = \arctan\left(\frac{\beta}{\gamma}\right)$, $k' = k\sqrt{1-\alpha^2}$, $\varphi = k(\alpha x + \beta y_o + \gamma z_o)$ and where we have expanded the surface current vector in a Fourier series:

$$\mathbf{K} = \sum_{n=-\infty}^{\infty}\mathbf{K}_n\exp(jn\theta)$$

and $H_n^{(2)}(x)$, $J_n(x)$ are respectively Hankel's function of the second kind and Bessel's function, both of order n.

Equation (A.8) could in principle be used to solve for arbitrary order of accuracy, but if we assume that the wavelength of the incident wave and the size of the wire are such that $k'a \ll 1$, we can then approximate $\mathbf{A}_s(\mathbf{r})$ to:

$$\mathbf{A}_s(\mathbf{r}) = \frac{\pi\mu_o a}{2j}\mathbf{K}\, H_0^{(2)}(k'\rho)\exp(-j\varphi) \tag{A.9}$$

where we have replaced $\mathbf{K}_0$ by $\mathbf{K}$ for simplicity.

It is now straightforward, using equations (A.6) and (A.7) to calculate the scattered fields:

$$E_s^\rho(\mathbf{r}) = -j\alpha\sqrt{1-\alpha^2}F\,K^x H_1^{(2)}(k'\rho)\exp(-j\varphi) \tag{A.10}$$

$$E_s^\theta(\mathbf{r}) = -F\,K^\theta H_0^{(2)}(k'\rho)\exp(-j\varphi) \tag{A.11}$$

$$E_s^x(\mathbf{r}) = -\left(1-\alpha^2\right)F\,K^x H_0^{(2)}(k'\rho)\exp(-j\varphi) \tag{A.12}$$

$$H_s^\rho(\mathbf{r}) = \frac{\alpha}{Z_o}F\,K^\theta H_0^{(2)}(k'\rho)\exp(-j\varphi) \tag{A.13}$$

$$H_s^\theta(\mathbf{r}) = -j\frac{\sqrt{1-\alpha^2}}{Z_o}F\,K^x H_1^{(2)}(k'\rho)\exp(-j\varphi) \tag{A.14}$$

$$H_s^x(\mathbf{r}) = -j\frac{\sqrt{1-\alpha^2}}{Z_o}F\,K^\theta\left[\frac{H_0^{(2)}(k'\rho)}{k'\rho} - H_1^{(2)}(k'\rho)\right]\exp(-j\varphi) \tag{A.15}$$

where $F = \frac{\pi\mu_o\omega a}{2}$ and $Z_o = \sqrt{\frac{\mu_o}{\epsilon_o}}$ is the impedance of free space.

We now have to evaluate the surface current. In order to do so we must first express the incident plane wave in the appropriate coordinate system. This can be done by first using the following expression:

$$\exp(-jk(\beta y+\gamma z))=\sum_{n=-\infty}^{\infty}(-j)^n J_n(k'\rho)\exp(jn\theta') \tag{A.16}$$

with $\theta'=\theta-\arctan\left(\frac{\gamma}{\beta}\right)$ and then combine this equation with a well-known technique (van de Hulst 1957) where the incident field is split into two modes: one where the electrical field is parallel to the plane defined by $\mathbf{e}_x$ and $\mathbf{k}$ and another where the magnetic field is parallel to this same plane. This enables us to express the plane wave in cylindrical coordinates and match the fields with the usual boundary conditions for their tangential components at the surface of the wire:

$$E_i^x+E_s^x = Z_s(H_i^\theta+H_s^\theta) \tag{A.17}$$

$$E_i^\theta+E_s^\theta = -Z_s(H_i^x+H_s^x) \tag{A.18}$$

where $Z_s=(1+j)\sqrt{\frac{\mu_o\omega}{2\sigma}}$ is the surface impedance of the wire (Jackson 1962).

We finally find the following expressions for the components of the surface current:

$$K^x = \frac{E_o}{F}\cdot\frac{\alpha'}{(1-\alpha^2)\,H_0^{(2)}(k'a)-j\frac{Z_s}{Z_o}\sqrt{1-\alpha^2}H_1^{(2)}(k'a)} \tag{A.19}$$

$$K^\theta = \frac{E_o}{F}\cdot\frac{\frac{Z_s}{Z_o}(\gamma'\beta-\beta'\gamma)}{H_0^{(2)}(k'a)+j\frac{Z_s}{Z_o}\sqrt{1-\alpha^2}\left[\frac{H_0^{(2)}(k'a)}{k'a}-H_1^{(2)}(k'a)\right]}. \tag{A.20}$$

These last two equations can be inserted in equations (A.10)-(A.14) to calculate the value of the fields at any point exterior to the wire. For a good conductor the internal fields are practically inexistent.

3. The polarizing grid.

3.1. Analysis.

With the solution for a single wire at hand, the problem of a configuration of an infinite number of wires of infinite length separated by a distance d is simplified if one realizes that every wire will be induced with the same surface current $\mathbf{K}$. The only difference will be a phase term in the current density $\mathbf{J}(\mathbf{r})$, given by equation (A.4), which depends on the position of the wire along the y-axis. The same thing can be said for the scattered fields from any given wire, one only has to replace y_o by nd in equations (A.10)-(A.15), where n is an integer that determines the position of the wire.

If the scattered fields are now just the sum of all the different scattered fields from the individual wires, care must however be taken in evaluating the surface current. First, when one matches the boundary conditions it must be done simultaneously at the surface of every wires. However, since we are dealing with an infinite number of infinitely long wires subjected to the same incident plane wave, it turns out that it is sufficient to do so for only one of the wires. If the boundary conditions are matched for one wire they will be for all. We have chosen for our calculations the "center" wire at $n = 0$. Second, to match the boundary conditions we must express the scattered fields of each and every wire in a cylindrical coordinate system centered on the position of this "center" wire.

When this is done, we find the following expressions for the components of the induced surface current:

$$K^x = \frac{E_o}{F} \cdot \frac{\alpha'}{\Delta_x} \tag{A.21}$$

$$K^\theta = \frac{E_o}{F} \cdot \frac{\frac{Z_s}{Z_o}(\gamma'\beta - \beta'\gamma)}{\Delta_\theta} \tag{A.22}$$

with

$$\Delta_x = \left(1-\alpha^2\right) S_1 - j\frac{Z_s}{Z_o}\cdot\sqrt{1-\alpha^2}H_1^{(2)}(k'a) \tag{A.23}$$

$$\Delta_\theta = H_0^{(2)}(k'a) + j\frac{Z_s}{Z_o}\cdot\sqrt{1-\alpha^2}S_2 \tag{A.24}$$

and

$$S_1 = H_0^{(2)}(k'a) + 2\sum_{n=1}^{\infty} H_0^{(2)}(k'nd)\cos(k\beta nd) \tag{A.25}$$

$$S_2 = \frac{H_0^{(2)}(k'a)}{k'a} - H_1^{(2)}(k'a) + 2\sum_{n=1}^{\infty}\left[\frac{H_0^{(2)}(k'nd)}{k'nd} - H_1^{(2)}(k'nd)\right]\cos(k\beta nd)\,. \tag{A.26}$$

We will give in section 3.4 adequate approximations for Δ_x and Δ_θ that will greatly simplify the evaluation of the reflection and transmission coefficients which are soon to follow.

By using the appropriate expansions for series of Hankel's functions we can write down the expressions for the components of the total electric field far away from the grid:

$$\begin{aligned}
E_T^x(\mathbf{r}) &= \alpha' E_o \exp(-j\mathbf{k}\cdot\mathbf{r}) - \frac{(1-\alpha^2)}{\gamma}\cdot\frac{\lambda F}{\pi d}K^x \exp(-jk\gamma|z-z_o|)\exp(-j\varphi)\\
E_T^y(\mathbf{r}) &= \beta' E_o \exp(-j\mathbf{k}\cdot\mathbf{r})\\
&\quad + \frac{\lambda F}{\pi d}\left[\frac{\alpha\beta}{\gamma}K^x + \frac{K^\theta}{\sqrt{1-\alpha^2}}\cdot\frac{z-z_o}{|z-z_o|}\right]\exp(-jk\gamma|z-z_o|)\exp(-j\varphi)\\
E_T^z(\mathbf{r}) &= \gamma' E_o \exp(-j\mathbf{k}\cdot\mathbf{r})\\
&\quad + \frac{\lambda F}{\pi d}\left[\alpha K^x\frac{z-z_o}{|z-z_o|} - \frac{\beta}{\gamma\sqrt{1-\alpha^2}}K^\theta\right]\exp(-jk\gamma|z-z_o|)\exp(-j\varphi)
\end{aligned}$$

where λ is the wavelength and $\varphi = k(\alpha x + \beta y + \gamma z_o)$. From these it is now straightforward to get the reflection and transmission coefficients (normalized to E_o) in the far-field:

$$R^x = -\frac{F}{E_o}\cdot\frac{\lambda}{\pi d}\cdot\frac{(1-\alpha^2)}{\gamma}K^x \tag{A.27}$$

$$R^y = \frac{F}{E_o}\cdot\frac{\lambda}{\pi d}\left[\frac{\alpha\beta}{\gamma}K^x - \frac{K^\theta}{\sqrt{1-\alpha^2}}\right] \tag{A.28}$$

$$R^z = -\frac{F}{E_o}\cdot\frac{\lambda}{\pi d}\left[\alpha K^x + \frac{\beta}{\gamma\sqrt{1-\alpha^2}}K^\theta\right] \tag{A.29}$$

$$T^x = \alpha' + R^x \tag{A.30}$$

$$T^y = \beta' + \frac{F}{E_o}\cdot\frac{\lambda}{\pi d}\left[\frac{\alpha\beta}{\gamma}K^x + \frac{K^\theta}{\sqrt{1-\alpha^2}}\right] \tag{A.31}$$

$$T^z = \gamma' + \frac{F}{E_o}\cdot\frac{\lambda}{\pi d}\left[\alpha K^x - \frac{\beta}{\gamma\sqrt{1-\alpha^2}}K^\theta\right] \tag{A.32}$$

where we have set $z_o = 0$ for simplicity.

Equations (A.27)-(A.32) along with (A.21)-(A.22), $F = \frac{\pi\mu_o\omega a}{2}$, $Z_s = (1+j)\sqrt{\frac{\mu_o\omega}{2\sigma}}$, and $Z_o = \sqrt{\frac{\mu_o}{\epsilon_o}}$ are the solution to the polarizing grid problem for cases where it is assumed that $k'a \ll 1$ and $a \ll d$.

For predictions of measurements made in the laboratory, one merely has to transform these coefficients to the laboratory coordinate system. If we adopt for this system the coordinates of the incident/transmitted (u, v, w) and reflected (u', v', w') plane waves defined in Figures 17 and 18, the last system of equations is simplified to:

$$R^{u'} = -\frac{F}{E_o}\cdot\frac{\lambda}{\pi d}\cdot\frac{1}{\gamma\sqrt{1-\gamma^2}}\left[\beta K^x - \frac{\alpha\gamma}{\sqrt{1-\alpha^2}}K^\theta\right] \tag{A.33}$$

$$R^{v'} = -\frac{F}{E_o}\cdot\frac{\lambda}{\pi d}\cdot\frac{1}{\gamma\sqrt{1-\gamma^2}}\left[\alpha\gamma K^x + \frac{\beta}{\sqrt{1-\alpha^2}}K^\theta\right] \tag{A.34}$$

$$R^{w'} = 0 \tag{A.35}$$

$$T^u = \alpha'' - \frac{F}{E_o}\cdot\frac{\lambda}{\pi d}\cdot\frac{1}{\gamma\sqrt{1-\gamma^2}}\left[\beta K^x + \frac{\alpha\gamma}{\sqrt{1-\alpha^2}}K^\theta\right] \tag{A.36}$$

$$T^v = \beta'' - \frac{F}{E_o}\cdot\frac{\lambda}{\pi d}\cdot\frac{1}{\gamma\sqrt{1-\gamma^2}}\left[\alpha\gamma K^x - \frac{\beta}{\sqrt{1-\alpha^2}}K^\theta\right] \tag{A.37}$$

$$T^w = 0 \tag{A.38}$$

with α'' and β'' related to the incident field by:

$$\mathbf{E}_i(\mathbf{r}) = E_o\,(\alpha''\mathbf{e}_u + \beta''\mathbf{e}_v)\exp(-jkw)\ .$$

As can be seen, the reflected and transmitted fields have no component along their respective direction of propagation as is required for the propagation of plane waves in free space.

3.2. Effects of grid imperfections.

So far we have assumed that there were no imperfections in the construction of the grid, obviously (and unfortunately) such is not the case in any given situation. It would be instructive if we could calculate the effects of errors that are likely to be introduced in the fabrication process. In this section we will provide expressions that will allow us to evaluate changes in the reflection and transmission coefficients induced by two possible imperfections: random errors in wire spacing and random variations in the size of the wire radius.

3.2.1. Random errors in wire spacing.

It is our experience that some of the commercially available grids when observed under a microscope show some defects in their assembly. Visually, the most obvious manifestation of this is in the inconsistency in the spacing between wires. In order to calculate the effect of these errors we have to go back to the discussion of section 3.1 that guided us into the evaluation of the induced current on the wires. Since we can no longer assume that the wires are evenly spaced, we must now realize that they will in general have different values for the

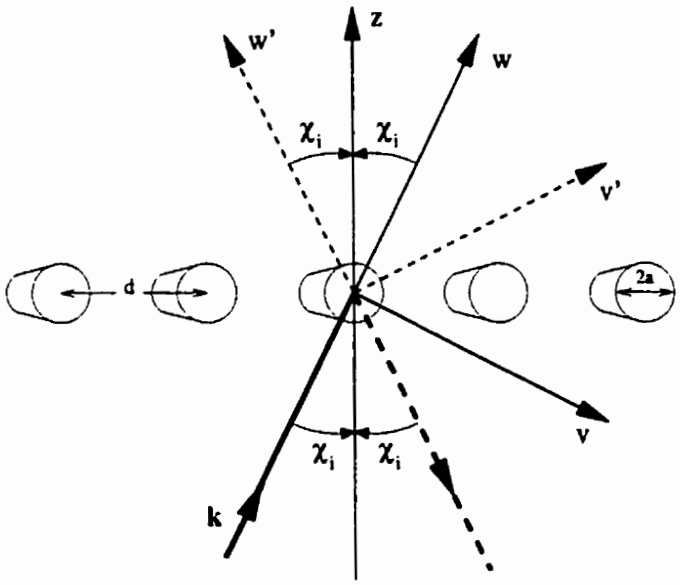

Fig. 18.— Definition of the system of coordinates (u', v', w') for the reflected wave in relation to the (u, v, w) system of the incident/transmitted waves introduced earlier in Figure 17. The u' and u-axes are one and the same and are pointing out of the page. The direction of propagation of the reflected wave is along the negative w'-axis.

current and fields on their surface. This will be made more apparent if we write down the expression for the x-component of the electric field on the surface of the "center" wire:

$$E_g^x(a) = -\left(1-\alpha^2\right) F \exp\left(-jk\left(\alpha x + \gamma z_o\right)\right) \sum_{n=-\infty}^{\infty} K_n^x\left(\xi\right) G_n\left(\xi\right) \tag{A.39}$$

with:

$$G_n\left(\xi\right) = \begin{cases} H_0^{(2)}(k'a)\exp\left(-jk\beta\xi_0\right) & ,n=0 \\ H_0^{(2)}\left(k'\left|nd+\xi_n\right|\right)\exp\left(-jk\beta\left(nd+\xi_n\right)\right) & ,n\neq 0\,. \end{cases} \tag{A.40}$$

K_n^x is the induced surface current on wire n and the ξ_n are statistically independent random errors in the positioning of the wires. Now, if $E\left\{x\right\}$ stands for the expected value of x and if we suppose that the errors have a zero mean, we can write:

$$E\left\{\xi_m^r\right\} = 0 \qquad ,r=1,3,5\ldots \tag{A.41}$$

$$E\left\{\xi_m^r\right\} = E\left\{\xi_n^r\right\} = E\left\{\xi^r\right\} \qquad ,\forall m,n \tag{A.42}$$

$$E\left\{\xi_m^r\xi_n^s\right\} = E\left\{\xi_m^r\right\}E\left\{\xi_n^s\right\} \qquad ,m\neq n \tag{A.43}$$

$$\overline{\xi^m K^x} = \overline{\xi_n^m K_n^x} = E\left\{\xi_n^m K_n^x\right\} \qquad ,\forall m,n\,. \tag{A.44}$$

The first equation is deduced from the supposed evenness of the probability density function of the errors, the second states that their statistics are the same across the grid and the third expresses their statistical independence. The last of these equations arises from the fact that if we were to test a large number of similar grids, every wire would exhibit the same average value $\overline{\xi^m K^x}$ for any induced surface current moment (independent of its position n).

We will not go into the details of the calculations as they are somewhat lengthy, but it can be shown that if we apply this last set of equations and expand $K_n^x\left(\xi\right)$ and $G_n(\xi)$ with

their Taylor series around $\xi_m = 0$ while solving for the boundary conditions, we can find an expression (valid to the second order in ξ) for the average longitudinal surface current:

$$\overline{K^x} \simeq K^x \left[1 - \frac{E\{\xi^2\}}{\sum_{n=-\infty}^{\infty} G_n(0)} \sum_{m=-\infty}^{\infty} \left\{ \frac{1}{2} \frac{\partial^2 G_m}{\partial \xi_m{}^2} - \frac{(1-\alpha^2)}{\Delta_x} \left[\frac{\partial G_m}{\partial \xi_m} \right]^2 \right\}_{\xi_m=0} \right]$$

where K^x is the current induced on the wires of a perfect grid and is given by equation (A.21). One sees that the errors bring a perturbation which is proportional to their common variance.

If the same approach is used to calculate the effect of such random errors on the value of the azimuthal surface current K_n^θ, one finds that it remains unaffected:

$$\overline{K^\theta} \simeq K^\theta$$

with K^θ given by equation (A.22).

From this we could then proceed and calculate the expected value of the reflection and transmission coefficients by evaluating equation (A.39) (and the corresponding equations for the y and z directions) in the far field, when this is accomplished we find that the coefficients have exactly the same form as shown in equations (A.27)-(A.32) (or (A.33)-(A.38)). We then merely have to replace K^x and K^θ by $\overline{K^x}$ and $\overline{K^\theta}$ respectively.

3.2.2. Random errors in the wire radius (wire to wire).

Another type of error which can be analyzed is one concerning the random variation in the size of the wire radius, which we will denote by the letter η. More explicitly, we are considering differences between wires and not variations along a single wire; we assume the diameter of a wire to be constant but somewhat uncertain in its value. This is the kind

phenomenon that could occur if the wires were stretched with slightly different tensions when installed. We can proceed in the same manner as we did in the last section for the analysis of the boundary conditions and the fields away from the grid. When this is done we get:

$$\overline{K^x} \simeq K^x \left[1 - \frac{E\{\eta^2\}}{\sum_{n=-\infty}^{\infty} G_n(0)} \left\{ \frac{1}{2} \frac{\partial^2 G_0}{\partial \eta_0{}^2} + \frac{1}{a} \frac{\partial G_0}{\partial \eta_0} - \frac{(1-\alpha^2)}{\Delta_x} \left[\frac{\partial G_0}{\partial \eta_0} \right]^2 \right\}_{\eta_0=0} \right]$$

$$\overline{K^\theta} \simeq K^\theta \left[1 - \frac{E\{\eta^2\}}{G_0(0)} \left\{ \frac{1}{2} \frac{\partial^2 G_0}{\partial \eta_0{}^2} + \frac{1}{a} \frac{\partial G_0}{\partial \eta_0} - \frac{1}{\Delta_\theta} \left[\frac{\partial G_0}{\partial \eta_0} \right]^2 \right\}_{\eta_0=0} \right]$$

where η_n is the random error in the size of the radius of wire n, G_n is given by equation (A.40) (with $\xi = 0$ and a replaced by $a+\eta$) and Δ_x and Δ_θ by (A.23) and (A.24) respectively. Again the expected value of the different coefficients can be obtained by replacing the current components K^x and K^θ by $\overline{K^x}$ and $\overline{K^\theta}$ in equations (A.27)-(A.32) (or (A.33)-(A.38)). It will also be noted that the errors bring a perturbation term which is proportional to their common variance.

3.2.3. Predictions and comparison with experiments.

Now that we have derived the equations for the reflection and transmission coefficients it would be interesting to compare the predictions that our model makes with experimental data. Although we have independently treated the two types of errors, it is nevertheless obvious that within the limit of precision of our analysis (small errors) that they can both be simultaneously added in the expressions for the reflection and transmission coefficients. Doing so would in principle allow us to compare theory and experiments as actual grids are liable to exhibit both kinds of defects. This also suggests though that it might be impossible to separate the effects of both errors in measurements. It turns out, however, that the perturbations caused by the errors in the size of the wire are predicted by our model to be

significantly smaller than those caused by the errors of the other type, it therefore seems appropriate to neglect them. This is what we do in what follows.

Shapiro & Bloemhof (1990) have published measurements of the unwanted cross-polarized transmittance through three grids on which they had purposely introduced random errors in the wire positioning. They quoted the errors in term of the random variation in the distance between wires (pitch) with amplitudes of 7%, 23% and 52% of the mean wire separation (aimed at 108 μm with a wire radius of 12.5 μm). We must divide these values by a factor of $\sqrt{2}$ in order to relate them to our errors ξ_n since we have defined these as pertaining to the absolute position of the wires. Figure 19 shows a comparison of our model's predictions with their measurements done for cases where the incoming field is at normal incidence to the grid and polarized parallel to the wire orientation. Although the agreement is not perfect, the outcome is very satisfactory as the theoretical curves exhibit the right behavior with frequency and error amplitude.

3.3. The scattering matrix and the impedance model.

3.3.1. The scattering matrix and the principal axes of a grid.

The relationship between the reflection and transmission coefficients in equations (A.33)-(A.38) is reminiscing of what is often encountered in microwave engineering in the analysis of systems that can be accurately dealt with using a lumped-elements model. With this in mind, it is tempting to consider any problem involving a polarizing grid by treating the different components as lumped and interconnected through a transmission line of characteristic impedance Z_o (Lamb 1997). We can then go ahead and model the grid as a 4-port device since the reflection and transmission coefficients given by the aforementioned set of equations provides us with the scattering parameters at each port.

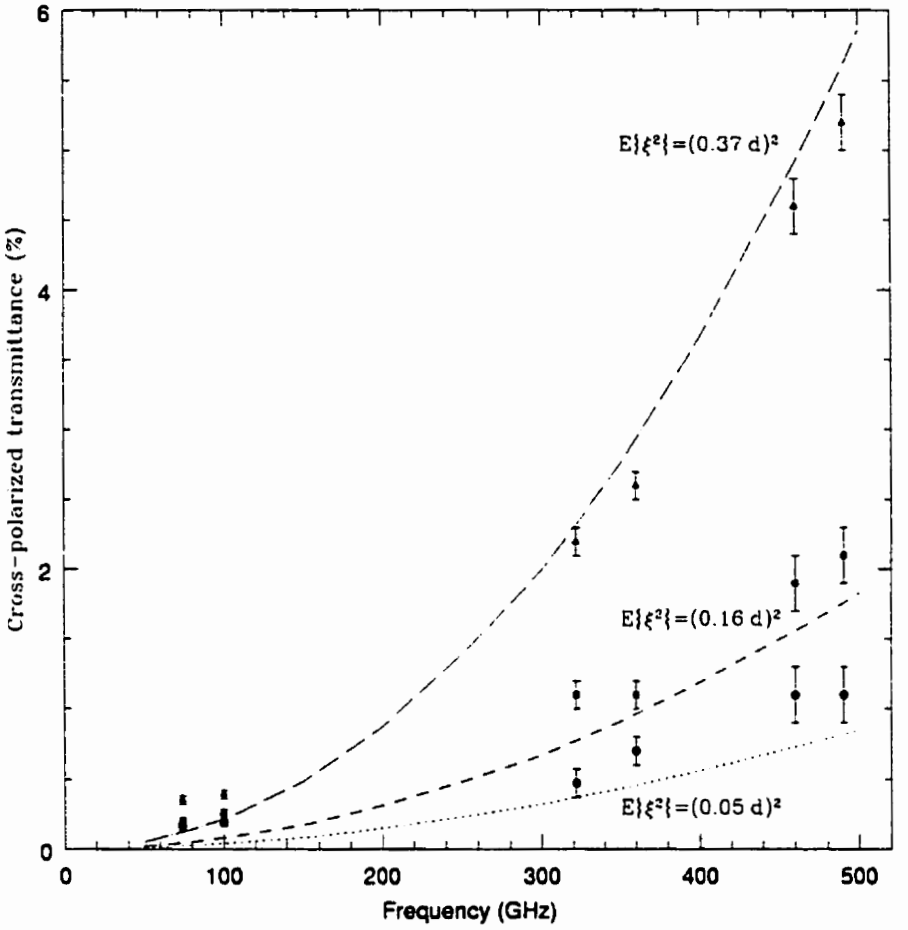

Fig. 19.— Curves of predicted values for the cross-polarized transmittance plotted against experimental data from Shapiro & Bloemhof (1990) and Bloemhof (1998). The three grids have a random error (1-σ) in wire positioning of 5%, 16% and 37% with mean distance between wires of 103 μm, 109 μm and 114 μm respectively; they all have a wire radius of 12.5 μm.

In this context, it is more convenient to work with a single coordinate system (u, v, w) (see Figures 17 and 18) for both the incident/transmitted and reflected plane waves since we can assume that their propagation is done along the same transmission line (it is however understood that, in reality, away from normal incidence the transmitted and reflected waves travel along different axes). We therefore assume that the incident/transmitted fields travel along the w-axis (with the u-axis vertical and the v-axis horizontal) and the reflected fields along the negative w-axis as seen from a given side of the grid.

Since there are two possible independent states of polarization (with the field aligned along the u or v-axes), where the waves can travel either toward or away from the grid, we need two ports on each side of the grid. So for example, if the incident wave on a given port has an electric field polarized along a given axis we can define 4 scattering parameters: one for the reflected signal at the input port and three for the transmissions to the other ports. The same thing can be done for every port leading to a total of 16 scattering parameters.

In what follows, a scattering parameter s_{mn} is defined with the 3 ports $m \neq n$ terminated with the line characteristic impedance Z_o. Also, each port n has two signals: an incoming signal E_n^+ and an outgoing signal E_n^-; $n = 1, 2$ (3, 4 on the other side of the grid) refer to polarization along the u and v axes respectively. The scattering matrix relates the different signals as follows:

$$\begin{bmatrix} E_1^- \\ E_2^- \\ E_3^- \\ E_4^- \end{bmatrix} = \begin{bmatrix} s_{11} & s_{12} & s_{13} & s_{14} \\ s_{21} & s_{22} & s_{23} & s_{24} \\ s_{31} & s_{32} & s_{33} & s_{34} \\ s_{41} & s_{42} & s_{43} & s_{44} \end{bmatrix} \begin{bmatrix} E_1^+ \\ E_2^+ \\ E_3^+ \\ E_4^+ \end{bmatrix} . \tag{A.45}$$

The elements of the matrix can be directly evaluated from equations (A.33)-(A.38) and shown to be:

$$\mathbf{S} = \begin{bmatrix} R^{uu} & R^{uv} & T^{uu} & T^{uv} \\ R^{uv} & R^{vv} & T^{uv} & T^{vv} \\ T^{uu} & T^{uv} & R^{uu} & R^{uv} \\ T^{uv} & T^{vv} & R^{uv} & R^{vv} \end{bmatrix} \tag{A.46}$$

with:

$$R^{uu} = -\frac{\lambda}{\pi d} \cdot \frac{1}{\gamma(1-\gamma^2)} \left[\beta^2 \cdot \frac{1}{\Delta_x} - \frac{\alpha^2\gamma^2}{\sqrt{1-\alpha^2}} \cdot \frac{Z_s}{Z_o} \cdot \frac{1}{\Delta_\theta} \right] \tag{A.47}$$

$$R^{vv} = -\frac{\lambda}{\pi d} \cdot \frac{1}{\gamma(1-\gamma^2)} \left[\alpha^2\gamma^2 \cdot \frac{1}{\Delta_x} - \frac{\beta^2}{\sqrt{1-\alpha^2}} \cdot \frac{Z_s}{Z_o} \cdot \frac{1}{\Delta_\theta} \right] \tag{A.48}$$

$$R^{uv} = -\frac{\lambda}{\pi d} \cdot \frac{\alpha\beta}{(1-\gamma^2)} \left[\frac{1}{\Delta_x} + \frac{1}{\sqrt{1-\alpha^2}} \cdot \frac{Z_s}{Z_o} \cdot \frac{1}{\Delta_\theta} \right] \tag{A.49}$$

$$T^{uu} = 1 - \frac{\lambda}{\pi d} \cdot \frac{1}{\gamma(1-\gamma^2)} \left[\beta^2 \cdot \frac{1}{\Delta_x} + \frac{\alpha^2\gamma^2}{\sqrt{1-\alpha^2}} \cdot \frac{Z_s}{Z_o} \cdot \frac{1}{\Delta_\theta} \right] \tag{A.50}$$

$$T^{vv} = 1 - \frac{\lambda}{\pi d} \cdot \frac{1}{\gamma(1-\gamma^2)} \left[\alpha^2\gamma^2 \cdot \frac{1}{\Delta_x} + \frac{\beta^2}{\sqrt{1-\alpha^2}} \cdot \frac{Z_s}{Z_o} \cdot \frac{1}{\Delta_\theta} \right] \tag{A.51}$$

$$T^{uv} = -\frac{\lambda}{\pi d} \cdot \frac{\alpha\beta}{(1-\gamma^2)} \left[\frac{1}{\Delta_x} - \frac{1}{\sqrt{1-\alpha^2}} \cdot \frac{Z_s}{Z_o} \cdot \frac{1}{\Delta_\theta} \right] \tag{A.52}$$

where Δ_x and Δ_θ are given by equations (A.23) and (A.24) respectively.

We can go one step further and render things considerably simpler if we make a change of coordinates and use the following as eigenvectors instead of $\mathbf{e_u}$ and $\mathbf{e_v}$:

$$\mathbf{p_1} = \frac{\beta\mathbf{e_u} + \alpha\gamma\mathbf{e_v}}{\sqrt{\beta^2 + \alpha^2\gamma^2}}$$

$$\mathbf{p_2} = \frac{-\alpha\gamma\mathbf{e_u} + \beta\mathbf{e_v}}{\sqrt{\beta^2 + \alpha^2\gamma^2}}.$$

From now on we will refer to these as the *principal axes* of the grid (for reasons that will soon become apparent). A close examination of the first of these two equations shows

that $\mathbf{p}_1$ is parallel to the projection of the direction of the wires in the plane of the incident field. The matrix $\mathbf{S}$ then transforms into a simple irreducible representation as can be seen if we also interchange the second row with the third and the second column with the third:

$$\mathbf{S} = \begin{bmatrix} R_{\|} & T_{\|} & 0 & 0 \\ T_{\|} & R_{\|} & 0 & 0 \\ 0 & 0 & R_{\perp} & T_{\perp} \\ 0 & 0 & T_{\perp} & R_{\perp} \end{bmatrix} \tag{A.53}$$

where

$$R_{\|} = -\frac{\lambda}{\pi d} \cdot \frac{(1-\alpha^2)}{\gamma} \cdot \frac{1}{\Delta_x} \tag{A.54}$$

$$R_{\perp} = \frac{Z_s}{Z_o} \cdot \frac{\lambda}{\pi d} \cdot \frac{\sqrt{1-\alpha^2}}{\gamma} \cdot \frac{1}{\Delta_\theta} \tag{A.55}$$

$$T_{\|} = 1 + R_{\|} \tag{A.56}$$

$$T_{\perp} = 1 - R_{\perp}\,. \tag{A.57}$$

We then have a further simplification in the modeling of the grid, evidently equations (A.54)-(A.57) represent the reflection and transmission coefficients along the two principal axes. Since $R_{\perp}$ scales as $\frac{Z_s}{Z_o}$, it follows that reflections along $\mathbf{p}_2$ will in general be weak therefore justifying the common approximation $T_{\perp} \simeq 1$.

This last representation has the advantage of simplifying calculations since it allows us to decompose any incident field into two non-interacting components, one along each of the principal axes. That is, a field polarized along one of the principal axis scatters only in this same polarization state (as can be deduced from the block-diagonal form of equation (A.53)). It is also interesting to note that even though we have defined the principal axes within the framework of our approximation of the grid ($k'a \ll 1$ and $a \ll d$), the result obtained here

still holds in the general case (see Appendix I for a proof). This implies that in the event where one wishes to use a different approach to solve (numerically or else) the scattering off a grid of arbitrary characteristics, it will always be possible to split the incoming field along the principal axes therefore avoiding cross-polarization terms and greatly simplifying the solution.

3.3.2. The impedance model.

It seems reasonable to think that a grid could also be modeled with another representation where the scattering matrix is replaced by an impedance matrix which contains the same number of elements since as before, the grid is still treated as a 4-port device. In this case however, the matrix relates the total voltages (electric fields) and currents (magnetic fields) between each and every ports (Collin 1992). The scattering matrix formulation follows more naturally from our analysis and has the advantage of dealing with quantities (reflection and transmission coefficients) which are directly measurable whereas impedances are not (at least at the wavelengths considered here). The impedance model has however gotten a great deal of attention in the literature and seems to often be the way in which polarizing grids are characterized (Wait 1954, 1955a; Larsen 1962).

Taking advantage of the principal axes representation, it is possible to treat each two-dimensional block of the scattering matrix (equation (A.53)) separately. It can be shown that the impedance matrix $\mathbf{Z}_b$ corresponding to a given block $\mathbf{S}_b$ can be expressed as:

$$\mathbf{Z}_b = Z_o \cdot (\mathbf{I} \pm \mathbf{S}_b) \cdot (\mathbf{I} \mp \mathbf{S}_b)^{-1} \tag{A.58}$$

where $\mathbf{I}$ is the unit matrix and the upper and lower signs correspond respectively to the upper left and lower right blocks of the scattering matrix (equation (A.53)). Applying this

last equation to equation (A.53) we get:

$$\mathbf{Z} = \begin{bmatrix} Z_p & Z_p & 0 & 0 \\ Z_p & Z_p & 0 & 0 \\ 0 & 0 & Z_n & -Z_n \\ 0 & 0 & -Z_n & Z_n \end{bmatrix}$$

with:

$$\begin{aligned} Z_p &= -\frac{Z_o}{2} \cdot \frac{1+R_{\|}}{R_{\|}} \\ Z_n &= \frac{Z_o}{2} \cdot \frac{1-R_{\perp}}{R_{\perp}}. \end{aligned}$$

It follows quite naturally from equations (A.54)-(A.57) that we could have defined two impedances $Z_{\|}$ and $Z_{\perp}$:

$$\begin{aligned} Z_{\|} &= Z_o \cdot \frac{1+R_{\|}}{1-R_{\|}} \\ Z_{\perp} &= Z_o \cdot \frac{1-R_{\perp}}{1+R_{\perp}}. \end{aligned}$$

One can easily verify that $Z_{\|}$ and $Z_{\perp}$ are respectively equal to Z_p and Z_n placed in parallel to the characteristic impedance Z_o. We therefore see that the impedance matrix gives the "actual" impedance of the grid along each of the principal axes whereas the scattering matrix includes, as should be expected, the contribution of the load of characteristic impedance Z_o which is assumed to be connected to the appropriate ports when defining its parameters.

3.4. Approximations and selection of a grid.

We will now study more closely our simpler equations (A.54) and (A.55) for the reflection coefficients $R_{||}$ and $R_{\perp}$and try to find relations that will allow us to find a set of optimum parameters for the selection of a grid. But before we do so, it will be to our advantage to approximate the expressions for Δ_x and Δ_θ (equations (A.23) and (A.24)).

So if we limit ourselves to situations where $d \ll \lambda$, $a \ll \lambda$ and $Z_s \ll Z_o$ (good conducting wires) and use the proper expansion for Hankel's functions and series of Hankel's functions applicable in such cases (small arguments) we find:

$$\begin{aligned}\Delta_x \simeq\ & (1-\alpha^2)\left[\left\{\frac{\lambda}{\pi\gamma d}-\left(\frac{k'a}{2}\right)^2+\frac{1}{\sqrt{(1-\alpha^2)\,\pi Z_o\sigma\lambda}}\left(\frac{2}{k'a}\right)\right\}\right. \\ & +j\frac{2}{\pi}\left\{\ln\left(\frac{d}{2\pi a}\right)+\frac{\pi^2}{6}\left(\frac{d\gamma}{\lambda}\right)^2-\left(\frac{k'a}{2}\right)^2\left[1-\Psi-\ln\left(\frac{k'a}{2}\right)\right]\right. \\ & \left.\left.+\sqrt{\frac{\pi}{4\,(1-\alpha^2)\,Z_o\sigma\lambda}}\left(\frac{2}{k'a}\right)\right\}\right] \qquad \text{(A.59)}\end{aligned}$$

$$\Delta_\theta \simeq 1-j\frac{2}{\pi}\left\{\Psi-\ln\left(\frac{k'a}{2}\right)\right\} \qquad \text{(A.60)}$$

where $\Psi \simeq 0.577215$ is Euler's constant. In equation (A.60) we have kept things to the lowest order possible as it is all that is needed ($R_\perp$ already scales as $\frac{Z_s}{Z_o}$, rendering unnecessary the need for terms of higher orders in Δ_θ), the same is not true for equation (A.59) for reasons that we shall encounter shortly.

We turn now to the problem of selecting the right parameters for a grid. If we decompose a given incident field into two components along the principal axes $\mathbf{p}_1$ and $\mathbf{p}_2$ (see section 3.3.1), a perfect grid would completely reflect the first of these and transmit the second ($R_{||} = -1$ and $T_\perp = 1$). The condition of perfect transmission can in principle be realized by selecting a good enough conducting material for the wires since $R_\perp \propto \frac{Z_s}{Z_o}$, we will therefore

not worry about it anymore. The condition of total reflection will dictate our choice for the parameters of the grid. A close study of equation (A.54) tells us that in order to achieve perfect reflection we must simultaneously satisfy the following relations for the real and imaginary parts of Δ_x:

$$\begin{aligned} \mathrm{Re}\{\Delta_x\} &= \frac{\lambda}{\pi d}\cdot\frac{(1-\alpha^2)}{\gamma} \\ \mathrm{Im}\{\Delta_x\} &= 0. \end{aligned}$$

Solving for these we then get:

$$a \simeq \left[\frac{\lambda^5}{(1-\alpha^2)^4\pi^7\sigma Z_o}\right]^{\frac{1}{6}} \tag{A.61}$$

$$d \simeq 2\pi a. \tag{A.62}$$

Had we kept equation (A.59) to the lowest order, we would have been unable to specify an optimum value for the wire radius but only the relation that binds d to a. It is also of interest to note that for a given wavelength, the finite size of the wire radius is, to this level of approximation, dictated by the conductivity σ; if we let $\sigma \to \infty$ then there is no restriction on the smallness of the radius.

In order to get an idea of the kind of values that can be expected for a and d, let's assume that we're working at normal incidence at a wavelength of 1 mm with a grid made of copper ($\sigma = 5.8 \times 10^7\ \Omega^{-1}\mathrm{m}^{-1}$). Using these, we obtain $a \simeq 11\,\mu$m and $d \simeq 70\,\mu$m.

It is at this point appropriate to discuss the implications of the two assumptions we made at the beginning concerning the wire radius and spacing, namely that $k'a \ll 1$ and $a \ll d$. It is important to make sure that a given choice of grid parameters are well within the boundaries of applicability of our model. As a mean to determine these boundaries,

we simulated the response of grids (and assemblies of grids, see section 4) for different combinations of wire radius and spacing and made sure that the results obtained were reliable (for example, it is obviously imperative that the magnitude of the reflection and transmission coefficients never exceed unity). As it turns out, there is a fairly strong restriction linking the size of the wires and the wavelength, but if one makes sure that $\lambda > 40\,a$ then one seems to be well within safe modeling conditions. a cannot be too small either. However, since for a good conductor (again let's use copper) the skin depth at 1 mm is on the order of 0.1 μm, our assumption of the existence of an idealized surface current is more than adequate. It seems that the second restriction concerning the spacing of the wires is not as binding as the first one. It is clear that $d > 2\,a$ for if not the wires would be touching, but it appears that everything is fine for $d > 4\,a$. Our proposed optimized values for the grid are therefore justified.

It is also appropriate to point out that using equations (A.59) and (A.60) for Δ_x and Δ_θ (with or without the optimal values for a and d given by equations (A.61) and (A.62)) along with the set (A.54)-(A.57) for the reflection and transmission coefficients along the principal axes renders the task of calculating the response of a grid a rather simple one. It becomes unnecessary to confront the more intimidating representations derived earlier in section 3.1 (compare with equations (A.21)-(A.32)).

4. The reflecting polarizer.

4.1. Analysis.

From the solution of the polarizing grid it is a somewhat natural extension to consider the more complicated problem of the reflecting polarizer. A reflecting polarizer consists of an assembly where a polarizing grid, like the one studied in the last section, is followed by

a mirror paralleling it at some distance z_o behind (effectively placing the mirror at $z = 0$).

It is appropriate in this case to use the method of images to solve this problem (Wait 1954). We then assume that images of both the incident and scattered fields are emanating from the other side of the mirror. This is equivalent to saying that the image world is made of a grid positioned at $z = -z_o$ with an image incident field impinging on it. Assuming that the mirror is made of a material of good conductivity, one can write for the image incident field $\mathbf{E}'_i(\mathbf{r})$:

$$\mathbf{E}'_i(\mathbf{r}) = E_o\,(\alpha'_m \mathbf{e}_x + \beta'_m \mathbf{e}_y - \gamma'_m \mathbf{e}_z)\exp(-jk(\alpha x + \beta y - \gamma z))$$

with:

$$\alpha'_m = \frac{1}{(1-\gamma^2)}\left[\alpha'\left(\alpha^2 R_{TM} + \beta^2 R_{TE}\right) + \alpha\beta\beta'\left(R_{TM} - R_{TE}\right)\right] \tag{A.63}$$

$$\beta'_m = \frac{1}{(1-\gamma^2)}\left[\beta'\left(\alpha^2 R_{TE} + \beta^2 R_{TM}\right) + \alpha\beta\alpha'\left(R_{TM} - R_{TE}\right)\right] \tag{A.64}$$

$$\gamma'_m = \gamma' R_{TM} \tag{A.65}$$

where R_{TE} and R_{TM} are the reflection coefficients of the mirror, with a dependency on the angle of incidence, for transverse electric and transverse magnetic modes of incoming radiation respectively (Fowles 1975).

One can go through calculations similar to those carried out in section 3.1 and find the following relations between the components of the surface currents of the "real" and image grids:

$$K'^x = \frac{\alpha'_m}{\alpha'} K^x$$

$$K'^\theta = -\frac{\gamma'_m\beta - \beta'_m\gamma}{\gamma'\beta - \beta'\gamma} K^\theta$$

where $\mathbf{K}'$ stands for the surface current of the image grid.

From these and by matching the boundary conditions at the grid, it is straightforward, but tedious, to solve for the problem. We give here the final results:

$$K^x = \frac{E_o}{F} \cdot \frac{2j\alpha' \,\mathrm{sn}(k\gamma h)}{(1-\alpha^2)\,\Delta S_1 - j\frac{Z_s}{Z_o}\sqrt{1-\alpha^2}\Delta S_4} \tag{A.66}$$

$$K^\theta = \frac{E_o}{F} \cdot \frac{2\frac{Z_s}{Z_o}(\gamma'\beta - \beta'\gamma)\,\mathrm{cs}(k\gamma h)}{\Sigma S_3 + j\frac{Z_s}{Z_o}\sqrt{1-\alpha^2}\,\Sigma S_2} \tag{A.67}$$

$$R^x = \alpha'_m - \frac{F}{E_o} \cdot \frac{2\lambda}{\pi d} \cdot \frac{(1-\alpha^2)}{\gamma} j\,\mathrm{sn}(k\gamma h)\,K^x \tag{A.68}$$

$$R^y = \beta'_m + \frac{F}{E_o} \cdot \frac{2\lambda}{\pi d}\left[j\frac{\alpha\beta}{\gamma}\,\mathrm{sn}(k\gamma h)\,K^x - \frac{\mathrm{cs}(k\gamma h)}{\sqrt{1-\alpha^2}}\,K^\theta\right] \tag{A.69}$$

$$R^z = -\gamma'_m - \frac{F}{E_o} \cdot \frac{2\lambda}{\pi d}\left[j\alpha\,\mathrm{sn}(k\gamma h)\,K^x + \frac{\beta\,\mathrm{cs}(k\gamma h)}{\gamma\sqrt{1-\alpha^2}}\,K^\theta\right] \tag{A.70}$$

where

$$\mathrm{sn}(x) = \frac{1}{2j}\left[\exp(jx) - r_x \exp(-jx)\right]$$

$$\mathrm{cs}(x) = \frac{1}{2}\left[\exp(jx) + r_\theta \exp(-jx)\right]$$

$$\Delta S_1 = H_0^{(2)}(k'a) - r_x H_0^{(2)}(k'2h) + 2\sum_{n=1}^{\infty}\left[H_0^{(2)}(k'nd) - r_x H_0^{(2)}\left(k'\sqrt{(nd)^2+4h^2}\right)\right]\cos(k\beta nd)$$

$$\Delta S_4 = H_1^{(2)}(k'a) - r_x H_1^{(2)}(k'2h)$$

$$\Sigma S_2 = \left[\frac{H_0^{(2)}(k'a)}{k'a} - H_1^{(2)}(k'a)\right] + r_\theta\left[\frac{H_0^{(2)}(k'2h)}{k'2h} - H_1^{(2)}(k'2h)\right] + 2\sum_{n=1}^{\infty}\cos(k\beta nd)\left\{\left[\frac{H_0^{(2)}(k'nd)}{k'nd} - H_1^{(2)}(k'nd)\right] + r_\theta\left[\frac{H_0^{(2)}\left(k'\sqrt{(nd)^2+4h^2}\right)}{k'\sqrt{(nd)^2+4h^2}} - H_1^{(2)}\left(k'\sqrt{(nd)^2+4h^2}\right)\right]\right\}$$

$$\Sigma S_3 = H_0^{(2)}(k'a) + r_\theta H_0^{(2)}(k'2h)$$

and

$$r_x = -\frac{\alpha'_m}{\alpha'}$$
$$r_\theta = -\frac{\gamma'_m\beta - \beta'_m\gamma}{\gamma'\beta - \beta'\gamma}.$$

We have also replaced $-z_o$ by h ($h > 0$) so that the distance between the mirror and the grid is expressed by a positive quantity. This set of equations along with equations (A.63)-(A.65) and $F = \frac{\pi\mu_o\omega a}{2}$, $Z_s = (1+j)\sqrt{\frac{\mu_o\omega}{2\sigma}}$, $Z_o = \sqrt{\frac{\mu_o}{\epsilon_o}}$ give us the solution of the reflecting polarizer problem for cases where $k'a \ll 1$ and $a \ll d$.

As was the case for the polarizing grid, if we transform those coefficients to the laboratory frame of coordinates (u', v', w') (see Figure 18) we obtain:

$$R^{u'} = \alpha''_m - \frac{F}{E_o}\cdot\frac{2\lambda}{\pi d}\cdot\frac{1}{\gamma\sqrt{1-\gamma^2}}\cdot\left[j\beta\,\mathrm{sn}(k\gamma h)\,K^x - \frac{\alpha\gamma\,\mathrm{cs}\,(k\gamma h)}{\sqrt{1-\alpha^2}}\,K^\theta\right] \quad \text{(A.71)}$$

$$R^{v'} = \beta''_m - \frac{F}{E_o}\cdot\frac{2\lambda}{\pi d}\cdot\frac{1}{\gamma\sqrt{1-\gamma^2}}\cdot\left[j\alpha\gamma\,\mathrm{sn}(k\gamma h)\,K^x + \frac{\beta\,\mathrm{cs}(k\gamma h)}{\sqrt{1-\alpha^2}}\,K^\theta\right] \quad \text{(A.72)}$$

$$R^{w'} = 0 \quad \text{(A.73)}$$

with α''_m and β''_m given by:

$$\alpha''_m = \frac{1}{(1-\gamma^2)}\left[\alpha''\left(\alpha^2 R_{TM} + \beta^2 R_{TE}\right) + \alpha\beta\beta''\left(R_{TM} - R_{TE}\right)\right] \quad \text{(A.74)}$$

$$\beta''_m = \frac{1}{(1-\gamma^2)}\left[\beta''\left(\alpha^2 R_{TE} + \beta^2 R_{TM}\right) + \alpha\beta\alpha''\left(R_{TM} - R_{TE}\right)\right] \quad \text{(A.75)}$$

and finally α'' and β'' are related to the incident field by:

$$\mathbf{E}_i(\mathbf{r}) = E_o\left(\alpha''\mathbf{e}_u + \beta''\mathbf{e}_v\right)\exp\left(-jkw\right).$$

4.2. Solution using the scattering matrix.

The scattering matrix representation of the polarizing grid gives us the advantage of rendering possible the solution of problems that would be otherwise extremely difficult, if not impossible, to solve using Maxwell's equations. For example, a solution of the reflecting polarizer problem is straightforward if we "connect" the mirror to ports 3 and 4 of the grid at a distance h behind. Using the definitions introduced in the discussion leading to equation (A.45) we have:

$$\begin{aligned} E_3^+ &= E_3^- R_{TE} \exp(-jk\gamma 2h) \\ E_4^+ &= E_4^- R_{TM} \exp(-jk\gamma 2h) \end{aligned}$$

where R_{TE} and R_{TM} are as defined in the previous section.

We can then solve for E_1^- and E_2^- and find results that are in agreement with those obtained in the previous section.

4.3. Experimental results.

Reflecting polarizers like those studied here were tested at the OVRO for polarimetry in the wavelength ranges of 1.3 mm as well as successfully used for polarimetry observations at 3 mm (Akeson 1997; Akeson et al. 1996). They are composed of an aluminum mirror and a grid of gold-plated tungsten wires of 25 μm diameter and spaced at an interval of 125 μm. The inside diameter of the grid is roughly 16 cm, some 25 times bigger than the incident Gaussian beam at 1.3 mm (Akeson 1997).

In this section, we will compare data obtained in the calibration of these polarizers at 1.3 mm with the model calculated earlier. In the experimental set-up, the incident beam is

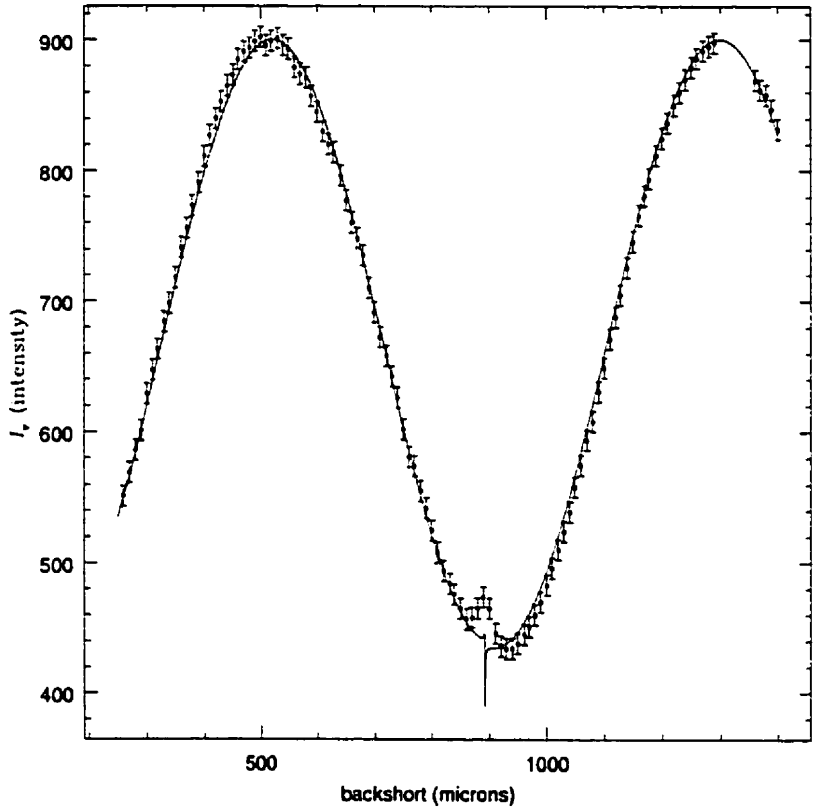

Fig. 20.— Calibration data from antenna #6 of the OVRO array. Data points are shown with an error bar and the solid curve is a least squares fit from the model presented in this paper.

composed of radiation emanating from a hot load (absorber at room temperature) polarized along the vertical axis and a cold load (absorber in liquid nitrogen) along the horizontal axis. The beam is incident on the polarizers at an angle of $\chi_i = 34\,\text{deg.}$ with the grid rotated by $\varphi_g = \pm 50.3\,\text{deg.}$ relative to the vertical, all in the coordinate system of the laboratory (coordinates (u,v,w) of Figure 17). These values can be inserted in the appropriate equations of our earlier analysis and used to test our model against the experimental data.

The calibration consists in using our model to map out the actual distance between the grid and the mirror as the latter is moved with a micro-positioner which is part of the assembly. When this is done, this distance can then be precisely adjusted to $\frac{\lambda}{8\gamma}$ in order to use the polarizer as a reflecting quarter-wave plate for polarimetry measurements. The grid rotation angle φ_g must also be calibrated so that it can be set to the proper value that will allow the transformation of incident linear polarization to circular polarization. (This condition is met for $\beta = \pm\alpha\gamma$ (or $\tan(\varphi_g) = \frac{\pm 1}{\cos(\chi_i)}$), as can be asserted from our earlier discussion of the principal axes of a grid in section 3.3, this gives $\varphi_g = \pm 50.3\,\text{deg}$ as quoted above).

Figure 20 shows the results obtained from such measurements (of the reflected polarized intensity along the horizontal v'-axis in the laboratory coordinate system) made on antenna #6 of the OVRO array at a frequency of 232.037 GHz when the separation between the grid and the mirror is varied through a range of a several hundreds of microns. Accompanying the data points is a least square fit of our model (solid curve) with no free parameters as far as the grid is concerned, only the hot and cold load levels and the offset in the mirror-grid separation were allowed to be fitted. The agreement is very good. The main shortcoming of the fit is at a backshort position of roughly 900 μm where a resonance is evident from the data. The model also shows a resonance at the same position but the fit is not perfect. This feature is caused by the small amount of unwanted transmission from the component of the

incident electric field aligned with one of the principal axes ($\mathbf{p}_1$) which gets trapped between the grid and the mirror.

Before we try to explain the differences in width and shape of the resonance, we would first like to show two ways by which it can be suppressed (such a response from the polarizer is a nuisance when trying to calibrate it and should be avoided).

First, reducing the amount of unwanted transmission through the grid would certainly have a damping effect on the resonance. We have shown how to do just that in section 3.4 when defining a set of optimum parameters for a grid, so using equations (A.61) and (A.62) we find for our application $a \simeq 24\,\mu$m and $d \simeq 148\,\mu$m. Figure 21 shows a comparison of the simulated responses for the polarizer tested at OVRO and our optimized polarizer. As can be seen, any sign of the resonance has disappeared in the latter.

Another way of avoiding the resonance, while still using the same original grid with $a = 12.5\,\mu$m and $d = 125\,\mu$m, is to replace the mirror with another grid (Young 1997) and rotate both of them in such a way that the projected orientation of their wires in the plane of the incident field are aligned with a principal axis. By this we mean that the two grids have their angle of rotation specified by $\tan(\varphi_g) = \frac{1}{\cos(\chi_i)}$ (or $\varphi_g = 50.3\,\text{deg}$) and $\tan(\varphi_g) = \frac{-1}{\cos(\chi_i)}$ (or $\varphi_g = -50.3\,\text{deg}$) respectively. This would ensure that the unwanted transmitted field from the first grid would almost be entirely transmitted through the second grid, therefore getting rid of the resonance.

Obviously, trying to solve for such a configuration using Maxwell's equations would be a formidable task. We can however use our scattering matrix model developed in section 3.3. We then have to define two matrices, one for each grid, and solve the problem for cases where they are separated by a given distance while terminating the last grid by the line characteristic impedance Z_o ($E_3^+ = E_4^+ = 0$). We simulated the response predicted for such an arrangement of grids and got results that are practically identical to those presented in

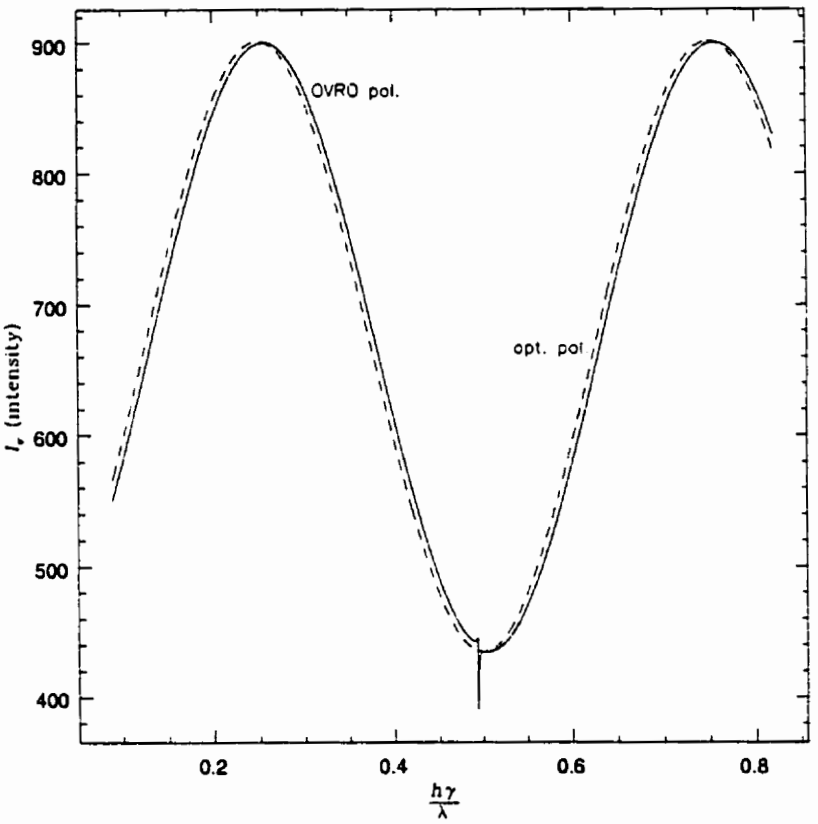

Fig. 21.— Comparison of the predicted results obtained for the polarizer tested at OVRO (solid curve) and our optimized polarizer (broken curve). The resonance is not present on the optimized polarizer's response.

Figure 21 for the optimum polarizer.

5. Grids and beams of radiation.

Until now we have restricted our analysis to cases where the dimensions of the grid (or the assembly) and the extent of the incident wave were assumed to be infinite. These simplifications were necessary in order to allow us to have a chance at a solution, as the reality of finite sizes brings severe difficulties in the analysis. It would however seem reasonable to suppose that if the incoming excitation can be properly represented by a beam of radiation which is of a size a few times smaller that the actual dimensions of the assembly that the results obtained with our analysis should still be valid. Indeed, one could argue that the incident beam should only induce currents in the vicinity of the area where it impinges on the assembly. There should therefore be little to no differences in its response whether it is infinite or not.

Although we believe this argument to be a reasonable one, we will show that the characteristics of the incoming radiation can be important in some cases. We will in fact argue that it can explain the discrepancies in the width and shape of the resonance observed in the response of the reflecting polarizer presented in section 4.3 (see Figure 20).

As a starting point, let's take note that we can always mathematically express a beam of radiation $E_o(\mathbf{r})$ as a summation of plane waves with different amplitude (and phase) and $\mathbf{k}$ vectors. For example, in the laboratory system of coordinates (u,v,w), the electric field along the u-axis $E_i^u(\mathbf{r},t) = \alpha'' E_o(\mathbf{r}) \exp(j\omega_o t)$ can be expressed by (using its Fourier transform in $(\omega, \mathbf{k})$-space and assuming the beam to be monochromatic at $\omega_o = kc$):

$$E_i^u(\mathbf{r},t) = \frac{\alpha''}{(2\pi)^4} \int_{-\infty}^{\infty} d\omega\, d^3k E_o(\mathbf{k},\omega) \exp\left[-j\left(\mathbf{k}\cdot\mathbf{r} - \omega t\right)\right] \qquad \text{(A.76)}$$

$$E_o(\mathbf{k},\omega) \;=\; 2\pi\delta(\omega-\omega_o)\int_{-\infty}^{\infty} d^3r' E_o(\mathbf{r}')\exp(j\mathbf{k}\cdot\mathbf{r}') \tag{A.77}$$

where $\delta(x)$ is Dirac's delta distribution.

Let's now assume that the incident radiation can be satisfactorily modeled using a circular Gaussian beam with a beam waist W_o and a Rayleigh range $z_R = \frac{\pi W_o^2}{\lambda}$. We also know that the resonance will occur for a grid-mirror separation of $h \simeq \frac{\pi}{k_z}$ for each spectral component, where k_z is the projection of the wave vector along the z-axis perpendicular to the reflecting polarizer (in the coordinates system of the grid of Figure 17). From this we can express the width of the resonance Δh as a function of k_z and Δk_z the spectrum extent along the same axis:

$$\Delta h \simeq \pi\frac{\Delta k_z}{k_z^2}.$$

We need to find an expression for Δk_z and this can be done as follows. Using the wave uncertainty relation, we can evaluate the spectrum extent in the laboratory system of axes as:

$$\begin{aligned}
\Delta k_u &\simeq W_o^{-1} \\
\Delta k_v &\simeq W_o^{-1} \\
\Delta k_w &\simeq z_R^{-1}.
\end{aligned}$$

Transforming these in the coordinate system of the grid and inserting the result in the expression for the width of the resonance we find:

$$\Delta h \simeq \frac{\pi}{(k\gamma W_o)^2}\sqrt{W_o^2(1-\gamma^2)+\left(\frac{2\gamma}{k}\right)^2}. \tag{A.78}$$

When we use the corresponding values of the different parameters appearing in equation

(A.78) for the case of the reflecting polarizer discussed in the last section (λ = 1.3 mm, $\gamma = 0.83$ and $W_o = 3$ mm) we find $\Delta h \simeq 37\,\mu$m. If we take into account the finite bandwidth of the OVRO receivers (3 GHz), a similar exercise shows that at most only a few microns need to be added to the previous estimate. Although these numbers represent only a rough calculation of what could be expected, they nevertheless tell us that there will be a significant broadening of the resonant feature.

We will not try to produce a perfect fit to the data obtained at OVRO for this would require extensive modeling of our experimental set-up and therefore bring us to a level of complexity that we do not wish to tackle at this time. But using equations (A.76) and (A.77) and applying the result of our analysis of the reflecting polarizer for every spectral component hence calculated, we can get a better idea of the phenomenon considered here.

We have done this and the result is shown in Figure 22 where we present the result of a simulation of the effect of a Gaussian beam on the width and shape of the resonance exhibited by a reflecting polarizer of the kind discussed in section 4.3. The beam is converging with its waist situated some 10 cm "behind" the polarizer and the integrated power (over a beam width) is measured some distance away from the assembly in the far-field. Although there still remains some differences, this simulation shares a lot of the same features observed experimentally.

We believe that simulations like this one along with our earlier calculations provide convincing and compelling evidences for the importance of appropriately taking into account the nature of the incident radiation in the analysis of similar systems.

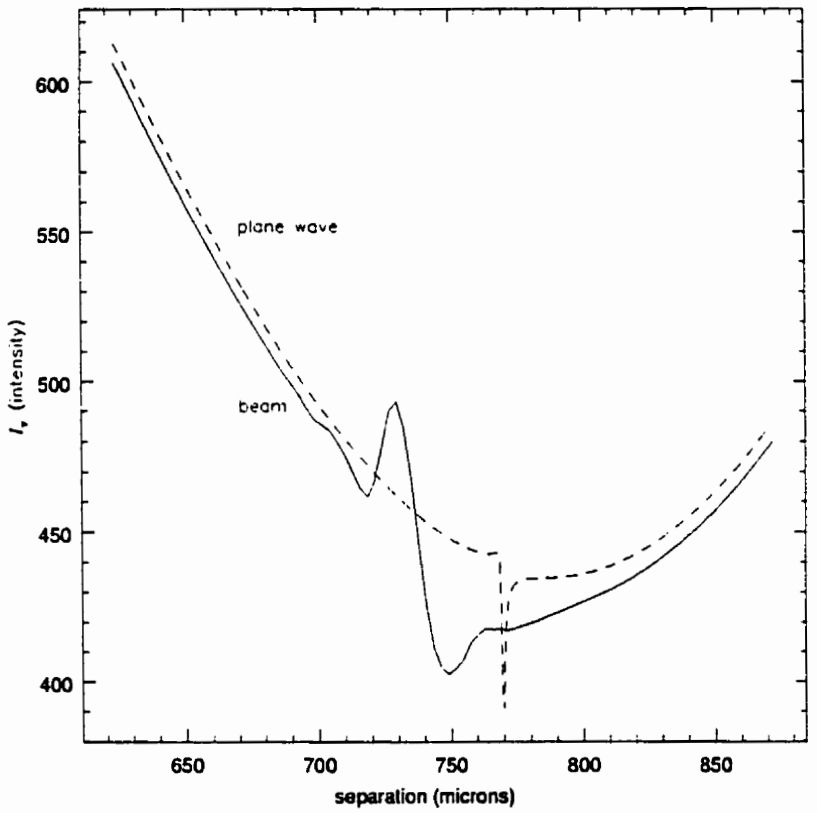

Fig. 22.— Simulation of the effect of a Gaussian beam ($W_o = 3$ mm) on the width and shape of the resonance exhibited by a reflecting polarizer as discussed in section 4.3. The broken and solid curves show the results predicted for an incident plane wave and a Gaussian beam respectively.

6. Conclusion.

In this paper, a general solution for the analysis of polarizing grids was presented; it is valid for arbitrary angles of incidence and of grid rotation. With it and the scattering matrix representation that derives from it, basically any configuration or system of grids can be analyzed as long as some assumptions concerning the wire radius and spacing are respected ($\lambda > 40\,a$ and $d > 4\,a$). This is not a severe restriction as most grid currently available satisfy those conditions, we refer the reader to Chambers et al. (1986, 1988) for cases where a larger size of wire is needed. Our analysis also allowed us to define a set of optimum values for both the wire radius and spacing as specified by the following equations:

$$\begin{aligned} a &\simeq \left[\frac{\lambda^5}{(1-\alpha^2)^4\,\pi^7\sigma Z_o}\right]^{\frac{1}{6}} \\ d &\simeq 2\pi a\,. \end{aligned}$$

We provided an analysis of the effects that two types of random errors can have on the performance of a grid. It was shown that errors in the wire spacing were the most important and could have some impact on the amount of unwanted polarization transmitted through a grid. In that respect, our model showed to be in good agreement with the experimental results of Shapiro & Bloemhof (1990).

Comparisons with experimental data obtained in the calibration of a reflecting polarizer used at the OVRO were also presented and predictions from our model are in good agreement with it. The only discrepancies appeared in the nature of a resonance, more precisely its width. But we have shown that it could be accounted for by including in the analysis a proper treatment of the effects of the nature of the incident radiation on the response of the polarizer.

We are grateful to J. B. Shapiro and E. E. Bloemhof for their permission to use their previously published experimental results. We wish to thank the staff of the Owens Valley Radio Observatory, especially D. P. Woody and J. W. Lamb for numerous discussions and suggestions. The Owens Valley Radio Observatory is funded by the National Science Fundation under Contract No. AST 96-13717. M. H. work was supported in part by a grants from FCAR and the département de physique de l'Université de Montréal.

Appendix I - Generalization of the principal axes.

Referring to equations (A.46) for the scattering matrix, one first realizes that such a symmetry in its components will always be seen when representing an arbitrary polarizing grid. Only the functions which define R^{uu}, T^{uu}, ... will change. Further, when trying to reduce the scattering matrix to a form similar to equation (A.53) it is only necessary to concentrate on only one of the two blocks (each appearing twice) present in equation (A.46). For example, if one diagonalizes the block composed of the reflection coefficients then the transmission block is also diagonalized and vice-versa. In obtaining the results which follow, we have worked with the reflection block appearing in the upper left and lower right of equation (A.46). We will now show that the orientation of the principal axes is determined by the symmetry of the grid and can be deduced using the formalism of group theory.

As seen by the incident wave, the grid has a symmetry which can be expressed by a representation of the point group C_{2v}. The four ccvering involved are: the identity (E), a rotation by π about the w-axis (C_2), a reflection (σ_v) across a plane defined by the w-axis and and an axis defined by the projection of the direction of the wires in the plane of the incident field and finally another reflection (σ_v') across a plane perpendicular to the previous one (and to the plane of the incident field). Upon studying the character table of this group (see Tinkham (1964, p. 325)) and the effect of the above operations on the two possible states of linear polarization (along the u and v-axes) we find that only two non degenerate irreducible representations (B_1 and B_2 in Tinkham (1964, p. 325)) will be realized. For each of these there will exist one eigenvector, each corresponding to a given principal axis. These can be deduced by constructing the appropriate symmetry coordinates (Wilson et al. 1955) which turn out to be the two principal axes $\mathbf{p}_1$ and $\mathbf{p}_2$ previously defined in section 3.3.1.

Since this result was obtained with the use of group theory, it is perfectly general and independent of any approximations that can be used in dealing with a polarizing grid.

Appendix II - List of symbols.

a wire radius,

$\mathbf{A}_s$ scattering vector potential,

c speed of light in free space,

d wire spacing,

$\mathbf{E}_i, \mathbf{E}_s, \mathbf{E}_T$ incident, scattered and total electric field,

F constant $\left(= \frac{\pi \mu_o \omega a}{2}\right)$,

h grid-mirror separation (reflecting polarizer),

$\mathbf{H}_s$ scattered magnetic field,

$H_n^{(2)}$ Hankel function of the second kind of order n,

$\mathbf{J}$ current density vector,

J_n Bessel function of the first kind of order n,

$\mathbf{k}$ wave vector of the incident wave $\left(|\mathbf{k}| = k = \frac{2\pi}{\lambda}\right)$,

k' $= k\sqrt{1-\alpha^2}$,

$\mathbf{K}$ surface current vector,

$\overline{K^z}, \overline{K^\theta}$ mean longitudinal and azimuthal surface current,

$\mathbf{p}_1, \mathbf{p}_2$ principal axes of a grid,

R^x, R^y, R^z reflection coefficients in the system of coordinates of the grid (see Figure 17),

$R^{u'}, R^{v'}$ reflection coefficients in the system of coordinates of the laboratory (see Figures 17 and 18),

$R_{\|}, R_{\perp}$ reflection coefficients along the principal axes of a grid,

R_{TE}, R_{TM} transverse electric and transverse magnetic reflection coefficients of the mirror,

$\mathbf{S}$ scattering matrix,

T^x, T^y, T^z transmission coefficients in the system of coordinates of the grid (see Figure 17),

T^u, T^v transmission coefficients in the system of coordinates of the laboratory (see Figures 17 and 18),

$T_{\|}, T_{\perp}$ transmission coefficients along the principal axes of a grid,

W_o, z_R beam waist and Rayleigh range of a circular Gaussian beam,

$\mathbf{Z}$ impedance matrix,

$Z_o,$ impedance of free space $\left(= \sqrt{\frac{\mu_o}{\epsilon_o}}\right)$,

Z_p, Z_n grid impedance along the principal axes (as defined with the impedance matrix),

Z_s surface impedance of the wires $\left(= (1+j)\sqrt{\frac{\mu_o \omega}{2\sigma}}\right)$,

$Z_{\|}, Z_{\perp}$ grid impedance along the principal axes (as defined with the scattering matrix),

α projection of the normalized wave vector on the x-axis $(= \sin(\chi_i)\sin(\varphi_g))$,

β projection of the normalized wave vector on the y-axis $(= \sin(\chi_i)\cos(\varphi_g))$,

γ projection of the normalized wave vector on the z-axis $(= \cos(\chi_i))$,

α', β', γ' projection of the normalized incident field on the x, y and z-axes,

α'', β'' projection of the normalized incident field on the u and v-axes,

$\delta(x)$ Dirac's delta distribution,

ϵ_o, μ_o permittivity and permeability of free space,

η, ξ random errors in wire radius and spacing,

λ wavelength,

σ wire conductivity,

φ_g, χ_i angle of grid rotation and angle of incidence,

Ψ Euler's constant ($\simeq 0.577215$),

ω angular frequency of radiation.